IMPEDANCE MATCHING BASED STABILITY CRITERIA FOR AC MICROGRIDS

by

Patricio A. Mendoza-Araya

A dissertation submitted in partial fulfillment of
the requirements for the degree of

Doctor of Philosophy

(Electrical Engineering)

at the

UNIVERSITY OF WISCONSIN–MADISON

2014

Date of final oral examination: 02/12/2014

The dissertation is approved by the following members of the Final Oral Committee:
Giri Venkataramanan, Professor, Electrical and Computer Engineering
Thomas M. Jahns, Professor, Electrical and Computer Engineering
Christopher L. DeMarco, Professor, Electrical and Computer Engineering
Bulent Sarlioglu, Assistant Professor, Electrical and Computer Engineering
Suman Banerjee, Associate Professor, Computer Sciences

To my father, Galvarino, for the encouragement he gave me to pursue this dream.

ACKNOWLEDGMENTS

I would like to thank my advisor, Professor Giri Venkataramanan, for the almost six years we spent doing research together. I am grateful for having had him as my advisor, as he provided me with continuous guidance and experienced views of the problems I encountered during my time in Madison. His dedication towards me and the rest of his students is unique and appreciated.

I would like to thank the rest of my committee for their feedback during my thesis work, and the Wisconsin Electric Machines and Power Electronics Consortium (WEMPEC) for their support during my research. I would also like to thank the Electrical and Computer Engineering department at the University of Wisconsin-Madison for their help during my student and researcher years at the university.

I would like to thank the Fulbright Scholarship Program, Comisión Fulbright Chile, CONICYT-Chile and The University of Chile for their continuous support during my time as a graduate student away from Chile.

I would like to thank my fellow graduate students and friends who joined me these years. While some of them are gone, others are about to leave: Dan, Pedro, Justin, Phil, Micah, James, Shiv, Manuel, Jonathan, Roberto, Di, Adam, Patel, Wei, Wanjun, Junjian and Silong. Special thanks to Malte, Julia and Ray, who helped me with the experiments at the UW Microgrid.

Last but not least, I would like to thank my family. First, I would like to thank my parents, Galvarino and Patricia, without them nothing would be possible. I am grateful to my wonderful siblings, Eliana, Alejandro, Francisca, Rocío and Pablo, who have always been there for me. I am also thankful to the rest of my family who, while being far away, have shown their support in different forms. Bárbara, who joined me in the last stage of my studies, has been an incredible support and partner. She gives a special meaning to this work, as she does with everything in our lives.

CONTENTS

LIST OF FIGURES

LIST OF TABLES

ABSTRACT

Stable operation of the electrical system in the context of microgrid and smart grid technologies is imperative to enable their large scale adoption. Even though many of the analytical tools that are applied to large power systems are readily applicable to microgrids, there are certain key aspects that render some of these tools inadequate and require others to be adapted. This work is aimed at an evaluation of several stability criteria applied to a microgrid environment, which comprises distributed generators, storage devices and loads operating on a droop-control strategy. Stability criteria based on impedance matching at the point of application allow the prediction of instabilities in the grid-tied and islanded cases. Analytical, simulation and experimental results show interesting and intuitive relationships between the parameters of the microgrid components and the stability boundaries. These relationships can be utilized to establish design tools for ensuring robust operation of microgrids.

Professor Giri Venkataramanan

1 INTRODUCTION

The electric grid is facing new challenges everyday. For example, the electricity grid in the US has been subject to several problems due to natural disasters, such as the storms and hurricanes in the last few years, that have ended in power outages ranging from few hours to several days [1, 2, 3]. In these emergency cases and others, the use of energy resources that are close to the consumers is an attractive idea. Nowadays, there are several energy resources already available close to the consumer's location, such as electric or hybrid vehicles and combined heat and power (CHP) units. However, there is a need for those resources to be successfully coordinated and to take advantage of existing and new infrastructure.

The concept of *microgrid* is emerging to be a technically viable approach for meeting reliable supply of electricity with increased availability in the presence of large scale grid disturbances induced by severe weather events, as well to integrate various types of electricity sources and storage devices. The definition of the microgrid concept by the United States Department of Energy's Microgrid Exchange Group is

> "A group of interconnected loads and distributed energy resources within clearly defined electrical boundaries that acts as a single controllable entity with respect to the grid, and can connect and disconnect from the grid to enable it to operate in both grid-connected or island mode. "

Microgrids may find a broad range of applications from autonomous systems on rural communities to smart and energy-efficient buildings. A conceptual diagram of a microgrid is shown in Figure 1.1. In this diagram, distributed resources (DR) inject power to the system, where local loads, third party loads and the grid might be present. A microgrid is expected to have several features: to smoothly transfer from grid-connected to islanded mode and vice-versa; to work with no explicit communication system; to provide localized energy management for the

improvement of power quality and efficiency; to be scalable in terms of loads and sources; and to provide plug and play capabilities.

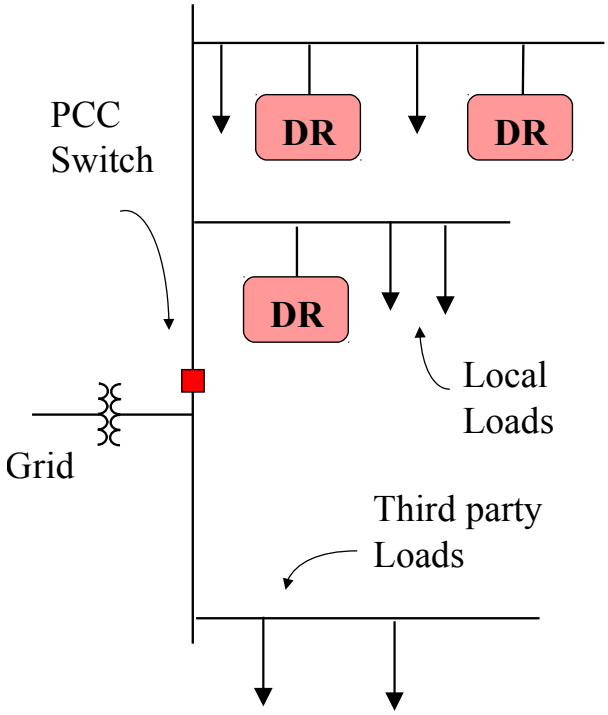

Figure 1.1: A microgrid conceptual diagram

It is in this last feature, the *plug and play* capabilities, where the operational viability of microgrid has seen the least advance, specially when it comes to uncertainties about its stable operation. Ideally, a microgrid should ensure its stable operation under any circumstance, even when the large scale grid or the microgrid dynamically changes due to the incorporation of new units. Every time a new unit is connected to a microgrid, the system increases its complexity. The state-of-the-art approaches to studying and ensuring the stability of microgrids are largely incapable of providing the structural certainty to promote true plug and play operation, particularly with changing network conditions.

Thus, there is a need and an opportunity to develop a stability criterion that can truly promote the plug and play capabilities expected from a microgrid.

1.1 Goal

The main goal of this work is to contribute to the *plug and play* capabilities of a microgrid and its components, through the development of suitable stability criteria. The stability criteria should be applicable to microgrids that may change and grow.

This goal is completed by pursuing the following objectives:

- Propose a modeling approach compatible with the *plug and play* concept.
- Develop suitable models for microgrid components that allow an easy assessment of the stability when interconnected.
- Validate microgrid models by studying representative microgrid configuration cases.

1.2 Approach

The stability criteria proposed in this thesis uses *incremental phasor impedances and admittances* defined at a point of interconnection. The definition of the incremental phasor impedance and admittance as used in evaluating the stability criteria herein depart from the classical definitions of impedance and admittance, as will be developed further in this thesis.

The studies in developing the incremental phasor impedance and admittance are performed in several domains as appropriate in order the validate the proposed approach. The work follows analytical domains with numerical evaluations, time-domain simulations and experimental hardware. The approach of the study in each of these domains is shown in Figure 1.2.

In the analytical domain, the impedances are obtained through the transfer functions. The transfer functions are in turn the result of a state space representation. The state space representation is created using dynamic phasor modeling, which is covered in Chapter 3. Even though dynamic phasors have been used in a power system context, their application to microgrid is not as well developed. Therefore,

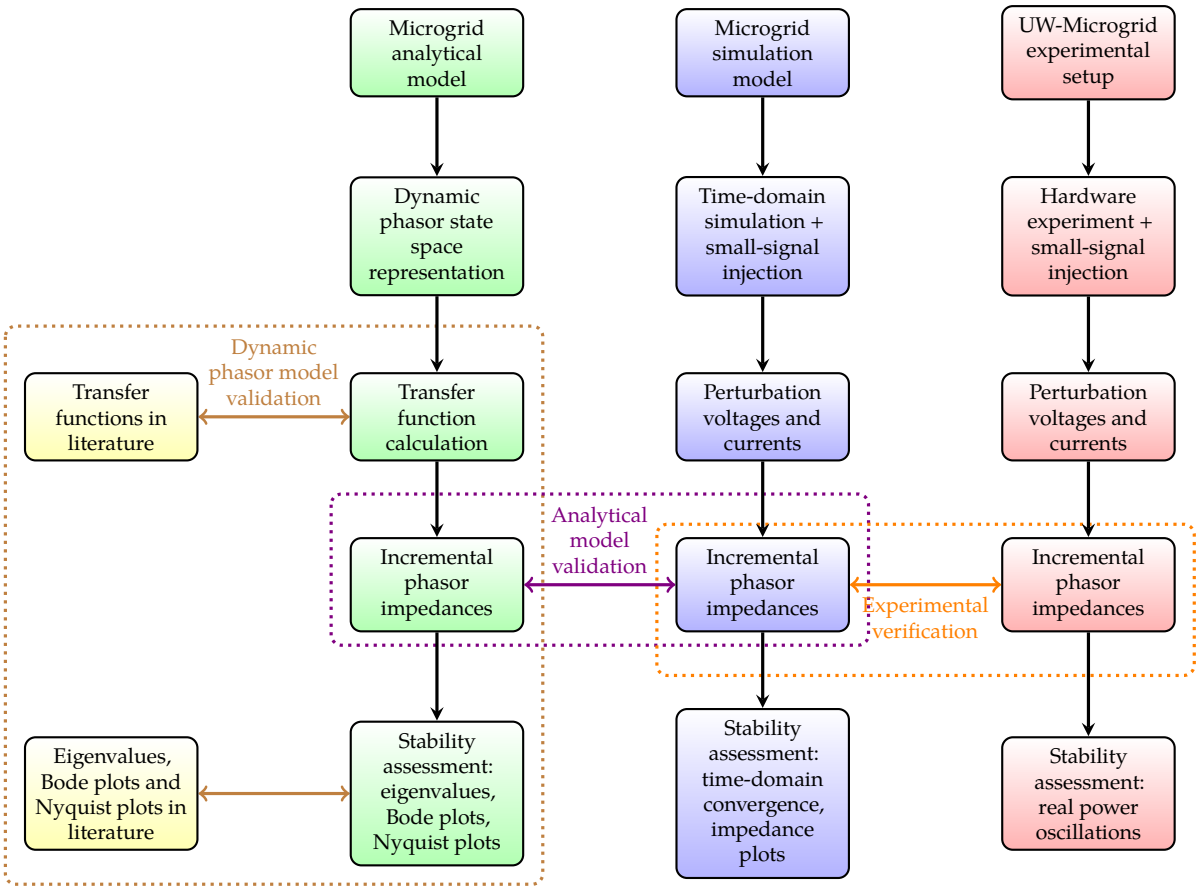

Figure 1.2: Impedance matching stability criteria methodology for different application domains. On the left, the analytical domain uses a transfer function to obtain impedances. On the center and the right, the simulation and real-world domains use perturbation voltages and currents to obtain impedances.

the results from the dynamic phasor models will be validated against other existing models in literature. The procedure to obtain impedances from these models is presented in Section 3.5.

In the simulation domain, the impedances are a result of the perturbation currents and voltages when a small-signal perturbation is injected into the system. Time-domain simulation components are detailed in Section 3.6, and simulation results are shown in Sections 4.1.3, 4.2.2 and 5.4.2.

In the experimental domain, the procedure is similar to the one used in the

simulation domain. Perturbation currents and voltages are also injected into the microgrid, and the impedances are obtained through signal processing techniques to verify the validity of the criteria. The University of Wisconsin Microgrid provides an excellent hardware installation to perform small signal injection and incremental phasor impedance spectroscopy.

1.3 Document organization

This thesis is organized in several chapters as follows. In Chapter 2, a detailed literature review is presented. It includes topics directly and indirectly related to microgrid stability. The analytical development of the incremental phasor dynamic models is detailed in Chapter 3. These models are the foundation of the impedance matching stability criteria introduced in this thesis. Chapters 4 and 5 present the cases of single source and multiple sources microgrids respectively. In both chapters, the analytical models will be presented, and numerical and time-domain simulation results will be obtained. Chapter 6 describes the hardware setup and experimental tasks performer in order to validate the analytical and simulation models. Chapter 7 extended the incremental phasor models two mode complex loads. In Chapter 8, a summary of this document is presented, as well as the conclusions and future work.

2 MICROGRID STABILITY: STATE OF THE ART

In this chapter, a detailed literature review regarding microgrids and its stability problems is presented. Due to the variety of stability problems that are present in an Electric Power System, the first section presents an overview of the traditional views on stability issues in AC Electric Power Systems. Also, this section briefly introduces the stability criteria used in feedback control systems, and presents the key criterion used later in the impedance matching technique: the Nyquist Stability Criterion. The second section presents an overview of the stability issues, studies and approaches in DC systems, which inspired the impedance matching stability criteria developed later in this thesis. The third section presents the current trends in microgrid stability studies, which utilizes many of the tools already presented in the previous sections. As we will show, many of the stability studies in microgrids require a comprehensive model, which changes on any and every single modification of such microgrid. The last section summarizes the state of the art, and how the present work contributes to the successful development of practical plug and play microgrids beyond the state of the art in a new framework.

2.1 Stability in traditional Electric Power Systems

Electric Power Systems (EPS) are a complex mix of generation, transmission and distribution systems, whose operation is not always completely predictable. The ability of a system to remain in equilibrium, during and after a perturbation, and on its steady state, is called stability. Traditionally, Power System stability studies are focused on a particular aspect of such system: (comprehensive information can be found in [4, Ch. 2])

- Angle stability: the ability to maintain synchronism and torque balance.
  - Small signal stability: small disturbances.
  - Transient stability: large disturbances.

- Mid-term and long-term stability: large voltage and frequency excursions.
- Voltage stability: the ability to maintain steady acceptable voltage and reactive power balance.

In particular, we are interested in the *small signal* stability problem. An EPS is *small signal* stable if it is able to remain in the same operating point after a small perturbation. In contrast, an EPS is *transient* stable if, after a larger perturbation, the system ends in an equilibrium point, which could be different from the operating point before the perturbation. For the purpose of a small signal stability study, the system is represented by differential equations in a state-space form, and is linearized around an equilibrium point. Such procedure is presented below in Section 3.2 on page 23 of this document.

The choice of state variables depend on what aspect(s) we are interested in studying. For example, choosing rotor angles as state variables could give immediate information about torque balance and angle stability. However, the stability of the EPS does not depend on the choice of state variables. Nevertheless, it is important to note that the assumptions under which the linearization is done will have an impact on what dynamics are well represented in the model.

The small signal stability of dynamic systems (represented by differential equations) can be studied by Lyapunov's first and second methods. Lyapunov's definition of stability and the development of the stability methods are presented and thoroughly treated in [5, Ch. 5]. By Lyapunov's linearization method, the stability properties of a non-linear system could be studied by linearizing the system around an operating point.

For linear systems that are time-invariant and have no inputs, Lyapunov stability is expressed as conditions over the eigenvalues of the state matrix:

- The system is stable if and only if all eigenvalues have negative or zero real part.
- The system is exponentially stable if and only if all eigenvalues have negative real part.

- The system is unstable if and only if there is at least one eigenvalue with positive real part.

It is possible to utilize another approach to study the stability of a linear autonomous system, by solving the Lyapunov Matrix Equation [5, Sec. 5.4]. It is also possible to study the stability properties of linear time-variant systems by analyzing the state transition matrix Φ of a given linear system. However, those methods escape from the scope of this thesis.

For linear systems with inputs, the concept of bounded-input-bounded-output (BIBO) stability is often used. A system is BIBO stable if its output is bounded for every bounded input [6]. A linear time-invariant system is BIBO stable if and only if every pole of its matrix transfer function has a negative real part. The matrix transfer function is obtained by using the Laplace transform over the state, input, output and feed-forward matrices[7] as shown in (3.12) in page 26. BIBO stability and Lyapunov stability are related properties on linear time-invariant systems [5, Sec. 6.3], as the eigenvalues are used to establish the stability properties. However, BIBO stability and Lyapunov stability are independent concepts which relate stability of the output of a forced system, regardless of the internal state, and the stability of the output of an unforced system with a given initial condition, respectively.

The small signal stability is usually assessed, hence, by an eigenvalue analysis. After the system is linearized, the eigenvalues of the state matrix are obtained. The location of those eigenvalues in the complex plane provide insightful information about the dynamics of the system under small disturbances. For the system to be stable, all eigenvalues must have non-positive real part.

The stability of systems with feedback (Figure 2.1) can be also studied by eigenvalue analysis. However, the characteristics of such systems open the possibility of assessing their stability through the study of the plant, control and feedback components separately. In particular, the loop gain (sometimes called return ratio) plays an important role on the stability of the closed loop feedback system [8, 9].

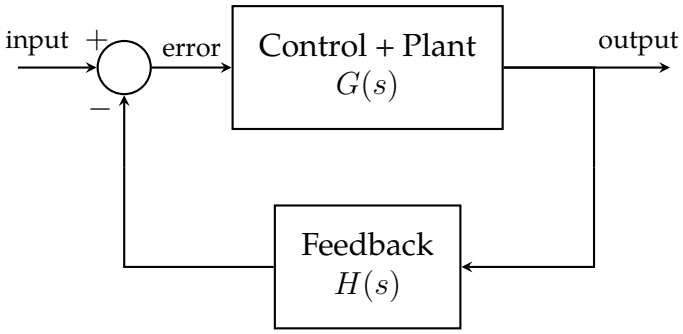

Figure 2.1: Generic system with feedback

The appealing idea of assessing the stability of a system by knowing the properties of the separate components of the feedback system was well developed on the electronics area in the first half of the twentieth century [10, 11]. Developments such as the Bode plot, phase and gain margin criteria, and the Nyquist plot dramatically changed the theoretical understanding of feedback systems.

The Nyquist stability criterion states that, for a negative feedback system such as the one in Figure 2.1 the closed-loop system is stable if and only if the number of unstable poles of the loop gain $H(s) \cdot G(s)$ are equal to the number of counterclockwise encirclements of the critical point $(-1, 0)$ in the Nyquist plot [12].

2.2 Stability in DC systems

Recent interest in DC power systems have demonstrated that they are definitely not a technology of the past. In fact, The IEEE Power and Energy Magazine dedicated its November/December 2012 issue to this type of power systems. Two articles [13, 14] discuss DC distributed power systems in data-center and microgrid environments. Although conclusions of both articles are positive and promising, some barriers for DC power systems are identified.

From the stability point of view, abundant research has been done on DC power systems in the last forty years. Several stability criteria have been developed [15], such as the Middlebrook stability criterion, Phase and Gain margin criterion, among

others. In general, these criteria are applied to two sections of a DC system about to be connected, specifically over the ratio of output and input impedances of such sections.

The research on DC power systems have been developed for studying power systems present on ships [16, 17, 18]. On those systems, the effect of the source impedance in the stability of the system was recognized when regulated converters [16] and constant power loads [17] are present; boundaries on the value of such impedance are developed. Reference [18] presents a solution by means of control algorithm, in which a field oriented control strategy is used to stabilize the DC link of an electric propulsion system.

Recent research has been done in stability analysis that specifically uses impedances and admittances. Power electronics based power distribution systems (PEDSs) are described in [19], and the stability approach in this particular case is less conservative than others such as the Opposing Argument criterion or the Gain margin and Phase margin criterion [15]. Furthermore, it is recognized that the impedances and admittances are a function of the operating point (e.g. output power), hence the impedances and admittances are considered as a set of values rather than a single value. In this way, the stability-constrained region, which is usually a region of the complex plane, is translated into a forbidden volume in a 3-D space. The immitance-based stability criteria is further developed in [20], where the new forbidden region is described by a continuous function, instead of the piecewise linear function used in [19].

Reference [21] introduces the concept of DC Distribution Power Systems (DPS), and the stability assessment of the Power Electronic Building Blocks (PEBBs). The stability concern appears at the control loop, filter subsystem interaction and system-level interactions. In all cases, loop gains and impedance ratios appear as key quantities for stability assessment. Design challenges and opportunities for this kind of systems are presented in [22], in the context of computer, telecommunication and network systems. The focus of this work is on EMI and and high frequency converters.

Related research, which applies similar criteria on other AC, DC and hybrid

systems, is presented in Section 2.4.

2.3 Stability in microgrids

The stability of microgrids has been a topic of great interest: even though a microgrid resembles a small-scale EPS, its control and operation differs from this larger counterpart in many aspects, such as the centralized control and operation paradigm, the impedance characteristics of the transmission lines (reactive in large-scale systems vs. resistive in small-scale systems), the relative power rating of sources and loads, and the large penetration of inverter-based sources, among others. Comprehensive reviews on microgrid control and related literature are found in [23, 24, 25, 26].

In order for an AC grid to operate properly, several controls need to be present. For example, frequency and voltage regulation is necessary to achieve power transmission over the network [27, Sec. 1.3]. In the microgrid environment, a distinction is made between units that participate in those regulation tasks and those that do not. A *grid-forming* unit is a microgrid unit that participates in the frequency and/or voltage regulation, while a *grid-following* unit is a microgrid unit that does not participate in any kind of regulation. This distinction is of major importance because the behavior of a microgrid is drastically different whether it is parallel to a larger (e.g. national) grid or islanded, and the grid-forming and grid-following units interact with the microgrid in a completely different way under those two operating modes. The control strategy of a grid-following unit could be similar to any of the grid-tied units already present in a EPS. The control strategy of a grid-forming unit, however, deserves a deeper analysis, and is one of the most active topics of microgrid research, specially in the case of islanded operation.

One of the first environments that recognized the necessity of a novel control approach for islanded systems was the Uninterruptible Power Supply (UPS) applications [28]. In such setting, the parallel operation of multiple UPS systems posed a challenge in terms of decentralized control strategy. Droop controllers for frequency and voltage are introduced, which allow the system to share power

and operate with measurements that are local to each individual UPS. A stability analysis on line interactive UPS systems is presented in [29], where it is recognized that large frequency droop gains affect stability, while voltage droop gains usually do not.

Even though [28] set a milestone in microgrid control through the proposal and detailed study of the droop control, it was not until the 2000's when the microgrid concept was formally introduced [30]. A detailed study and evaluation of the microgrid concepts, along with discussion and experimental results are presented in [31]. Details of the UW-Microgrid laboratory setup are also included in this article. Moreover, the first discussions of stability issues on a microgrid environment are presented in [32] and [33], where the authors develop time domain simulations, apply small signal models for the microgrid components and use eigenvalue analysis. In all these studies, the droop control has been a widely adopted approach [34] and it also among the subjects of study in this thesis.

2.3.1 Small signal stability in microgrids

The small signal stability of a microgrid has been thoroughly studied in the last two decades. Typically, the study involves a simplified microgrid, with a single inverter-based source coupled to an infinite bus or stiff grid. For example, Reference [35] uses a small signal model of a three-phase distributed generator using dynamic phasors. Using eigenvalue analysis, the large signal and small signal models are compared, and a deadbeat droop control is proposed. The dynamic phasor model is found to be better suited for this kind of analysis and design. Reference [36] also uses dynamic phasors to model a single source connected to an infinite bus; it is recognized that the stability of the frequency droop control depends on the X/R ratio of the interconnection, and virtual impedance is used to ensure stability (see Section 2.3.2).

Throughout the years, researchers have developed more systematic ways of establishing the stability of a less constrained microgrid, with generalized small signal models for an islanded or grid-tied microgrid. Reference [37] presents a

stability analysis framework using small perturbations on a d-q reference frame. The framework is exemplified on a two-source standalone microgrid, and eigenvalue analysis and simulation results are provided. By using the resulting root loci, a designer could pick optimal droop parameters and filter cut-off frequencies.

Reference [38] presents a novel modeling approach for the microgrid, in which the electric network, loads and inverters have their own state-space model. These models are brought to a common d-q reference frame and interconnected together, resulting in a large state-space representation of the whole microgrid. Once this full model is obtained, eigenvalue and sensitivity analyses are performed, and exemplified on a three-source grid-tied microgrid. It is recognized that the low-frequency modes (eigenvalues) are those who determine the stability of the system, and are dependent on the network configuration and droop controllers, while the high-frequency modes are sensitive to inverter inner loops, load and network dynamics. Similar conclusions are drawn in [39], with an equivalent modeling approach.

Reference [40] introduces a generalized computational method for small signal stability assessment of a multi-inverter microgrid. The approach is very similar to the one in [38], with the exception that the plant model is simplified in order to reduce the complexity of the resulting system. The computational method is exemplified with a three-source ring-topology microgrid.

The article in Reference [41] is particularly focused on *chain* microgrids, i.e. microgrids whose individual distributed sources are longitudinally chained by inductive transmission lines. The author finds sufficient conditions for the stability of such chain microgrid. The small signal models are further developed in the author's thesis [32], including the *parallel* microgrids, i.e. microgrids whose individual distributed sources are connected in a star topology through inductive transmission lines. Both *chain* and *parallel* configurations are contrasted in terms of the conditions that droop gains need to comply with in order to ensure microgrid stability.

2.3.2 Alternatives and improvements to droop control

The droop control is not the only approach for microgrid control. Reference [42] presents a microgrid control that requires communication among all inverters to operate properly and maintain power quality. The control scheme is subject to performance testing with linear and non-linear, balanced and unbalanced loads, with successful results.

As an alternative to the frequency droop controller, an angle droop controller is proposed in [43]. The operation and control of both the frequency and angle droop controllers are compared over a hybrid microgrid, i.e. a microgrid that contains inertial and non-inertial sources. The angle droop successfully provides power sharing among the units and the system frequency deviation is smaller that with the traditional frequency droop control. Reference [44] shows how the angle droop control needs high droop gain to ensure proper power sharing. Due to the stability issues that this high droop gain generates, the authors propose an additional stabilizing loop, inspired on the Power System Stabilizer (PSS) used in traditional EPS. The stability study in this paper is done by eigenvalue analysis.

Reference [45] improves on the angle droop control by adding a Distributed Static Compensator (DSTATCOM) to the microgrid, enabling the ride-through capability. The results are supported onto extensive simulations over a radial three-source microgrid with inertial and non-inertial sources.

As the researchers recognized how the impedance of transmission lines and other units constrained the magnitude of droop gain that allow stable operation, several methods to modify the apparent impedance of converters were proposed. The concept of virtual impedance is presented in [46, 47], which modifies the output impedance of the converter by means of control strategy at the voltage regulation loop. The case of resistive output impedance shown in [46, 47] has a positive impact on the stability of the system.

Interesting developments in stability of single-phase microgrids are presented in [48, 49]. In Reference [48], the authors introduce the concept of microgrid *gateway*, a device that allow the interconnection of AC microgrids of different frequencies. The

authors already recognize the impact of the inverter controller in the behavior of the system, and develop further in [49]: several inverter controllers are specifically modeled for stability study using dynamic phasors, and regions of stability are found as a function of the impedance ratio and interconnection reactance. A detailed analysis of these topics are also included in the author's thesis [50].

One of the most recent developments is presented in [51], where the stability of a microgrid is studied as part of the effort to improve the power control bandwidth of a grid-forming source. After establishing a simple criteria for stability, based on a relationship between series resistance and droop gain, two control improvement methods are proposed: active damping and loop shaping. From these two, active damping shows better dynamic characteristics, and is developed further in [52]. These topics are thoroughly detailed in the author's thesis [53].

2.3.3 Other topics related to microgrid stability

The usual droop controllers, which relate frequency with active power and voltage with reactive power, are only suitable for systems with interconnections lines that are strongly reactive. On distribution systems, this is not always true, and microgrid systems with strongly resistive lines tend to perform poorly with the traditional droop controllers. In [54], the authors propose a linear rotational transformation of the active and reactive power, such that the transformed quantities are effectively controlled by the usual droop controllers. The improvements are demonstrated along with a controller that includes virtual impedance and controls current instead of power.

As stated above, the selection of droop gains in a microgrid has an impact on the stability. However, the technical constraints are not the only ones to be considered when selecting the gains. As the droop gains modify the operating points of the units in the microgrid, they certainly have an impact on the technical and economical operation of a microgrid, and several researchers have developed tools to incorporate economical constraints to the droop gain selection process. Even though the selection could be done offline, the inclusion of an Energy Manage-

ment System (EMS) is usually assumed. In [55], the authors propose an EMS that minimizes fuel consumption while ensuring stable operation. In [56], the authors study how the selection of droop gains impacts the reserve requirements using bifurcation theory to ensure stability. Note that both papers impose stability as one of the constraints of an optimization algorithm.

Other topics that escape from the small signal stability problems are also of remarkable research interest. For example, a study of transient stability on a microgrid is presented in [57] where the microgrid is exposed to faults under islanded and grid-tied operation. Primary frequency regulation is approached in [58], in a system that incorporates wind power, micro hydropower, energy storage and dump load. A probabilistic analysis of the small signal stability is presented in [59] using Monte Carlo simulation. These topics, however, are out of the scope of this thesis.

2.4 Impedance analysis

The Middlebrook criterion [60] was originally applied to input filters in power switching converters, where the author was interested in establishing the conditions under which the filter does not have deteriorating effects on the dynamics of the converter to be connected. However, it was recognized that this stability criterion could be applied to the interconnection between any two DC subsystems [15].

There are many recent developments in the stability study of DC systems, as it was shown in Section 2.2. However, only the most mature tools used in DC systems have been recently extended to AC systems. The technique used in AC systems is to obtain a small signal model of the system under a certain operating point, and use this model (which may look like a DC system in the synchronously rotating d-q reference frame) to study the stability characteristics. These models have an structure similar to the ones obtained by the state-space averaging method used in power converters studies [61]. As a result, the system is represented in a state-space form, with matrix transfer functions that relates different small signal variables, or *channels*. When the small-signal impedances or admittances are of interest, the

systems are modeled using currents and voltages as inputs and/or outputs, such that the transfer functions relate the right variables. One example of this technique is shown in [62], where models for AC-DC, DC-AC and DC-DC converters are provided and experimentally verified.

As an approach to AC system stability studies through impedances, References [63] and [64] show the Nyquist stability criterion applied to multi-pulse rectifiers and active front-end rectifiers respectively. In both cases, the systems are modeled in d-q reference frame, and the stability is assessed by the study of the return ratio matrix. It is demonstrated that only the d-d channel information is necessary to establish the stability of the rectifiers. The idea of using models in d-q was already presented in [65], where AC power systems with regulated loads are studied.

The use of the impedance as an instrument to study stability was experimentally verified in [66]. In this particular case, two DC-AC converters were interfaced on the AC side, and the stability was assessed on the AC link, on the d-q reference frame.

2.4.1 Impedance measurement

The impedance measurement in AC systems has been explored from several points of view. Reference [67] gives an overview of system identification techniques used for the measurement of grid impedance. The authors propose an online impulse-response-based technique to identify the grid impedance on a grid-tied inverter in sequence components. Another method based on impulse response is presented in [68], where the focus is on the nonstationaryness of the power system; a method that requires observation times in the order of one second is presented.

Several AC impedance measurement methods are introduced in [69, 70]; a three-phase bridge, three-phase chopper and a wound rotor induction machine are used to obtain impedances in d-q components. A similar approach is used in [71], in which a single-phase system is studied using d-q components that are obtained by the use of the Hilbert transform on the single-phase quantities. The authors further develop impedance measurement on an AC system by a line-to-line injection [72],

recognizing that one of the currents in the d-q reference frame can be set to zero.

The impedance measurement on the d-q reference frame is introduced in [73], where a simple AC system consisting of a three-phase source and passive linear loads is studied. The measurement system uses a Phase-locked loop (PLL) to synchronize the rotating d-q reference frame and allows multiple injections at the different channels.

A different method is presented in [74], where the injection is a white noise and a system identification approach is used. The proposed method is used in a low power system and several passive loads are inserted into the system and their impedances are obtained.

2.5 Literature review summary

Even though the microgrid has been subject of ample research, several existing tools are unattractive when applied to a microgrid with plug and play capabilities. Tools such as [40] are appealing for the design and planning process of a new microgrid. However, they are unsuitable for a large, growing microgrid, in which new units are added to the system and would require a complete remodeling of the system every time the microgrid changes.

On the other hand, impedance analysis tools such as [63] are appealing for existing systems that face the addition of a new unit. For these dynamically changing systems, the stability assessment at the point of connection of the new unit is ideal. However, these tools have only been applied to converters connected to the grid, and no microgrid control has ever been modeled in an impedance representation.

The impedance approach is appealing not only in the design and planning stage of a microgrid, but most remarkably in the everyday operation of it. The vision of an ideal microsource that senses the system right before connecting, and adjusts itself for better performance and stability, could become reality with an impedance matching criterion: the unit could measure the impedance of the existing microgrid, and adjust its internal control parameters for a better match.

Even some fixed parameters such as filter inductances are now possible to adjust by developments such as the virtual impedance or active damping.

From the modeling point of view, the usual approach for modeling AC system dynamics is to use d-q components. In most established applications of d-q component models, the reference frame transformation to convert the real three phase system variables to the abstract system is frequency dependent. However, droop controls that incorporate frequency variation in system operation would render the reference frame transformation to be dynamic, and it is not clear that this formulation would be suitable for the purpose. In this context the dynamic phasor approach, in polar coordinates is appealing because the phase magnitude variable is not affected by the operating frequency. For example, Reference [75] presents a converter that does point-of-load regulation of the voltage *magnitude*, where a model using phasors would allow immediate access to a variable that represents this quantity of interest. In addition, the dynamic phasor representation shown in [75] is fully compatible with other state space representations, such as the the ones resulting from the averaging method of power converters [61], and several other control systems. In particular, it is not difficult to model the microgrid droop control in a state space representation, as shown in Section 3.4.

3 PHASOR DYNAMIC MODELING OF A MICROGRID

As stated in the introduction of this document, the main goal of the present work is to study the stability of a microgrid that facilitates a *plug and play* application approach. The traditional stability assessment is done through eigenvalue analysis, which requires a detailed model of the system under study. The proposed approach utilizes an impedance matching criterion, which is established at a point of interconnection in the microgrid. By using this method, the stability of the interconnection may be studied at such a point, and the properties of the system under study are also established at that point, and in principle avoiding the need to develop a full system model with several unknown structures and parameters.

In this chapter, the stability analysis approach, which uses phasor modeling, will be presented. Both the analytical and simulation models will be introduced. First, the impedance matching approach will be introduced, and the pertinence of its application to the microgrid will be discussed. Then, the classical small signal stability models will be explained. Dynamic phasors models, and their incremental dynamics at an operating point used for impedance matching, will be detailed. Finally, the analytical models for several components of the microgrid will be presented. In addition, the simulation model and parameters are introduced at the end of the chapter.

3.1 Stability of a microgrid: impedance approach

Even though a large part of a microgrid could be considered linear (i.e. it comprises components whose representation models are linear), the introduction of other components (e.g. machines, power electronics) render the system nonlinear in general. Therefore, the stability study of a microgrid requires the modeling of nonlinear components. The resulting nonlinear system can be linearized around

an operating point and the stability of the operating point can be assessed at such point through linear systems tools.

There exist several ways of assessing the stability properties of a power system [4]. However, virtually all the criteria require a complete, detailed model of the whole system. Once the stability of a given system is established, any single modification will potentially have an impact on the stability. Therefore, remodeling of the system is required after any modification if stability assessment is needed. This is specially true when adding extra units to the system, thus, increasing the system's complexity, usually seen as an increase in the order of the system.

A different approach, compatible with the *plug and play* concept, is the assessment of the stability at an interconnection point in the microgrid. Let the microgrid have links with other systems, such as other microgrids, a larger (e.g. national) grid, or an extra unit that is being incorporated into the existing microgrid (Figure 3.1). The microgrid could be conceptually split in two sections, using one of these links as the partitioning point (for example, the new source link shown in Figure 3.1). This point will be called Point of Connection (PoC). The PoC is the only point at which the two areas exchange power.

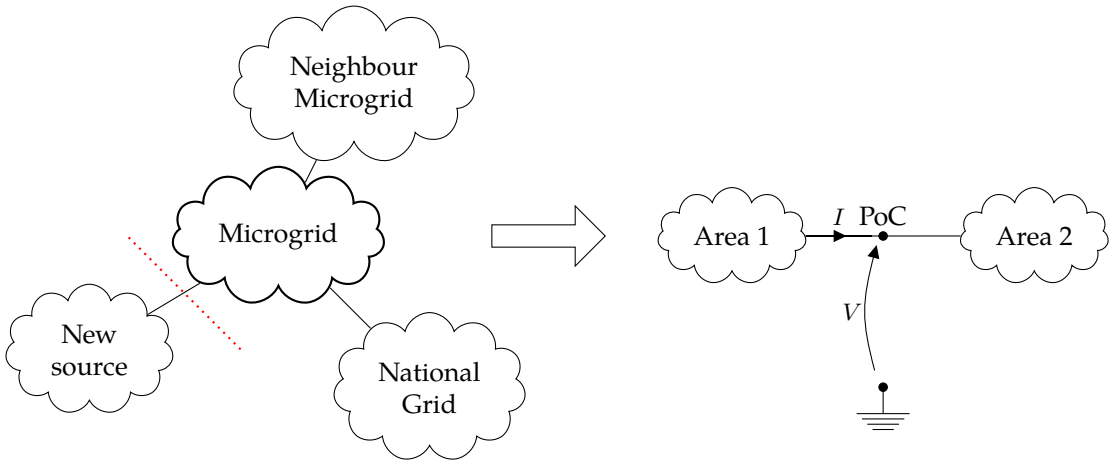

Figure 3.1: Conceptual Microgrid split in two halves

We are interested in establishing the stability of the system at the PoC. If the system is perturbed around its operating point (V, I), the perturbation currents

will flow between Areas 1 and 2, and a perturbation voltage will appear at the PoC. The magnitudes of those perturbations could be represented by incremental impedances at the PoC for both areas. For modeling convenience, we will use an admittance Y_1 for the Area 1 and an impedance Z_2 for the area 2, as shown in Figure 3.2.

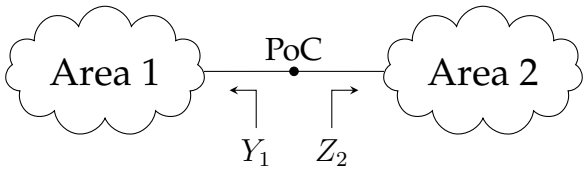

Figure 3.2: Impedances in a conceptual Microgrid

The interactions between the areas may be viewed in the form of a block diagram illustrated in Figure 3.3. It may be observed that Area 1 receives the PoC voltage and draws an output current determined by its admittance. Likewise, Area 2 receives the output current from Area 1 as its input and develops the PoC voltage as its output, as determined by its impedance. The mutual interactions form a close loop system (Figure 3.3(a)): the output of one area is the input to the other area. The closed loop stability properties can be assessed by studying the open loop system properties (Figure 3.3(b)), in particular, by the return-ratio or loop-gain $-Y_1Z_2$. Note how the sign of one impedance changes, as needed by the references shown in Figure 3.2.

In this document, the *impedance matching stability criteria* refers to the use of the Nyquist stability criterion over the loop-gain $-Y_1Z_2$ obtained at a given PoC on a microgrid. Bode plots will be also presented for reference to interpret the frequency response function in more common graphical formats.

Since the interconnected system is in general nonlinear, and is excited at the nominal power frequency, incremental impedances are defined using the dynamic phasor models at the appropriate operating point. This way, the magnitudes and phase angles of the perturbations will be represented in the small signal models.

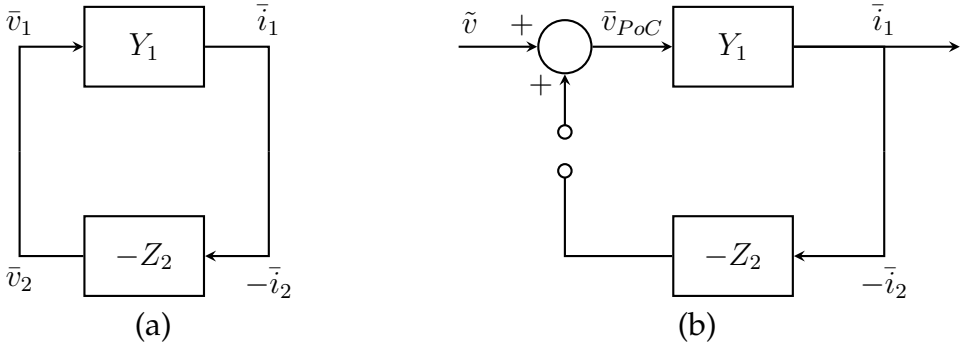

Figure 3.3: Impedance-admittance block diagram of the conceptual microgrid. The stability of the close-loop system (a) can be assessed by the study of the open-loop system (b)

The *incremental phasor impedances* will be obtained from the dynamic phasor models, and used for Y_1 and Z_2 when establishing the stability properties of a microgrid.

3.2 Small-signal stability models

The goal of a small signal model is to construct a linear time invariant (LTI) model of a system around an operating point in order to assess the stability at such point. If the LTI system is stable, then the original system is also stable; if the LTI system is unstable, the stability of the original system cannot be ensured [76].

Every system model can be described in a state space representation, shown in (3.1). For a system with m inputs, n outputs and p states, $x(t)$ is the state vector of dimension p, $u(t)$ is the input vector of dimension m, $y(t)$ is the output vector of dimension n. The function f describes the dynamics of the system, and the function g describes the output of the system. Both f and g are continuous and differentiable.

$$\begin{aligned} \dot{x}(t) &= f(x(t), u(t), t) \\ y(t) &= g(x(t), u(t), t) \end{aligned} \tag{3.1}$$

In the case of an LTI system, both f and g are linear and do not depend on the time t. The general expression for an LTI system is given in (3.2), where A, B, C,

and D are the state, input, output and feedforward matrices respectively.

$$\begin{aligned} \dot{x} &= Ax + Bu \\ y &= Cx + Du \end{aligned} \tag{3.2}$$

To obtain a linearized system, from the general form (3.1) to the form (3.2), the usual procedure is to linearize both f and g around an equilibrium point. The equilibrium points are those who satisfy

$$\dot{x}(t) = f(x(t_o), u(t_o), t) = 0 \; \forall t \geq t_o \tag{3.3}$$

where $x(t_o)$ and $u(t_o)$ denotes the state and input at which the equilibrium is obtained. Once this point has been established, the system can be linearized around it.

For time-invariant systems, described by

$$\begin{aligned} \dot{x}(t) &= f(x(t), u(t)) \\ y(t) &= g(x(t), u(t)) \end{aligned} \tag{3.4}$$

i.e., f and g are not explicit functions of time, the linearization is done around an operating point x_o obtained at input u_o:

$$f(x(t), u(t)) = f(x_o, u_o) + J_{f,x}|_{x=x_o}(x - x_o) + J_{f,u}|_{u=u_o}(u - u_o) + f_1(x(t), u(t)) \tag{3.5}$$

where $J_{f,x}$ and $J_{f,x}$ are the Jacobians of f with respect to the state and input variables respectively, and f_1 is a remainder that absorbs all the differences that the first order approximation cannot represent. A similar process can be applied to g that yields a linear approximation of it.

If we define $\tilde{x}(t) = x(t) - x_o$ and $\tilde{u}(t) = u(t) - u_o$, and neglect the remainders f_1 and g_1, the system (3.4) could be rewritten in terms of $\tilde{x}$ as follows (t is dropped to

simplify notation):

$$\begin{aligned}
\dot{\tilde{x}} &= \dot{x} - \underbrace{\dot{x_o}}_{=0} = f(x,u) \\
&\approx \underbrace{f(x_o,u_o)}_{=0} + J_{f,x}|_{x=x_o}(x-x_o) + J_{f,u}|_{u=u_o}(u-u_o) \\
\tilde{y} &= y - y_o = g(x,u) - g(x_o,u_o) \\
&\approx J_{g,x}|_{x=x_o}(x-x_o) + J_{g,u}|_{u=u_o}(u-u_o)
\end{aligned} \tag{3.6}$$

in which $J_{f,x} \triangleq A$, $J_{f,u} \triangleq B$, $J_{g,x} \triangleq C$ and $J_{g,u} \triangleq D$ are constant matrices when the system is time-invariant.

$$\begin{aligned}
\dot{\tilde{x}} &\approx A\tilde{x} + B\tilde{u} \\
\tilde{y} &\approx C\tilde{x} + D\tilde{u}
\end{aligned} \tag{3.7}$$

If the system has m inputs, n outputs and p states, the components of each of the matrices in (3.7) can be found as:

$$a_{i,j} = \left.\frac{\partial f_i}{\partial x_j}\right|_{x=x_o} \qquad \forall i,j = 1\ldots p \qquad A = [a_{i,j}] \tag{3.8}$$

$$b_{i,k} = \left.\frac{\partial f_i}{\partial u_k}\right|_{x=x_o} \qquad \forall i = 1\ldots p, k = 1\ldots m \qquad B = [b_{i,k}] \tag{3.9}$$

$$c_{l,j} = \left.\frac{\partial g_l}{\partial x_j}\right|_{x=x_o} \qquad \forall l = l\ldots n, j = 1\ldots p \qquad C = [c_{l,j}] \tag{3.10}$$

$$d_{l,k} = \left.\frac{\partial g_l}{\partial u_k}\right|_{x=x_o} \qquad \forall l = l\ldots n, k = 1\ldots m \qquad D = [d_{l,k}] \tag{3.11}$$

Once the linearized, approximated model and its matrices have been determined, the stability could be studied by the eigenvalue analysis of the matrix A or by any of the stability assessment methods described in the previous chapter, as long as the system is time-invariant (which will be the case of the resulting models of this thesis). Some of the stability criteria require an expression for the transfer function

of the system. For the LTI system, the matrix transfer function is determined by

$$H(s) = C \cdot (sI - A)^{-1} \cdot B + D \tag{3.12}$$

where s is the Laplace domain variable and I is the $p \times p$ identity matrix.

3.3 Dynamic phasors

The development of dynamic phasor modeling was inspired by the generalized averaging method of power conversion circuits [77], which is in turn based on the state-space averaging method [61]. The concept presented in [77] aims to generalize over the "small ripple" constraint present on state-space averaging models to allow its application to a broader class of power converters.

The concept of dynamic phasor is based on the generalization of the steady-state phasor quantity, which is complex-valued, to the quasi-steady state, making the magnitude and phase angle of a phasor functions of time. In the general case, the solution of a model's differential equations can be expressed as a Fourier series, in which each Fourier coefficient is referred to as k-*phasor*, where k is the index of such Fourier coefficient. Note that the approximation by a Fourier series is applied on a time interval $(t - \tau, t]$, where τ is a period of interest (e.g. power converter switching period); this interval moves along with the time, as well as the k-phasors. An example of the application of this dynamic phasor technique to a Thyristor Controller Series Capacitor is presented in [78]. This concept has also been applied to more complex power systems, not only consisting of a power converter but also larger systems [79].

The dynamic phasor modeling technique presented in this thesis is closer to the "harmonic linearization" method presented in [80] (also covered as "method of averaging" in [76, Sec. 3.5]), in the sense that it corresponds to the 1-phasor approximation of the non-linear system. Moreover, the method presented here is strongly influenced by previous developments shown in [75].

The traditional steady-state phasor is a complex number that represents an

amplitude and phase angle of a sinusoidal signal in the time domain. They can be expressed in Cartesian coordinates or polar coordinates. Typically phasors are denoted by a bar on top of its variable name. For example the phasor

$$\bar{V}_1 = 1 + j1 = \sqrt{2}\angle 45^\circ \tag{3.13}$$

represents a sinusoidal waveform

$$V_1(t) = \sqrt{2}\cos(\omega_o t + 45^\circ) = \Re\left[\bar{V}_1 e^{j\omega_o t}\right] \tag{3.14}$$

with constant magnitude and phase angle, and implicit frequency ω_o, which is also assumed to be constant.

A dynamic phasor is a generalization of the phasor concept, in which the time-domain signal is represented by

$$V_1(t) = V_1^a \cos(\omega_o t + V_1^\theta) \tag{3.15}$$

where V_1^a and V_1^θ are both functions of time. The superscripts $()^a$ and $()^\theta$ denote magnitude and phase angle respectively. The corresponding dynamic phasor in the complex notation would be

$$\bar{V}_1 = V_1^a \angle V_1^\theta \tag{3.16}$$

Note, however, that frequency variations are able to be represented, because the frequency variability is absorbed in the phase angle function V_1^θ. At sinusoidal steady state, both the magnitude V_1^a and the phase angle V_1^θ are constants.

Uniqueness of the dynamic phasor representation

The representation of an arbitrary waveform $V_1(t)$ by a dynamic phasor $V_1^a \angle V_1^\theta$ is, in principle, not unique. For example, the sinusoidal waveform

$$a(t) = A\sin(\omega_o t)$$

could be perfectly represented by these two dynamic phasors:

$$\begin{aligned} a_1^a &= A & a_1^\theta &= -\pi/2 \\ a_2^a &= A\sin(\omega_o t) & a_2^\theta &= -\omega_o t \end{aligned}$$

The first phasor $\bar{a}_1$ has a constant magnitude and phase angle, while the second phasor $\bar{a}_2$ has a sinusoidally-varying magnitude and a linearly decreasing phase angle.

In order for the dynamic phasor representation to be unique, both the magnitude and phase angle components need to be functions of time that are limited in bandwidth. This is due to the assumption that the waveforms that the dynamic phasors are representing have Fourier transforms whose spectra lie in the intervals $(-2\omega_o, 0)$ and $(0, 2\omega_o)$. The assumption is the same as the one presented in [81], although the dynamic phasor representation of such article is in rectangular coordinates rather than polar coordinates.

In this thesis, it will be assumed that the dynamic phasor magnitude components $()^a$ are bandwidth limited to the frequency range $(-\omega_o, \omega_o)$, where ω_o is the system's steady state line frequency; and the phase angle components $()^\theta$ are bandwidth limited to a frequency range such that the modulation could be considered as narrow-band *phase angle* modulation. This will ensure that the time domain waveforms

$$x(t) = \Re\left[X^a e^{j\omega_o t + X^\theta}\right] \tag{3.17}$$

represented by X^a and X^θ are bandwidth limited to the frequency range $(-\omega_o, \omega_o)$

The variation of the components X^a and X^θ could be seen as *amplitude* and *phase angle* modulation of a carrier waveform of frequency ω_o. As such, the bandwidth of the resulting modulated signal is a function of the bandwidth of the modulating components, and the carrier frequency ω_o.

On the one hand, an amplitude modulated signal has a bandwidth equal to twice the bandwidth of the modulating signal, centered around the carrier frequency [82]. On the other hand, a phase modulated signal (as any other angle modulated signal) has an infinite number of sidebands; however, most of the information (or power)

content of the modulated signal lies in a limited band, whose width is a function of the modulating function and the *modulation index*, introduced by Van Der Pol [83]. The modulation index differs from the modulation index defined for amplitude modulation, in the sense that for amplitude modulation, the modulation index m_a has an impact on how much of the amplitude is modulated, and clipping and distortion may occur, but has not a direct impact on its bandwidth; the modulation index defined for angle modulation has indeed a direct and important impact on the bandwidth of the modulated signal, and requires careful study.

In frequency or phase modulation, the generated sidebands on the frequency spectrum are infinite, and given by a series of Bessel functions of the first type [84, 85, 86]. The spectrum is usually categorized into two types: narrow-band modulation and wide-band modulation. Narrow-band frequency (or phase) modulation is obtained by modulation indexes of less than 20% (or 60°for phase modulation), and the generated spectrum is similar in bandwidth to the one obtained by amplitude modulation. Wide-band frequency (or phase) modulation is obtained by modulation indexes greater that those stated above, and the generated spectrum is contained within a bandwidth equal to twice the modulating depth, which could be wider that the bandwidth of the modulating signal.

Carson's rule (or Carson's law) [87] states that the bandwidth of a frequency (or phase) modulated signal is approximately equal to

$$2\omega_B = 2(\Delta\omega + \omega_m) \tag{3.18}$$

where $\Delta\omega$ is the peak frequency deviation (controlled by the modulation index) and ω_m is the highest frequency of the modulating signal. If the modulation index is very small, the bandwidth is then very close to the one obtained in the amplitude modulation case, which is a case of narrow-band frequency (or phase) modulation.

For the purposes of the dynamic phasor modeling, the modulation indexes are obtained as follows. For frequency modulation,

$$\omega = \omega_o \left[1 + k_f \cos(\mu t)\right] \tag{3.19}$$

is the instantaneous frequency, and the resulting modulated signal is

$$i = A_o \cos\left[\omega_o t + m_f \sin(\mu t)\right] \tag{3.20}$$

where $m_f = \frac{k_f \omega_o}{\mu}$ is the modulation index. Equivalently for phase modulation,

$$\phi = \phi_o \left[1 + k_p \sin(\mu t)\right] \tag{3.21}$$

is the instantaneous phase, and the resulting modulated signal is

$$i = A_o \cos\left[\omega_o t + m_p \sin(\mu t)\right] \tag{3.22}$$

where $m_p = k_p \phi_o$ is the modulation index.

A dynamic phasor $V_1^a \angle V_1^\theta$ is representing

$$V_1(t) = V_1^a \cos(\omega_o t + V_1^\theta) \tag{3.23}$$

For the purposes of studying the modulation, this equation will be matched with (3.22) and (3.20). This is $V_1^\theta = m_p \sin(\mu t) = m_f \sin(\mu t)$. The instantaneous frequency in this case is

$$\frac{dV_1^\theta}{dt} = m_p \mu \cos(\mu t) = k_p \phi_o \mu \cos(\mu t) \tag{3.24}$$

or

$$\frac{dV_1^\theta}{dt} = m_f \mu \cos(\mu t) = k_f \omega_o \cos(\mu t) \tag{3.25}$$

It is easier to see in this last expression that the peak frequency deviation is $\Delta\omega = \omega_o k_f$ or $\Delta\omega = \phi_o k_p \mu$. Since the narrow-band behavior is desired, we must ensure that the equivalent modulation index is less than $60°$or 1 rad [84], or 20% in the case of frequency modulation ($\lambda/\omega \ll 1$ in [86]).

One of the key equations in the small signal models of the microgrid components is the droop control, which is translated into

$$\frac{\mathrm{d}V_e^\theta}{\mathrm{d}t} = -M_p(P - P_o) \tag{3.26}$$

where M_p is the droop gain, and P and P_o are the measured and desired real power quantities respectively. We recognize then that, given a limited excursion of the power measurement, the droop gain M_p plays the role of modulating index. In order to ensure that the dynamic phasor model is a good approximation, the droop gain has to be *small enough*. This is, the product $M_p(P - P_o)$ has to be such that the resulting angle modulation can be considered narrow-band. It is easier to compare this to a frequency modulation case rather than phase modulation (it is shown in [88, 89] that both types of angle modulation are not essentially different): The modulation index in frequency modulation is expected to be 20% or less, and the typical frequency excursion for a droop controller is in the order of $3\,\text{Hz}$ maximum, which is 5% of the line frequency. Having a low droop gain will ensure that the dynamic phasor representation is in fact unique.

The width of the frequency band, as a function of the modulation index, is thoroughly discussed in [82]. Additional discussion is also found in [89]. An interesting study of frequency modulation of a gaussian noise modulating waveform is covered in [90, Ch.4]. A study of multitone modulation is presented in [91].

3.3.1 Dynamic phasors for linear components

For elements such as a resistor, capacitor or inductor, the dynamic phasor representation of their defining equations is not difficult to obtain.

For any two terminal device, such as the generic one shown in Figure 3.4, the voltage and current could be represented by a pair dynamic phasors

$$V_1(t) = V_1^a \cos(\omega_o t + V_1^\theta)$$
$$I_1(t) = I_1^a \cos(\omega_o t + I_1^\theta)$$

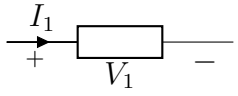

Figure 3.4: Voltage and current sign convention for dynamic phasors

The instantaneous power absorbed by the device is simply the product of the voltage and current:

$$\begin{aligned} p_1 &= V_1^a \cos(\omega_o t + V_1^\theta) \cdot I_1^a \cos(\omega_o t + I_1^\theta) \\ &= \frac{V_1^a I_1^a}{2} \left[\cos(V_1^\theta - I_1^\theta)(1 + \cos 2(\omega_o t + I_1^\theta)) - \sin(V_1^\theta - I_1^\theta) \sin 2(\omega_o t + I_1^\theta)\right] \\ &= \frac{I_1^a V_1^a}{2} \left[\cos(I_1^\theta - V_1^\theta)(1 + \cos 2(\omega_o t + V_1^\theta)) - \sin(I_1^\theta - V_1^\theta) \sin 2(\omega_o t + V_1^\theta)\right] \end{aligned} \tag{3.27}$$

For an element that stores energy, such as a capacitor or an inductor, the instantaneous power is also equal to the time derivative of its stored energy

$$p_1 = \frac{\mathrm{d}e_1}{\mathrm{d}t} \tag{3.28}$$

For example, for an inductor,

$$e_L = \frac{1}{2} L I_L^2 = \frac{1}{2} L [I_L^a \cos(\omega_o t + I_L^\theta)]^2 \tag{3.29}$$

$$p_L = \frac{\mathrm{d}e_L}{\mathrm{d}t} = \frac{L I_L^a}{2} \left[\frac{\mathrm{d}I_L^a}{\mathrm{d}t} (1 + \cos 2(\omega_o t + I_L^\theta)) - I_L^a \left(\frac{\mathrm{d}I_L^\theta}{\mathrm{d}t} - \omega_o \right) \sin 2(\omega_o t + I_L^\theta) \right] \tag{3.30}$$

Equating (3.27) and (3.30), we obtain

$$\frac{\mathrm{d}I_L^a}{\mathrm{d}t} = \frac{1}{L} V_L^a \cos(V_L^\theta - I_L^\theta) \tag{3.31}$$

$$\frac{\mathrm{d}I_L^\theta}{\mathrm{d}t} = \frac{1}{L I_L^a} V_L^a \sin(V_L^\theta - I_L^\theta) - \omega_o \tag{3.32}$$

Similarly for a capacitor,

$$\frac{\mathrm{d}V_C^a}{\mathrm{d}t} = \frac{1}{C} I_C^a \cos(I_C^\theta - V_C^\theta) \tag{3.33}$$

$$\frac{\mathrm{d}V_C^\theta}{\mathrm{d}t} = \frac{1}{C V_C^a} I_C^a \sin(I_C^\theta - V_C^\theta) - \omega_o \tag{3.34}$$

The resistor is much more simple, because it does not store energy and follows Ohm's law:

$$V_R(t) = R \cdot I_R(t) \qquad \Rightarrow \qquad \begin{aligned} V_R^a &= R \cdot I_R^a \\ V_R^\theta &= I_R^\theta \end{aligned} \tag{3.35}$$

Note that Equations (3.31) – (3.35) are readily in a form that allows their inclusion in a state-space model of a larger system that contains components of those types.

Time-invariance of dynamic phasor models for linear components

As it can be readily seen in (3.31) – (3.34), some of the differential equations are non-linear (see Section 3.3.3). However, these systems are time-invariant: by choosing the dynamic phasor representation in polar coordinates, the non-linear equations are independent of time.

It is worth noting that, for this last statement to be true, the elements that these models are representing need to be time-invariant. In addition, the frequency reference used in the dynamic phasor definition, ω_o needs to be known *a priori*. From a power system's point of view, this corresponds to the line frequency of a system operating in sinusoidal steady state. As an example of a power system's operating point calculation, see Section 5.2.

3.3.2 Dynamic phasors and steady state solutions

As with any system of the form (3.1), the sinusoidal steady state solutions for dynamic phasors, which correspond to an equilibrium point, can be found setting the time derivative of the magnitudes and phase angles equal to zero. If we do so for the capacitor and inductor cases in Equations (3.31) – (3.34), we obtain the following steady state conditions:

for the capacitor,	$I_C^A = \omega_o C V_C^A$	$I_C^\Theta - V_C^\Theta = \pi/2$	(3.36)
for the inductor,	$V_L^A = \omega_o L I_L^A$	$V_L^\Theta - I_L^\Theta = \pi/2$	(3.37)
for the resistor,	$V_R^A = R I_R^A$	$V_R^\Theta - I_L^\Theta = 0$	(3.38)

The superscripts $()^A$ and $()^\Theta$ (in uppercase) denote constant quantities that define the operating points.

3.3.3 Dynamic phasors and linearization of resulting models: incremental phasor models

Even though passive components such as the capacitor and the inductor are linear in nature, their models under the dynamic phasor representation render a non-linear set of differential equations, as shown in (3.31) – (3.34).

The non-linear relationship comes from the fact that the nominal sinusoidal excitation and response variables of components are modeled in polar coordinates. As opposed to rectangular coordinates such as the d-q reference frame, the dynamic phasor's polar coordinates do not preserve the linearity of the components' voltage and current representation. In fact, the equivalence of d-q and dynamic phasor coordinates could be presented as a transformation between rectangular and polar coordinates, which is nonlinear. Therefore, the interactions between magnitudes and phase angles in the dynamic phasor representation will be non-linear.

The dynamic phasor equations are a valid large-signal representation; to study small-signal perturbations, a linearization of those equations around an operating point provides an LTI system that can be used for stability assessment. In the same fashion of the linearization introduced in Section 3.2, a linear model can be constructed around a sinusoidal steady state operating point. Then, the stability properties of the resulting LTI system can be used to study the stability of the dynamic phasor nonlinear system.

The dynamics of this linearized model, which we call *incremental phasor model*, describe the interactions between perturbations in phasor currents and voltages $(\tilde{v}, \tilde{i})$ around the static phasor operating point $(\bar{V}, \bar{I})$, as shown in Figure 3.5. These phasors are also presented in their time-domain waveform representation in Figure 3.6. The incremental phasor model represents then the interactions between the waveforms shown at the right side of Figure 3.6.

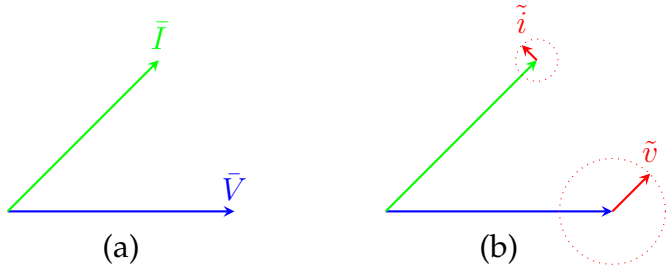

Figure 3.5: Dynamic phasor diagrams for (a) large and (b) small signals

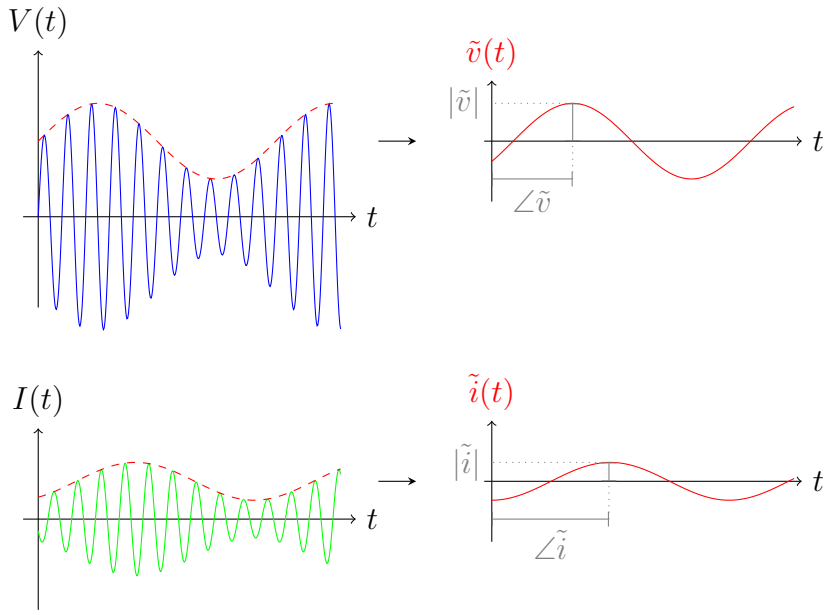

Figure 3.6: Waveforms for large and small signals shown in Figure 3.5 (not to the same scale)

In the following section, small signal models for several microgrid components will be created using this technique.

3.4 Incremental phasor models of microgrid components

In this section, the dynamic phasor analytical models of several microgrid components will be detailed, and their linearization around an operating point will be obtained. Each component is modeled in such a way that the resulting state space representation yields either an admittance or impedance. This way, the incremental phasor models can be connected together to form an impedance-admittance equivalent that resembles the block diagrams of Figure 3.3.

3.4.1 Resistive, inductive and capacitive loads

The loads are modeled as impedances, i.e. the inputs of the systems will be currents, and the outputs of the system will be voltages. The models are presented in increasing complexity order, starting from the simple resistive load to the microsource.

Resistor

The most basic load to model is a single resistor (Figure 3.7), whose representation in dynamic phasors is a direct result of Ohm's law, as shown in (3.39). R is the resistor's resistance, and $\bar{V}_R$ and $\bar{I}_R$ are the resistor's voltage and current respectively.

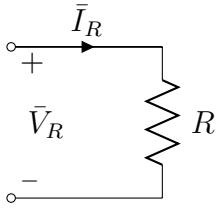

Figure 3.7: Schematic of a resistive load

$$\begin{aligned} V_R^a &= RI_R^a \\ V_R^\theta &= I_R^\theta \end{aligned} \tag{3.39}$$

As this load has no dynamics over time, and is already in a linear form, its state space representation is given by a single gain matrix. If the input and output vectors are given by

$$y = \begin{pmatrix} V_R^a \\ V_R^\theta \end{pmatrix}, \quad u = \begin{pmatrix} I_R^a \\ I_R^\theta \end{pmatrix} \tag{3.40}$$

then the state space representation is given by

$$\begin{aligned} y &= Du \\ D &= \begin{pmatrix} R & 0 \\ 0 & 1 \end{pmatrix} \end{aligned} \tag{3.41}$$

Capacitor

A capacitor is also easily modeled in an impedance state space representation. Its describing equations are shown in (3.42) for the magnitude and phase angle components, and a diagram with current and voltage references is shown in Figure 3.8.

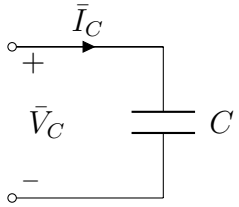

Figure 3.8: Schematic of a capacitive load

$$\begin{aligned} \frac{\mathrm{d}V_C^a}{\mathrm{d}t} &= f_1(V_C^a, V_C^\theta, I_C^a, I_C^\theta) = \frac{1}{C} I_C^a \cos(I_C^\theta - V_C^\theta) \\ \frac{\mathrm{d}V_C^\theta}{\mathrm{d}t} &= f_2(V_C^a, V_C^\theta, I_C^a, I_C^\theta) = \frac{1}{CV_C^a} I_C^a \sin(I_C^\theta - V_C^\theta) - \omega_o \end{aligned} \tag{3.42}$$

The system can be linearized around a generic operating point (V_C^A, V_C^Θ). This operating point, the steady state solution, is found setting the voltage magnitude

and phase angle time derivatives to zero:

$$\begin{array}{ll} 0 = \dfrac{1}{C} I_C^a \cos(I_C^\theta - V_C^\theta) & \\ 0 = \dfrac{1}{C V_C^a} I_C^a \sin(I_C^\theta - V_C^\theta) - \omega_o & \end{array} \quad \Rightarrow \quad \begin{array}{l} I_C^\Theta - V_C^\Theta = \dfrac{\pi}{2} \\ I_C^A = \omega_o C V_C^A \end{array} \tag{3.43}$$

Notice that this solution is the same as the one obtained by the traditional phasor algebra.

Now that the equilibrium point is known, the dynamic phasor system is linearized around it. The capacitor current $\bar{I}_C$ is chosen as the input variable, and the capacitor voltage $\bar{V}_C$ as the state (and output) variable.

$$x = \begin{pmatrix} V_C^a \\ V_C^\theta \end{pmatrix}, \quad u = \begin{pmatrix} I_C^a \\ I_C^\theta \end{pmatrix}, \quad y = x \tag{3.44}$$

The small signal quantities v_C^a and v_C^θ, which are the state variables of the linearized model, are defined in (3.45).

$$\tilde{x} = x - x_o \quad \longrightarrow \quad \begin{array}{rcl} v_C^a & = & V_C^a - V_C^A \\ v_C^\theta & = & V_C^\theta - V_C^\Theta \end{array} \tag{3.45}$$

The linearization matrices and its components are shown in (3.46) and (3.47).

$$\begin{array}{ll} \dfrac{\partial f_1}{\partial V_C^a} = 0 & \dfrac{\partial f_1}{\partial I_C^a} = 0 \\ \dfrac{\partial f_1}{\partial V_C^\theta} = \omega_o V_C^A & \dfrac{\partial f_1}{\partial I_C^\theta} = -\omega_o V_C^A \\ \dfrac{\partial f_2}{\partial V_C^a} = \dfrac{\omega_o}{V_C^A} & \dfrac{\partial f_2}{\partial I_C^a} = \dfrac{1}{C V_C^A} \\ \dfrac{\partial f_2}{\partial V_C^\theta} = 0 & \dfrac{\partial f_2}{\partial I_C^\theta} = 0 \end{array} \tag{3.46}$$

$$\begin{aligned} \dot{\tilde{x}} &= A\tilde{x} + B\tilde{u} \\ \tilde{y} &= C\tilde{x} \end{aligned}$$
$$A = \begin{pmatrix} 0 & \omega_o V_C^A \\ \frac{\omega_o}{V_C^A} & 0 \end{pmatrix} \quad B = \begin{pmatrix} 0 & -\omega_o V_C^A \\ \frac{1}{CV_C^A} & 0 \end{pmatrix} \quad C = \begin{pmatrix} 1 & 0 \\ 0 & 1 \end{pmatrix} \tag{3.47}$$

R-L load

The R-L load schematic is shown in Figure 3.9 along with the voltage and current definitions. The inductor current $\bar{I}_L$ is governed by its dynamic phasor equations shown in (3.48).

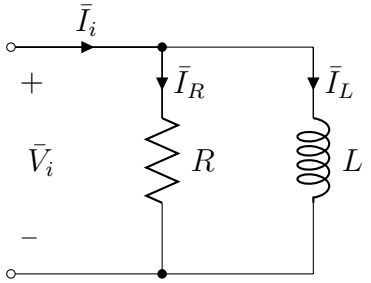

Figure 3.9: Schematic of a R-L load

$$\begin{aligned} \frac{\mathrm{d}I_L^a}{\mathrm{d}t} &= \frac{1}{L} V_L^a \cos(V_L^\theta - I_L^\theta) \\ \frac{\mathrm{d}I_L^\theta}{\mathrm{d}t} &= \frac{1}{LI_L^a} V_L^a \sin(V_L^\theta - I_L^\theta) - \omega_o \end{aligned} \tag{3.48}$$

For this load, the voltages in the inductor and the resistor are the same, i.e. $V_i^a = V_L^a = V_R^a$ and $V_i^\theta = V_L^\theta = V_R^\theta$. Using the relationships in (3.39), we can rewrite (3.48) as

$$\begin{aligned} \frac{\mathrm{d}I_L^a}{\mathrm{d}t} &= f_1(I_R^a, I_R^\theta, I_L^\theta) = \frac{1}{L} R I_R^a \cos(I_R^\theta - I_L^\theta) \\ \frac{\mathrm{d}I_L^\theta}{\mathrm{d}t} &= f_2(I_R^a, I_R^\theta, I_L^\theta) = \frac{1}{LI_L^a} R I_R^a \sin(I_R^\theta - I_L^\theta) - \omega_o \end{aligned} \tag{3.49}$$

Moreover, the resistor current can be expressed as a function of the input current $\bar{I}_i$ and the inductor current $\bar{I}_L$, which are our variables of interest (input and state variables respectively). These relationships are shown in (3.50).

$$\bar{I}_R = \bar{I}_i - \bar{I}_L \quad \Rightarrow \quad \begin{aligned} (I_R^a)^2 &= (I_i^a)^2 + (I_L^a)^2 - 2I_i^a I_L^a \cos(I_i^\theta - I_L^\theta) \\ I_R^\theta &= \arctan\left(\frac{I_i^a \sin(I_i^\theta) - I_L^a \sin(I_L^\theta)}{I_i^a \cos(I_i^\theta) - I_L^a \cos(I_L^\theta)}\right) \end{aligned} \tag{3.50}$$

Equations (3.49) and (3.50) constitute the state space model for the R-L load, where the R-L load current $\bar{I}_i$ is chosen as the input variable, the R-L load voltage $\bar{V}_i$ as the output variable, and the inductor current $\bar{I}_L$ as the state variable.

$$x = \begin{pmatrix} I_L^a \\ I_L^\theta \end{pmatrix}, \quad u = \begin{pmatrix} I_i^a \\ I_i^\theta \end{pmatrix}, \quad y = \begin{pmatrix} V_i^a \\ V_i^\theta \end{pmatrix} \tag{3.51}$$

This system can be linearized around a generic operating point $(\bar{V}_i, \bar{I}_i)$. The steady state operating point can be found, as shown for the capacitive load, using traditional phasor algebra:

$$\begin{aligned} \bar{V}_i &= \left(\frac{1}{R} + \frac{1}{j\omega_o L}\right)^{-1} \bar{I}_i \\ \bar{I}_R &= \frac{\bar{V}_i}{R} \\ \bar{I}_L &= \frac{\bar{V}_i}{j\omega_o L} \end{aligned} \tag{3.52}$$

which is equivalent to the dynamic phasor solution:

$$\begin{aligned} V_i^A &= \frac{\omega_o RL}{\sqrt{R^2 + (\omega_o L)^2}} \cdot I_i^A \qquad & I_R^A &= \frac{V_i^A}{R} \qquad & I_L^A &= \frac{V_i^A}{\omega_o L} \\ V_i^\Theta &= \arctan\left(\frac{R}{\omega_o L}\right) + I_i^\Theta \qquad & I_R^\Theta &= V_i^\Theta \qquad & I_L^\Theta &= V_i^\Theta - \frac{\pi}{2} \end{aligned} \tag{3.53}$$

Alternatively, the same solution cam be found setting the time derivatives of

inductor current magnitude and phase angle to zero and ω_o respectively.

The small signal state variables i_L^a and i_L^θ are defined in (3.54).

$$\tilde{x} = x - x_o \quad \longrightarrow \quad \begin{array}{rcl} i_L^a & = & I_L^a - I_L^A \\ i_L^\theta & = & I_L^\theta - I_L^\Theta \end{array} \tag{3.54}$$

The linearization matrices and its components are shown in (3.55), (3.56), (3.57), (3.58) and (3.59).

$$\begin{aligned}
\frac{\partial f_1}{\partial I_L^a} &= \frac{R}{LI_R^A}\left[I_L^A\cos(I_L^\Theta - I_R^\Theta) - I_i^A\cos(I_i^\Theta - I_R^\Theta)\right] = -\frac{R}{L} \\
\frac{\partial f_1}{\partial I_L^\theta} &= \frac{R}{LI_R^A}\left[-(I_i^A)^2\sin(I_L^\Theta - I_R^\Theta) - I_i^A I_L^A\sin(I_i^\Theta + I_R^\Theta - 2I_L^\Theta)\right] = \frac{R}{L}I_R^A \\
\frac{\partial f_2}{\partial I_L^a} &= \frac{R}{LI_R^A(I_L^A)^2}\left[(I_i^A)^2\sin(I_L^\Theta - I_R^\Theta) + I_i^A I_L^A\sin(I_i^\Theta + I_R^\Theta - 2I_L^\Theta)\right] = -\frac{R}{L}\frac{I_R^A}{(I_L^A)^2} \\
\frac{\partial f_2}{\partial I_L^\theta} &= \frac{R}{LI_R^A I_L^A}\left[-(I_i^A)^2\cos(I_L^\Theta - I_R^\Theta) + I_i^A I_L^A\cos(I_i^\Theta + I_R^\Theta - 2I_L^\Theta)\right] = -\frac{R}{L}
\end{aligned} \tag{3.55}$$

$$\begin{aligned}
\frac{\partial f_1}{\partial I_i^a} &= \frac{R}{LI_R^A}\left[I_i^A\cos(I_L^\Theta - I_R^\Theta) - I_L^A\cos(I_i^\Theta + I_R^\Theta - 2I_L^\Theta)\right] = \frac{R}{L}\frac{I_L^A}{I_i^A} \\
\frac{\partial f_1}{\partial I_i^\theta} &= \frac{R}{LI_R^A}\left[(I_i^A)^2\sin(I_L^\Theta - I_R^\Theta) + I_i^A I_L^A\sin(I_i^\Theta + I_R^\Theta - 2I_L^\Theta)\right] = -\frac{R}{L}I_R^A \\
\frac{\partial f_2}{\partial I_i^a} &= \frac{R}{LI_R^A I_L^A}\left[-I_i^A\sin(I_L^\Theta - I_R^\Theta) - I_L^A\sin(I_i^\Theta + I_R^\Theta - 2I_L^\Theta)\right] = \frac{R}{L}\frac{I_R^A}{I_L^A I_i^A} = \frac{\omega_o}{I_i^A} \\
\frac{\partial f_2}{\partial I_i^\theta} &= \frac{R}{LI_R^A I_L^A}\left[(I_i^A)^2\cos(I_L^\Theta - I_R^\Theta) - I_i^A I_L^A\cos(I_i^\Theta + I_R^\Theta - 2I_L^\Theta)\right] = \frac{R}{L}
\end{aligned} \tag{3.56}$$

$$
\begin{aligned}
\frac{\partial g_1}{\partial I_L^a} &= \frac{R}{I_R^A}\left[I_L^A - I_i^A\cos(I_L^\Theta - I_i^\Theta)\right] = 0 \\
\frac{\partial g_1}{\partial I_L^\theta} &= -\frac{R}{I_R^A} I_i^A I_L^A \sin(I_L^\Theta - I_i^\Theta) = R I_L^A \\
\frac{\partial g_2}{\partial I_L^a} &= \frac{I_i^A}{(I_R^A)^2}\sin(I_L^\Theta - I_i^\Theta) = -\frac{1}{I_R^A} \\
\frac{\partial g_2}{\partial I_L^\theta} &= \frac{1}{(I_R^A)^2}\left[(I_L^A)^2 - I_i^A I_L^A\cos(I_L^\Theta - I_i^\Theta)\right] = 0
\end{aligned}
\tag{3.57}
$$

$$
\begin{aligned}
\frac{\partial g_1}{\partial I_i^a} &= \frac{R}{I_R^A}\left[I_i^A - I_L^A\cos(I_L^\Theta - I_i^\Theta)\right] = R\frac{I_R^A}{I_i^A} \\
\frac{\partial g_1}{\partial I_i^\theta} &= \frac{R}{I_R^A} I_i^A I_L^A \sin(I_L^\Theta - I_i^\Theta) = -R I_L^A \\
\frac{\partial g_2}{\partial I_i^a} &= -\frac{I_i^A}{(I_R^A)^2}\sin(I_L^\Theta - I_i^\Theta) = \frac{I_L^A}{I_R^A I_i^A} \\
\frac{\partial g_2}{\partial I_i^\theta} &= \frac{1}{(I_R^A)^2}\left[(I_i^A)^2 - I_i^A I_L^A\cos(I_L^\Theta - I_i^\Theta)\right] = 1
\end{aligned}
\tag{3.58}
$$

$$
\begin{aligned}
\dot{\tilde{x}} &= A\tilde{x} + B\tilde{u} \\
\tilde{y} &= C\tilde{x} + D\tilde{u}
\end{aligned}
$$

$$
A = \begin{pmatrix} -\frac{R}{L} & \frac{R}{L}I_R^A \\ -\frac{R}{L}\frac{I_R^A}{I_L^A} & -\frac{R}{L} \end{pmatrix} \qquad B = \frac{R}{L}\begin{pmatrix} \frac{I_L^A}{I_i^A} & -I_R^A \\ \frac{I_R^A}{I_L^A I_i^A} & 1 \end{pmatrix}
$$

$$
C = \begin{pmatrix} 0 & RI_L^A \\ \frac{1}{I_R^A} & 0 \end{pmatrix} \qquad D = \begin{pmatrix} \frac{RI_R^A}{I_i^A} & -RI_L^A \\ \frac{I_L^A}{I_R^A I_i^A} & 1 \end{pmatrix}
\tag{3.59}
$$

R-C load

The R-C load schematic is shown in Figure 3.10 along with the voltage and current definitions. The development of the R-C load equations is very similar to the R-L load case.

The differential equations that govern the capacitor voltage in dynamic phasor representation are shown in (3.42).

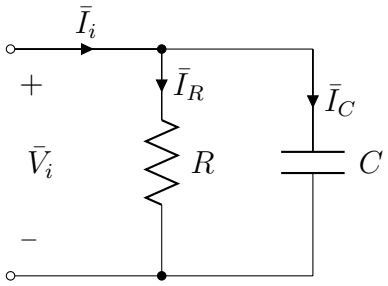

Figure 3.10: Schematic of a R-C load

On the R-C load, the voltages in the capacitor and the resistor are the same, $\bar{V}_i = \bar{V}_C = \bar{V}_R$, i.e. $V_i^a = V_R^a = V_C^a$ and $V_i^\theta = V_R^\theta = V_C^\theta$. Moreover, the resistor current can be expressed as a function of the input current $\bar{I}_i$ and the capacitor current $\bar{I}_C$: $\bar{I}_C = \bar{I}_i - \bar{I}_R$. The dynamic phasor representation of the load is then given by:

$$\begin{aligned} \frac{\mathrm{d}V_i^a}{\mathrm{d}t} &= f_1(V_i^a, V_i^\theta, I_i^a, I_i^\theta) = \frac{1}{C}\left[I_i^a \cos(I_i^\theta - V_i^\theta) - \frac{V_i^a}{R}\right] \\ \frac{\mathrm{d}V_i^\theta}{\mathrm{d}t} &= f_2(V_i^a, V_i^\theta, I_i^a, I_i^\theta) = \frac{1}{CV_i^a} I_i^a \sin(I_i^\theta - V_i^\theta) - \omega_o \end{aligned} \tag{3.60}$$

Equations (3.60) constitute the state space model for the R-C load, with $(V_C^a, V_C^\theta) = (V_i^a, V_i^\theta)$ as states (and outputs), and (I_i^a, I_i^θ) as inputs:

$$x = \begin{pmatrix} V_C^a \\ V_C^\theta \end{pmatrix}, \quad u = \begin{pmatrix} I_i^a \\ I_i^\theta \end{pmatrix}, \quad y = x \tag{3.61}$$

This system can be linearized around a generic operating point $(\bar{V}_i, \bar{I}_i)$, as it was done for the other loads. The steady state operating point can be found using

traditional phasor algebra:

$$\begin{aligned}\bar{V}_i &= \left(\frac{1}{R} + j\omega_o C\right)^{-1} \bar{I}_i \\ \bar{I}_R &= \frac{\bar{V}_i}{R} \\ \bar{I}_C &= \bar{V}_i j\omega_o C\end{aligned} \tag{3.62}$$

The small signal state variables v_C^a and v_C^θ are defined in (3.63).

$$\tilde{x} = x - x_o \quad \longrightarrow \quad \begin{aligned} v_C^a &= V_C^a - V_C^A \\ v_C^\theta &= V_C^\theta - V_C^\Theta \end{aligned} \tag{3.63}$$

The linearization matrices and its components are shown in (3.64), (3.65) and (3.66).

$$\begin{aligned}\frac{\partial f_1}{\partial V_i^a} &= -\frac{1}{RC} \\ \frac{\partial f_1}{\partial V_i^\theta} &= \frac{I_C^A}{C} \\ \frac{\partial f_2}{\partial V_i^a} &= -\frac{I_C^A}{C(V_i^A)^2} \\ \frac{\partial f_2}{\partial V_i^\theta} &= -\frac{1}{RC}\end{aligned} \tag{3.64}$$

$$\begin{aligned}\frac{\partial f_1}{\partial I_i^a} &= \frac{1}{C}\frac{I_R^A}{I_i^A} \\ \frac{\partial f_1}{\partial I_i^\theta} &= \frac{1}{C} I_C^A \\ \frac{\partial f_2}{\partial I_i^a} &= \frac{1}{C}\frac{I_C^A}{V_i^A I_i^A} \\ \frac{\partial f_2}{\partial I_i^\theta} &= \frac{1}{C}\frac{I_R^A}{V_i^A}\end{aligned} \tag{3.65}$$

$$
\begin{aligned}
\dot{\tilde{x}} &= A\tilde{x} + B\tilde{u} \\
\tilde{y} &= C\tilde{x}
\end{aligned}
$$

$$
A = \begin{pmatrix} -\frac{1}{RC} & \frac{I_C^A}{C} \\ -\frac{I_C^A}{C(V_i^A)^2} & -\frac{1}{RC} \end{pmatrix} \quad B = \frac{1}{C}\begin{pmatrix} \frac{I_R^A}{I_i^A} & I_C^A \\ \frac{I_C^A}{V_i^A I_i^A} & \frac{I_R^A}{V_i^A} \end{pmatrix} \quad C = \begin{pmatrix} 1 & 0 \\ 0 & 1 \end{pmatrix} \tag{3.66}
$$

3.4.2 Simple source

The simple source comprises an ideal voltage source with an R-L series impedance. An schematic diagram is shown in Figure 3.11. In this simple source model, the dynamic phasors $\bar{V}_e$ and $\bar{I}_L$ represent the ideal source's voltage and the current through the inductor respectively. The dynamic phasor $\bar{V}_o$ represents the voltage at the terminals.

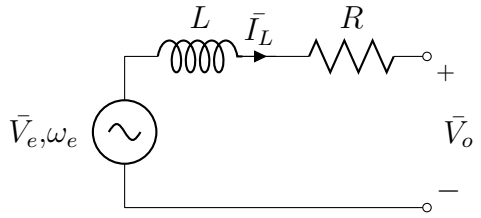

Figure 3.11: Schematic of a simple source

Following the sign references of this figure, the differential equations that describe the simple source are presented in (3.67) and (3.68).

$$
\frac{\mathrm{d}I_L^a}{\mathrm{d}t} = f_1(I_L^a, I_L^\theta, V_o^a, V_o^\theta) = \frac{1}{L}\left[V_e^a \cos(V_e^\theta - I_L^\theta) - V_o^a \cos(V_o^\theta - I_L^\theta) - RI_L^a\right] \tag{3.67}
$$

$$
\frac{\mathrm{d}I_L^\theta}{\mathrm{d}t} = f_2(I_L^a, I_L^\theta, V_o^a, V_o^\theta) = \frac{1}{LI_L^a}\left[V_e^a \sin(V_e^\theta - I_L^\theta) - V_o^a \sin(V_o^\theta - I_L^\theta)\right] - \omega_o \tag{3.68}
$$

The sinusoidal steady state equilibrium points are found when the magnitude and phase angle derivatives are equal to zero. Setting (3.67) and (3.68) to zero, we

obtain the analytical set of equations (3.69).

$$\begin{aligned} \omega_o L I_L^a &= V_e^a \sin(V_e^\theta - I_L^\theta) - V_o^a \sin(V_o^\theta - I_L^\theta) \\ R I_L^a &= V_e^a \cos(V_e^\theta - I_L^\theta) - V_o^a \cos(V_o^\theta - I_L^\theta) \end{aligned} \tag{3.69}$$

Assuming that the voltages $\bar{V}_e$ and $\bar{V}_o$ are known, we can solve for the inductor current $\bar{I}_L$ as in (3.70).

$$\begin{aligned} (I_L^A)^2 &= \frac{(V_e^A)^2 + (V_o^A)^2 - 2V_e^A V_o^A \cos(V_e^\Theta - V_o^\Theta)}{R^2 + (\omega_o L)^2} \\ I_L^\Theta &= V_e^\Theta + \arctan\left(\frac{-V_o^A \sin(V_o^\Theta - V_e^\Theta)}{V_e^A - V_o^A \cos(V_o^\Theta - V_e^\Theta)}\right) - \arcsin\left(\frac{\omega_o L}{\sqrt{R^2 + (\omega_o L)^2}}\right) \end{aligned} \tag{3.70}$$

The notation of this solution is easily simplified if we define the phasor quantities shown in (3.71) and (3.72).

$$\begin{aligned} \bar{U} &= \bar{V}_e - \bar{V}_L \\ U^A &= \sqrt{(V_e^A)^2 + (V_L^A)^2 - 2V_e^A V_L^A \cos(V_e^\Theta - V_L^\Theta)} \\ U^\Theta &= \arccos\left(\frac{V_e^A \cos(V_e^\Theta) - V_L^A \cos(V_L^\Theta)}{U^A}\right) \end{aligned} \tag{3.71}$$

$$\begin{aligned} \bar{Z} &= R + j\omega_o L \\ Z^A &= \sqrt{R^2 + (\omega_o L)^2} \\ Z^\Theta &= \arctan\left(\frac{\omega_o L}{R}\right) \end{aligned} \tag{3.72}$$

Then, the steady state solution is written in equation (3.73) in terms of these new phasor quantities. Note that the phasor $\bar{U}$ corresponds to the voltage drop in the R-L series impedance, now represented by $\bar{Z}$.

$$\begin{aligned} I_L^A &= \frac{U^A}{Z^A} \\ I_L^\Theta &= U^\Theta - Z^\Theta \end{aligned} \tag{3.73}$$

This solution is unique, and equal to the steady state solution that one would find using traditional phasor methods. A phasor diagram of this solution is shown in Figure 3.12.

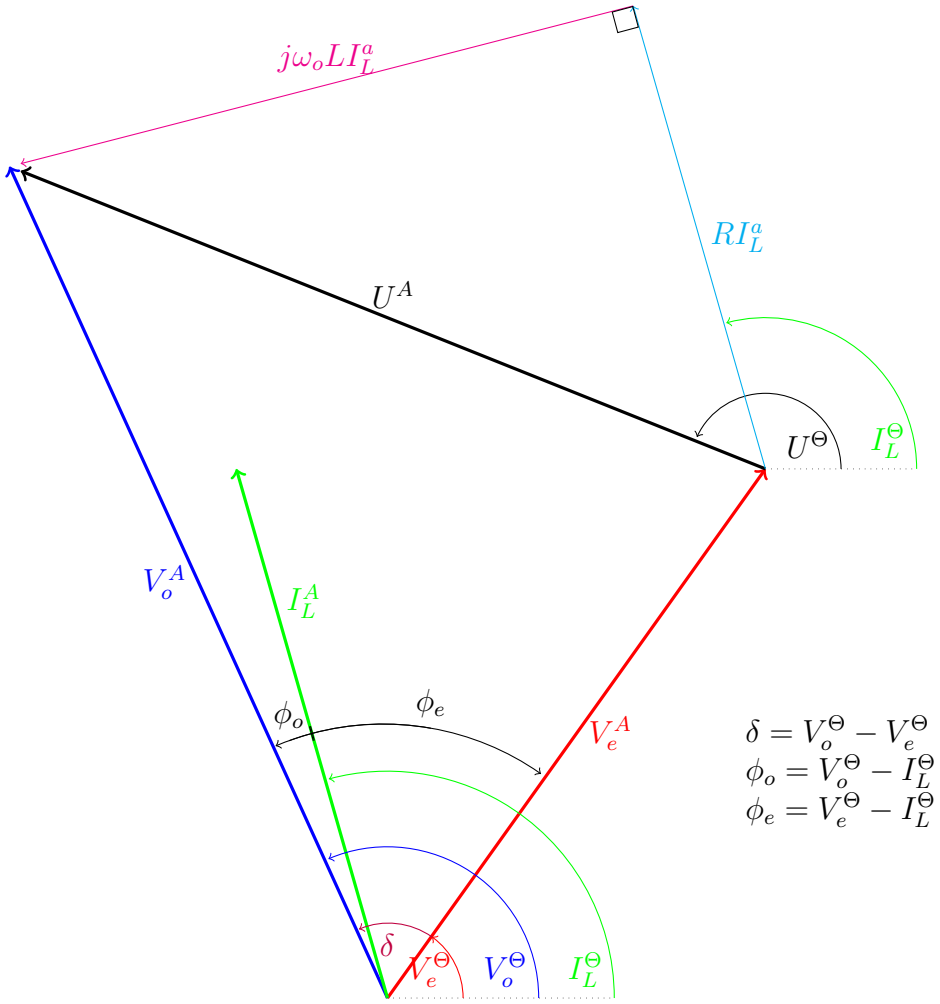

Figure 3.12: Phasor diagram of voltages and currents of the simple source in Figure 3.11.

Now that the equilibrium point is known, the dynamic system is linearized around it. The terminal voltage $\bar{V}_o$ is chosen as the input variable, and the inductor current $\bar{I}_L$ as the output variable. The ideal voltage source V_e is assumed to be constant.

$$x = \begin{pmatrix} I_L^a \\ I_L^\theta \end{pmatrix}, \quad u = \begin{pmatrix} V_o^a \\ V_o^\theta \end{pmatrix}, \quad y = \begin{pmatrix} I_L^a \\ I_L^\theta \end{pmatrix} \tag{3.74}$$

The small signal quantities i_L^a and i_L^θ are defined in (3.75).

$$\tilde{x} = x - x_o \quad \longrightarrow \quad \begin{aligned} i_L^a &= I_L^a - I_L^A \\ i_L^\theta &= I_L^\theta - I_L^\Theta \end{aligned} \tag{3.75}$$

The linearized system's matrices A and B are obtained in (3.76) and (3.77) respectively. The resulting linearized system is shown in (3.78).

$$\begin{aligned} \left.\frac{\partial f_1}{\partial x_1}\right|_{x_o} &= \left.\frac{\partial f_1}{\partial I_L^a}\right|_{x_o} &&= -\frac{R}{L} \\ \left.\frac{\partial f_1}{\partial x_2}\right|_{x_o} &= \left.\frac{\partial f_1}{\partial I_L^\theta}\right|_{x_o} &&= \frac{\omega_o U^A}{Z^A} \\ \left.\frac{\partial f_2}{\partial x_1}\right|_{x_o} &= \left.\frac{\partial f_2}{\partial I_L^a}\right|_{x_o} &&= -\frac{\omega_o Z^A}{U^A} \\ \left.\frac{\partial f_2}{\partial x_2}\right|_{x_o} &= \left.\frac{\partial f_2}{\partial I_L^\theta}\right|_{x_o} &&= -\frac{R}{L} \end{aligned} \tag{3.76}$$

$$\begin{aligned} \left.\frac{\partial f_1}{\partial u_1}\right|_{x_o} &= \left.\frac{\partial f_1}{\partial V_o^a}\right|_{x_o} &&= -\frac{1}{L}\cos(V_o^\Theta - I_L^\Theta) \\ \left.\frac{\partial f_1}{\partial u_2}\right|_{x_o} &= \left.\frac{\partial f_1}{\partial V_o^\theta}\right|_{x_o} &&= \frac{V_o^A}{L}\sin(V_o^\Theta - I_L^\Theta) \\ \left.\frac{\partial f_2}{\partial u_1}\right|_{x_o} &= \left.\frac{\partial f_2}{\partial V_o^a}\right|_{x_o} &&= -\frac{Z^A}{LU^A}\sin(V_o^\Theta - I_L^\Theta) \\ \left.\frac{\partial f_2}{\partial u_2}\right|_{x_o} &= \left.\frac{\partial f_2}{\partial V_o^\theta}\right|_{x_o} &&= -\frac{Z^A V_o^A}{LU^A}\cos(V_o^\Theta - I_L^\Theta) \end{aligned} \tag{3.77}$$

$$\begin{aligned}\dot{\tilde{x}} &= A\tilde{x} + B\tilde{u} \\ \tilde{y} &= C\tilde{x}\end{aligned}$$

$$A = \begin{pmatrix} -\frac{R}{L} & \frac{\omega_o U^A}{Z^A} \\ -\frac{\omega_o Z^A}{U^A} & -\frac{R}{L} \end{pmatrix} \qquad C = \begin{pmatrix} 1 & 0 \\ 0 & 1 \end{pmatrix} \tag{3.78}$$

$$B = \begin{pmatrix} -\frac{1}{L}\cos(V_o^\Theta - I_L^\Theta) & \frac{V_o^A}{L}\sin(V_o^\Theta - I_L^\Theta) \\ -\frac{Z^A}{LU^A}\sin(V_o^\Theta - I_L^\Theta) & -\frac{Z^A V_o^A}{LU^A}\cos(V_o^\Theta - I_L^\Theta) \end{pmatrix}$$

Note how the input and output variables are arranged. Since the inputs are voltages and the outputs are currents, any transfer function resulting from this system will have the units of an admittance.

3.4.3 Microsource

The microsource is one of the most important building blocks of the microgrid model. It is, in essence, the simple source presented in Figure 3.11, with the addition of the droop control, governed by the droop law

$$\omega = -M_p(P_{out} - P_o) + \omega_o \tag{3.79}$$

where P_o is the desired real power output at frequency ω_o, M_p is the droop gain, and P_{out} is the output power of the microsource, defined as

$$P_{out} = \frac{1}{2} V_o^a I_L^a \cos(V_o^\theta - I_L^\theta) \tag{3.80}$$

An schematic diagram is shown in Figure 3.13.

Now, the phasor angle V_e^θ will be a state of the incremental phasor system, as it is related to the frequency ω. In fact,

$$\frac{\mathrm{d}V_e^\theta}{\mathrm{d}t} = \omega - \omega_o = -M_p(P_{out} - P_o) \tag{3.81}$$

We assume the phasor magnitude V_e^a is still constant. The new state, input and

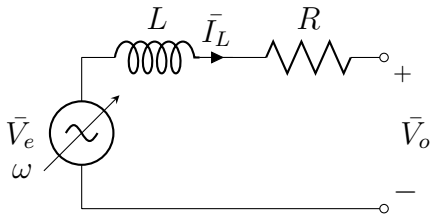

Figure 3.13: Schematic of a microsource

output vectors are presented in (3.82).

$$x = \begin{pmatrix} I_L^a \\ I_L^\theta \\ V_e^\theta \end{pmatrix}, \quad u = \begin{pmatrix} V_o^a \\ V_o^\theta \end{pmatrix}, \quad y = \begin{pmatrix} I_L^a \\ I_L^\theta \end{pmatrix} \tag{3.82}$$

The dynamics of the R-L series impedance are still given by equations (3.67) and (3.68). However, these are now function of V_e^θ also. Nevertheless, they have the same form, as shown in (3.83) and (3.84). The additional differential equation includes the dynamics introduced by the droop control, as shown in equation (3.85).

$$\frac{\mathrm{d}I_L^a}{\mathrm{d}t} = f_1(I_L^a, I_L^\theta, V_o^a, V_o^\theta, V_e^\theta) = \frac{1}{L}\left[V_e^a \cos(V_e^\theta - I_L^\theta) - V_o^a \cos(V_o^\theta - I_L^\theta) - RI_L^a\right] \tag{3.83}$$

$$\frac{\mathrm{d}I_L^\theta}{\mathrm{d}t} = f_2(I_L^a, I_L^\theta, V_o^a, V_o^\theta, V_e^\theta) = \frac{1}{LI_L^a}\left[V_e^a \sin(V_e^\theta - I_L^\theta) - V_o^a \sin(V_o^\theta - I_L^\theta)\right] - \omega_o \tag{3.84}$$

$$\frac{\mathrm{d}V_e^\theta}{\mathrm{d}t} = f_3(I_L^a, I_L^\theta, V_o^a, V_o^\theta, V_e^\theta) = -M_p\left(\frac{1}{2}V_o^a I_L^a \cos(V_o^\theta - I_L^\theta) - P_o\right) \tag{3.85}$$

For the sinusoidal steady state equilibrium point, the solutions still follow the same equations (3.73) and (3.73). However, there is an additional condition over the new state variable. This new condition is the steady state operation of the droop controller, in which $\frac{\mathrm{d}V_e^\theta}{\mathrm{d}t} = 0$, i.e.

$$\frac{1}{2}V_o^a I_L^a \cos(V_o^\theta - I_L^\theta) = P_o \tag{3.86}$$

The linearization will incorporate new components to the incremental phasor model, increasing its order to three. The new dynamics appear as additional components of the A matrix obtained in (3.87) and (3.88).

$$\begin{aligned} \left.\frac{\partial f_1}{\partial x_3}\right|_{x_o} &= \left.\frac{\partial f_1}{\partial V_e^\theta}\right|_{x_o} &&= -\frac{V_e^A}{L}\sin(V_e^\Theta - I_L^\Theta) \\ \left.\frac{\partial f_2}{\partial x_3}\right|_{x_o} &= \left.\frac{\partial f_2}{\partial V_e^\theta}\right|_{x_o} &&= \frac{Z^A V_e^A}{U^A L}\cos(V_e^\Theta - I_L^\Theta) \end{aligned} \tag{3.87}$$

$$\begin{aligned} \left.\frac{\partial f_3}{\partial x_1}\right|_{x_o} &= \left.\frac{\partial f_3}{\partial I_L^a}\right|_{x_o} &&= -\frac{M_p}{2}V_o^A\cos(V_o^\Theta - I_L^\Theta) \\ \left.\frac{\partial f_3}{\partial x_2}\right|_{x_o} &= \left.\frac{\partial f_3}{\partial I_L^\theta}\right|_{x_o} &&= -\frac{M_p}{2}V_o^A I_L^A\sin(V_o^\Theta - I_L^\Theta) \\ \left.\frac{\partial f_3}{\partial x_3}\right|_{x_o} &= \left.\frac{\partial f_3}{\partial V_e^\theta}\right|_{x_o} &&= 0 \end{aligned} \tag{3.88}$$

There will also be new components for the B matrix, as the input will also interact with the new state V_e^θ. The new components are derived in (3.89) and the resulting incremental phasor system is shown in (3.90).

$$\begin{aligned} \left.\frac{\partial f_3}{\partial u_1}\right|_{x_o} &= \left.\frac{\partial f_3}{\partial V_o^a}\right|_{x_o} &&= -\frac{M_p}{2}I_L^A\cos(V_o^\Theta - I_L^\Theta) \\ \left.\frac{\partial f_3}{\partial u_2}\right|_{x_o} &= \left.\frac{\partial f_3}{\partial V_o^\theta}\right|_{x_o} &&= \frac{M_p}{2}V_o^A I_L^A\sin(V_o^\Theta - I_L^\Theta) \end{aligned} \tag{3.89}$$

$$
\begin{aligned}
\dot{\tilde{x}} &= A\tilde{x} + B\tilde{u} \\
\tilde{y} &= C\tilde{x}
\end{aligned}
$$

$$
A = \begin{pmatrix}
-\frac{R}{L} & \frac{\omega_o U^A}{Z^A} & -\frac{V_e^A}{L}\sin(V_e^\Theta - I_L^\Theta) \\
-\frac{\omega_o Z^A}{U^A} & -\frac{R}{L} & \frac{Z^A V_e^A}{U^A L}\cos(V_e^\Theta - I_L^\Theta) \\
-\frac{M_p}{2}V_o^A\cos(V_o^\Theta - I_L^\Theta) & -\frac{M_p}{2}V_o^A I_L^A\sin(V_o^\Theta - I_L^\Theta) & 0
\end{pmatrix}
$$

$$
B = \begin{pmatrix}
-\frac{1}{L}\cos(V_o^\Theta - I_L^\Theta) & \frac{V_o^A}{L}\sin(V_o^\Theta - I_L^\Theta) \\
-\frac{Z^A}{LU^A}\sin(V_o^\Theta - I_L^\Theta) & -\frac{Z^A V_o^A}{LU^A}\cos(V_o^\Theta - I_L^\Theta) \\
-\frac{M_p}{2}I_L^A\cos(V_o^\Theta - I_L^\Theta) & \frac{M_p}{2}V_o^A I_L^A\sin(V_o^\Theta - I_L^\Theta)
\end{pmatrix}
$$

$$
C = \begin{pmatrix} 1 & 0 & 0 \\ 0 & 1 & 0 \end{pmatrix}
\tag{3.90}
$$

3.4.4 Microsource with power measurement filter

It is customary to use a filter on the power measurements in the system to reject noises such as those generated by imbalances and harmonic content. One type of filter usually found in literature [44, 46, 36] is the first order low-pass filter, whose Laplace domain transfer function is

$$
H_{filter}(s) = \frac{P_f(s)}{P_{out}(s)} = \frac{\omega_c}{s + \omega_c} \tag{3.91}
$$

where ω_c is the cutoff frequency of the filter, P_{out} is the measured active power and P_f is the filtered active power. Adding such filter to the power measurement of the droop controlled microsource will increase the system's order in one.

The new droop control rule is

$$
\omega = -M_p(P_f - P_o) + \omega_o \tag{3.92}
$$

where P_f is now the filtered power measurement, and P_o is the desired real power output at frequency ω_o. This measurement comes from the measurement filter,

which is governed by equation (3.93). The measured output power P_{out} is defined in (3.80).

The time-domain differential equation for the power filter can be derived using the inverse Laplace transform on the transfer function of (3.91):

$$\begin{aligned} & \mathcal{L}(P_f) = \frac{\omega_c}{s+\omega_c}\,\mathcal{L}(P_{out}) \\ \Leftrightarrow \quad & s\,\mathcal{L}(P_f) + \omega_c\,\mathcal{L}(P_f) = \omega_c\,\mathcal{L}(P_{out}) \\ \Leftrightarrow \quad & s\,\mathcal{L}(P_f) = \omega_c\,[\mathcal{L}(P_{out}) - \mathcal{L}(P_f)] \qquad / \mathcal{L}^{-1} \\ \Leftrightarrow \quad & \frac{\mathrm{d}P_f}{\mathrm{d}t} = \omega_c\,[P_{out} - P_f] \end{aligned} \tag{3.93}$$

With this changes, the incremental phasor model of the system is represented by a new set of equations:

$$\frac{\mathrm{d}I_L^a}{\mathrm{d}t} = f_1(I_L^a, I_L^\theta, V_o^a, V_o^\theta, V_e^\theta, P_f) = \frac{1}{L}\left[V_e^a\cos(V_e^\theta - I_L^\theta) - V_o^a\cos(V_o^\theta - I_L^\theta) - RI_L^a\right] \tag{3.94}$$

$$\frac{\mathrm{d}I_L^\theta}{\mathrm{d}t} = f_2(I_L^a, I_L^\theta, V_o^a, V_o^\theta, V_e^\theta, P_f) = \frac{1}{LI_L^a}\left[V_e^a\sin(V_e^\theta - I_L^\theta) - V_o^a\sin(V_o^\theta - I_L^\theta)\right] - \omega_o \tag{3.95}$$

$$\frac{\mathrm{d}V_e^\theta}{\mathrm{d}t} = f_3(I_L^a, I_L^\theta, V_o^a, V_o^\theta, V_e^\theta, P_f) = -M_p(P_f - P_o) \tag{3.96}$$

$$\frac{\mathrm{d}P_f}{\mathrm{d}t} = f_4(I_L^a, I_L^\theta, V_o^a, V_o^\theta, V_e^\theta, P_f) = \omega_c\left(\frac{1}{2}V_o^a I_L^a\cos(V_o^\theta - I_L^\theta) - P_f\right) \tag{3.97}$$

Note that the incorporation of the filter does not impact the differential equations f_1 and f_2. However, f_3 is changed and a new equation f_4 appears. The modified components of f_3 are shown in (3.98) and (3.100), and the new components for the linearization of f_4 are shown in (3.99) and (3.101). The incremental phasor model is presented in (3.102).

$$\begin{aligned}
\left.\frac{\partial f_3}{\partial x_1}\right|_{x_o} &= \left.\frac{\partial f_3}{\partial I_L^a}\right|_{x_o} &=0\\
\left.\frac{\partial f_3}{\partial x_2}\right|_{x_o} &= \left.\frac{\partial f_3}{\partial I_L^\theta}\right|_{x_o} &=0\\
\left.\frac{\partial f_3}{\partial x_3}\right|_{x_o} &= \left.\frac{\partial f_3}{\partial V_e^\theta}\right|_{x_o} &=0\\
\left.\frac{\partial f_3}{\partial x_4}\right|_{x_o} &= \left.\frac{\partial f_3}{\partial P_f}\right|_{x_o} &=-M_p
\end{aligned} \tag{3.98}$$

$$\begin{aligned}
\left.\frac{\partial f_4}{\partial x_1}\right|_{x_o} &= \left.\frac{\partial f_4}{\partial I_L^a}\right|_{x_o} &=-\frac{\omega_c}{2}V_o^A\cos(V_o^\Theta - I_L^\Theta)\\
\left.\frac{\partial f_4}{\partial x_2}\right|_{x_o} &= \left.\frac{\partial f_4}{\partial I_L^\theta}\right|_{x_o} &=-\frac{\omega_c}{2}V_o^A I_L^A\sin(V_o^\Theta - I_L^\Theta)\\
\left.\frac{\partial f_4}{\partial x_3}\right|_{x_o} &= \left.\frac{\partial f_4}{\partial V_e^\theta}\right|_{x_o} &=0\\
\left.\frac{\partial f_4}{\partial x_3}\right|_{x_o} &= \left.\frac{\partial f_4}{\partial P_f}\right|_{x_o} &=-\omega_c
\end{aligned} \tag{3.99}$$

$$\begin{aligned}
\left.\frac{\partial f_3}{\partial u_1}\right|_{x_o} &= \left.\frac{\partial f_3}{\partial V_o^a}\right|_{x_o} &=0\\
\left.\frac{\partial f_3}{\partial u_2}\right|_{x_o} &= \left.\frac{\partial f_3}{\partial V_o^\theta}\right|_{x_o} &=0
\end{aligned} \tag{3.100}$$

$$\begin{aligned}
\left.\frac{\partial f_4}{\partial u_1}\right|_{x_o} &= \left.\frac{\partial f_4}{\partial V_o^a}\right|_{x_o} &=-\frac{\omega_c}{2}I_L^A\cos(V_o^\Theta - I_L^\Theta)\\
\left.\frac{\partial f_4}{\partial u_2}\right|_{x_o} &= \left.\frac{\partial f_4}{\partial V_o^\theta}\right|_{x_o} &=\frac{\omega_c}{2}V_o^A I_L^A\sin(V_o^\Theta - I_L^\Theta)
\end{aligned} \tag{3.101}$$

$$
\begin{aligned}
\dot{\tilde{x}} &= A\tilde{x} + B\tilde{u} \\
\tilde{y} &= C\tilde{x}
\end{aligned}
$$

$$
A = \begin{pmatrix}
-\frac{R}{L} & \frac{\omega_o U^A}{Z^A} & -\frac{V_e^A}{L}\sin(V_e^\Theta - I_L^\Theta) & 0 \\
-\frac{\omega_o Z^A}{U^A} & -\frac{R}{L} & \frac{Z^A V_e^A}{U^A L}\cos(V_e^\Theta - I_L^\Theta) & 0 \\
0 & 0 & 0 & -M_p \\
-\frac{\omega_c}{2} V_o^A \cos(V_o^\Theta - I_L^\Theta) & -\frac{\omega_c}{2} V_o^A I_L^A \sin(V_o^\Theta - I_L^\Theta) & 0 & -\omega_c
\end{pmatrix}
$$

$$
B = \begin{pmatrix}
-\frac{1}{L}\cos(V_o^\Theta - I_L^\Theta) & \frac{V_o^A}{L}\sin(V_o^\Theta - I_L^\Theta) \\
-\frac{Z^A}{LU^A}\sin(V_o^\Theta - I_L^\Theta) & -\frac{Z^A V_o^A}{LU^A}\cos(V_o^\Theta - I_L^\Theta) \\
0 & 0 \\
-\frac{\omega_c}{2} I_L^A \cos(V_o^\Theta - I_L^\Theta) & \frac{\omega_c}{2} V_o^A I_L^A \sin(V_o^\Theta - I_L^\Theta)
\end{pmatrix}
$$

$$
C = \begin{pmatrix} 1 & 0 & 0 & 0 \\ 0 & 1 & 0 & 0 \end{pmatrix}
$$

(3.102)

3.5 Interpretation of the incremental phasor models

The admittance and impedance representations deserve a careful look, as the magnitude/angle representation yields quantities that are easily related to physical quantities, but are not necessarily intuitive. In fact, contrary to common sense, the magnitude and phase angles of the small perturbations are, in principle, not related to the large signal excursions, as depicted in Figure 3.5.

The natural way of thinking is to relate voltages and currents through an impedance or admittance, a complex-valued quantity. The small signal representation, however, relates vectors by channels as individual components, each of which will be an impedance-like or admittance-like quantity.

For example, the transfer function matrix for the simple source, obtained from (3.78) as

$$H(s) = \frac{\tilde{y}(s)}{\tilde{u}(s)} = \frac{\tilde{i}(s)}{\tilde{v}(s)} = C \cdot (sI - A)^{-1} \cdot B \tag{3.103}$$

is a 2-by-2 matrix whose elements are all small-signal "admittances" over the magnitude and phase angle components

$$H(s) = \begin{pmatrix} H^{a,a}(s) & H^{a,\theta}(s) \\ H^{\theta,a}(s) & H^{\theta,\theta}(s) \end{pmatrix} \tag{3.104}$$

These small-signal "admittances" provide information about how perturbations in a given channel are affecting another channel on the LTI model. For example, $H^{a,\theta}(s)$ provides information about how perturbations in the small-signal current *phase angle* $\tilde{i}^{\theta}$ affects the small-signal voltage *magnitude* $\tilde{v}^{a}$. Graphically, using the designations of Figure 3.5, the relationship is governing how rotations of $\tilde{i}$ are making the radius of the dotted line circle around $\tilde{v}$ grow or shrink. That relationship is a Laplace-domain transfer function that, evaluated in $s = j\omega$, yields an admittance. However this particular admittance will not relate the whole current and voltage vectors, but only the current *phase angle* with the voltage *magnitude*.

The appearance of cross-coupled impedances and admittances is not a matter of the incremental phasor representation only. In fact, d-q models have also equivalent cross-coupled impedances and admittances [63], usually called Z_{dd}, Z_{dq}, and so on. However, it is worthy to note that the impedances and admittances in d-q components have the right physical units of Ohms and Mhos; the dynamic phasor components, in contrast, do not always have the right physical units or readily interpretable physical significance. When establishing the conditions for stability on the basis of impedance matching, the magnitude channels will be the only ones that provide physical significance. Our interest is, then, in the magnitude channel component, $H^{a,a}(s)$, which we will call *incremental phasor impedance* $\tilde{Z}(s)$ or *incremental phasor admittance* $\tilde{Y}(s)$ depending on the state space formulation.

Even though the system's stability properties will be dictated by the interaction of all magnitude and phase angle channels, as in any multiple-input-multiple-output (MIMO) system, it will be shown in the rest of this document that the stability

properties can be, in fact, studied by the interactions of the magnitude-magnitude components $H^{a,a}(s)$ only. This effectively represents the MIMO system as a single-input-single-output (SISO) system. The generalized Nyquist stability criterion, developed for MIMO systems, is simplified to the traditional Nyquist stability criterion for SISO systems [12]. This simplification is inspired by the developments presented in [63], in which the stability of a system is solely determined by looking at the d-d channel in a d-q reference frame analysis.

3.5.1 Incremental phasor impedances in the dynamic phasor representation

The simplest case is the resistive load, in which both the large-signal and small-signal (incremental) phasor impedances are equal:

$$Z_R(s) = \tilde{Z}_R(s) = R \tag{3.105}$$

However, as soon as dynamics come into play, the large-signal impedance $Z(s)$ and incremental impedance $\tilde{Z}(s)$ begin to differ. For example, in the case of the capacitive load, the large-signal impedance is

$$Z_C(s) = \frac{1}{sC} \tag{3.106}$$

and the incremental phasor impedance, obtained from (3.47) is

$$\tilde{Z}_C(s) = |Z(j\omega_o)| \cdot \frac{\omega_o^2}{s^2 + \omega_o^2} \tag{3.107}$$

In this particular example, we can see how the incremental phasor impedance has a "DC gain" equal to the large-signal impedance evaluated at the system's frequency, and a pair of complex-conjugate poles that lie on the imaginary axis, also at the system's frequency. This phenomenon can be seen as a "pole-splitting" characteristic: the original pole of the large-signal impedance, located at the origin,

is split into two poles, which move from the original pole's location towards $\pm j$.

Another example is the R-C load, in which the large-signal impedance's pole is not at the origin anymore. The large- and incremental phasor impedances are

$$Z_{R-C}(s) = \frac{R \cdot \frac{1}{sC}}{R + \frac{1}{sC}} = \frac{1}{C} \cdot \frac{1}{s + \frac{1}{RC}} \tag{3.108}$$

$$\tilde{Z}_{R-C}(s) = |Z(j\omega_o)| \cdot \frac{\frac{1}{RC}s + \frac{1}{(RC)^2} + \omega_o^2}{s^2 + \frac{2}{RC}s + \frac{1}{(RC)^2} + \omega_o^2} \tag{3.109}$$

In a similar fashion, the single negative real pole is split into two complex conjugate poles that move from the original pole location towards $\pm j$, and an extra zero appears as well. Note how the "DC gain" of the incremental phasor impedance is, once again, equal to the large-signal impedance evaluated at the system's frequency. Some example Bode plots and pole-zero maps of the large- and incremental phasor impedances are shown in Figure 3.14.

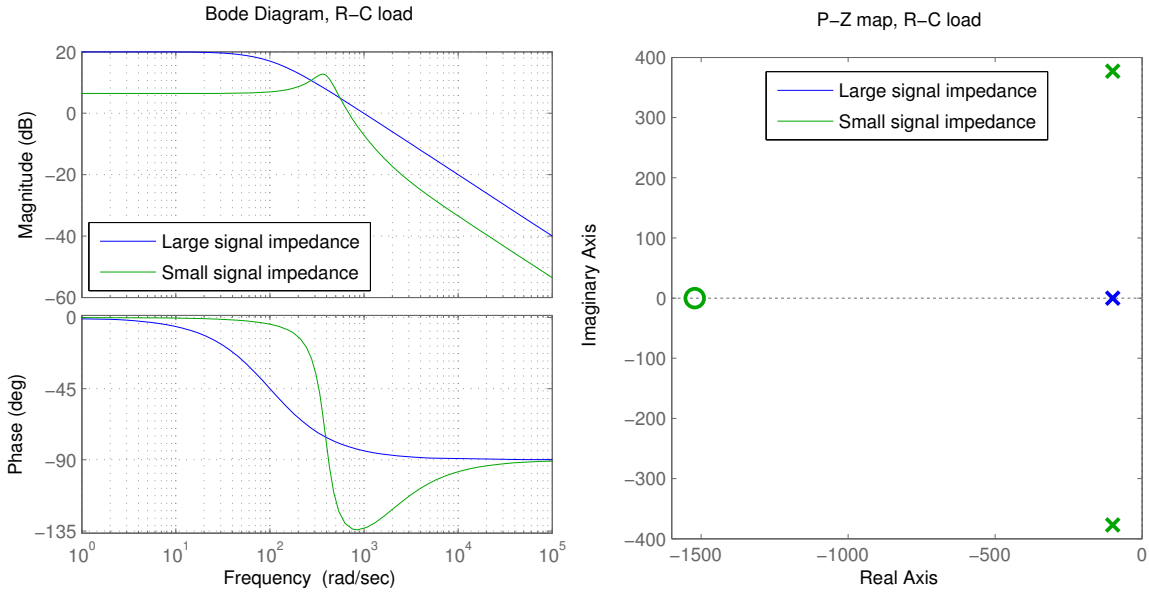

Figure 3.14: Example Bode plot and pole-zero map of the R-C load large-signal and incremental phasor impedances

The same analysis can be done with the R-L load, which shows a slightly different structure. The large-signal and incremental phasor impedances in this case are

$$Z_{R-L}(s) = \frac{sRL}{R+sL} = R\frac{s}{s+\frac{R}{L}} \tag{3.110}$$

$$\tilde{Z}_{R-L}(s) = |Z(j\omega_o)| \cdot \frac{s^2 + 3\frac{R}{L}s + \left(\frac{R^2}{L^2} + \omega_o^2\right)}{s^2 + 2\frac{R}{L}s + \left(\frac{R^2}{L^2} + \omega_o^2\right)} \tag{3.111}$$

The large-signal impedance has one pole and one zero, and the incremental phasor impedance has two poles and two zeros. The pole-splitting phenomenon in this case is rather different, however the "DC gain" of the incremental phasor impedance is still equal to the large-signal impedance evaluated at the system's frequency. Some example Bode plots and pole-zero maps of the large-signal and incremental phasor impedances of the R-L load are shown in Figure 3.15.

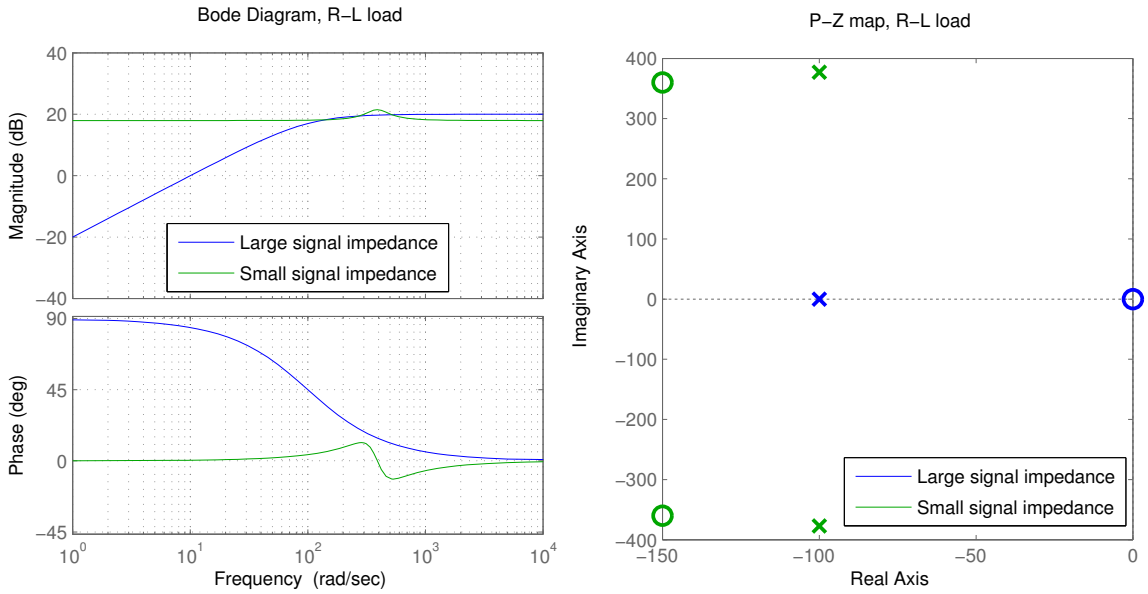

Figure 3.15: Example Bode plot and pole-zero map of the R-L load large-signal and incremental phasor impedances

In the case of the microsource analytical model, the expression for its admittance

is much more complex, as shown in (3.112). The numerator and denominator of this admittance are functions of the droop gain M_p. Some of the amplitudes and phase angles present in this equation are already defined in the phasor diagram of Figure 3.12.

$$\begin{aligned}\tilde{Y}_{usrc}(s) = & -\frac{1}{\Delta(s)} \cdot \frac{1}{Z^A} \cdot \left[\frac{Z^A}{L} \cos\phi_L s^2 + \frac{1}{L^2} \left({Z^A}^2 \cos(\phi_L - \varphi) - \frac{1}{2} L M_p V_e^A U \sin\phi_e \cos\phi_L \right) s \right. \\ & \left. + \frac{1}{2L^2} Z^A M_p V_e^A \left(V_o^A \sin\phi_L + U \sin(\varphi - \phi_e) \cos\phi_L \right) \right] \\ \Delta(s) = & \, s^3 + \frac{2R}{L} s^2 + \frac{1}{L^2} \left({Z^A}^2 + \frac{1}{2} L M_p V_e^A V_o^A \sin(\delta) \right) s + \frac{1}{2L^2} Z^A M_p V_e^A V_o^A \sin(\delta + \varphi)\end{aligned} \tag{3.112}$$

In this case, the DC gain of the incremental phasor admittance is equal to

$$\tilde{Y}_{usrc}(0) = -\frac{1}{Z^A} \frac{V_o^A \sin\phi_L + U \sin(\varphi - \phi_e) \cos\phi_L}{V_o^A \sin(\delta + \varphi)} \tag{3.113}$$

expression that preserves information about the large-signal series impedance (represented by Z^A), but also the operating point of the microsource (represented by the rest of the terms). Example bode plots of the incremental phasor impedance of the microsource can be found later in this document, for example in Figure 4.15.

These admittances and impedances will play a crucial role in the stability assessment of the microgrid, as will be shown in the following chapters.

3.6 Time-domain simulation models

The time-domain simulation models are constructed in Simulink, using SimPowerSystems blocks for the power system wiring.

A general overview of the system is shown in Figure 3.16, in which a three-phase, two-source microgrid is presented. This general model is modified for each specific simulation scenario, by adding, deleting or modifying its blocks.

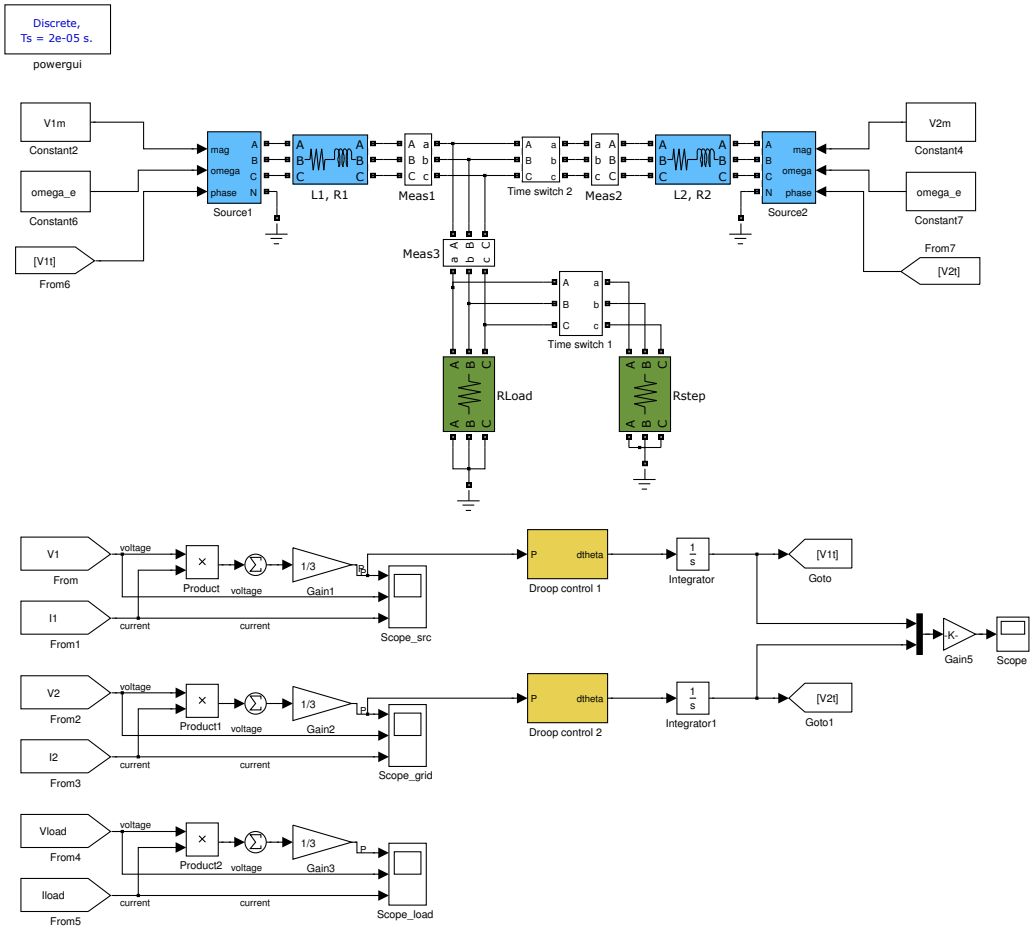

Figure 3.16: Overview of the 2-source microgrid simulation block diagram

The upper part of the block diagram corresponds to the power section, in which the electric elements interact. The lower part corresponds to the control section, in which the measurements are fed into the controllers, and control signals are delivered.

Each of the analytical models presented in the previous section has an equivalent for time-domain simulation, whose details are presented below.

3.6.1 Resistive, inductive and capacitive loads

Each passive load is already available as a SymPowerSystems block. The load blocks are shown in Figure 3.17.

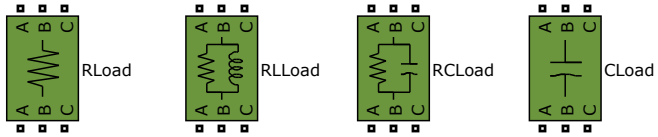

Figure 3.17: Collection of load block diagrams

3.6.2 Simple source

The simple source model is shown in Figure 3.18. It comprises an ideal voltage source and a series R-L impedance. The ideal voltage source is fed with constant voltage magnitude (V1m), frequency (omega_e) and phase angle (V1t). These quantities, however, may be connected to other blocks to introduce several controls, such as the frequency droop.

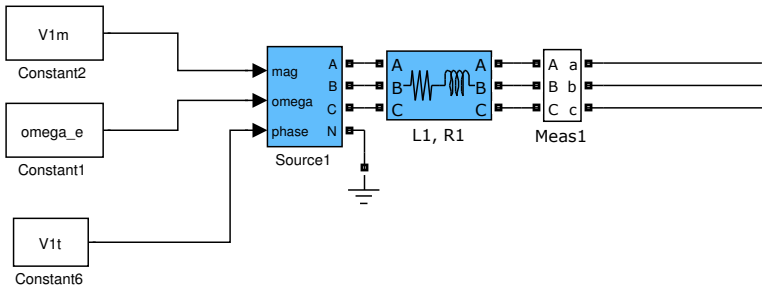

Figure 3.18: Simple source block diagram

Internally, the ideal voltage source is built using three ideal, wye-connected controlled voltage sources, which are fed with symmetric, balanced sinusoidal references. The block diagram of the ideal voltage source is shown in Figure 3.19.

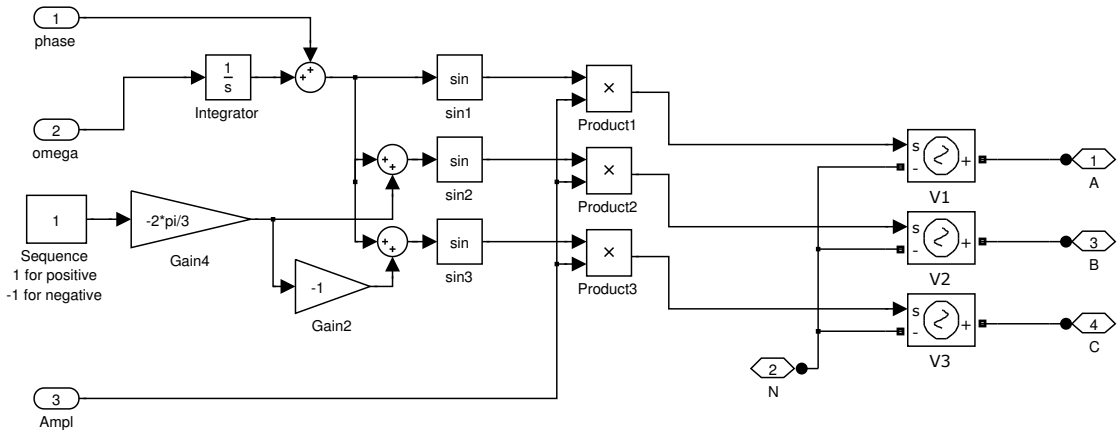

Figure 3.19: Simple source block diagram details: ideal three-phase controlled voltage source

3.6.3 Microsource

When the droop control is introduced, the frequency of the microsource varies as a function of the delivered power. The droop control block is fed with the three phase power measurement (scaled by $1/3$), and delivers $\frac{\mathrm{d}V^{\theta}}{\mathrm{d}t}$ at the output, as shown in Figure 3.20 as dtheta. The output of this block is connected to an integrator, to finally deliver the microsource's phase angle V^{θ}. The power measurement in the three phase case is remarkably simple. However, in other configurations such as a single-phase microgrid, the power measurement might be a more complex block.

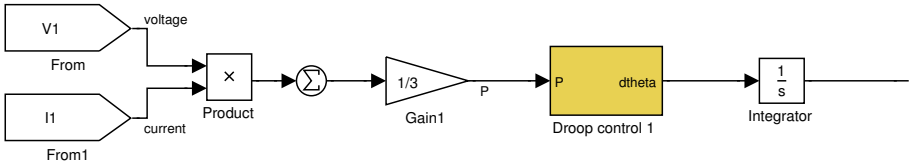

Figure 3.20: Droop control block diagram

The droop control internals are shown in Figure 3.21. This block is implementing Equation (3.81), with an output power setpoint Pb1 and droop gain Mp1.

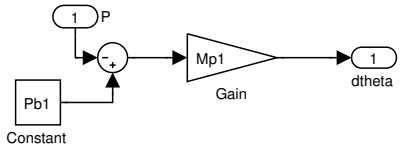

Figure 3.21: Droop control block diagram details

3.6.4 Microsource with power measurement filter

This version of the microsource only differs from the previous one in the additional filter block introduced after the power calculation, shown in Figure 3.22.

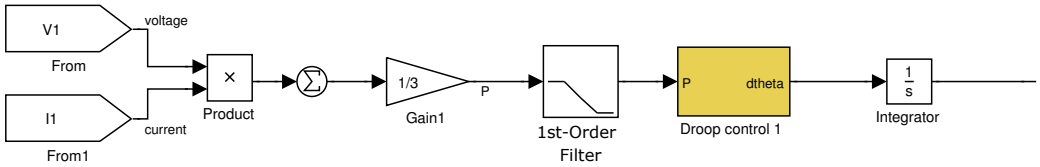

Figure 3.22: Droop control with power measurement filter block diagram

3.7 Parameters

The parameters shown in Table 3.1 are used throughout every numerical and time-domain simulation in the following chapters. Whenever a component is present in the system, its parameters will be the ones presented in this table, unless otherwise noted.

These parameters try to resemble the existing UW-Microgrid hardware. In fact, several values are equal to the measured parameters of the microsources in the UW-Microgrid. Note, however, that some parameters can be tuned during simulations and experiments, such as the droop gains M_p and the power measurement filter cut-off frequency ω_c.

Table 3.1: Base parameters for 2-source microgrid

Parameter	Symbol	Value	Units
System's frequency	f_o	60	Hz
System's angular frequency	ω_o	377	rad s^{-1}
Microsource resistance	$R_{1,2}$	0.0188	Ω
Microsource inductance	$L_{1,2}$	0.62	mH
Microsource 1 voltage magnitude	V_{e1}^{A}	$120\sqrt{2}$	V
Microsource 2 voltage magnitude	V_{e2}^{A}	$115\sqrt{2}$	V
Microsource 1 voltage angle	V_{e1}^{Θ}	0.05π	rad
Microsource 2 voltage angle	V_{e2}^{Θ}	0	rad
Load resistance	R_L	10	Ω
Load capacitance	C_L	10	µF
Load inductance	L_L	10	H
Microsource droop gain	$M_{p1,2}$	0.1	%
Microsource power filter cut-off frequency	ω_c	30	Hz

3.8 Summary

In this chapter, the ideas behind the impedance matching criteria were introduced. Then, the dynamic phasor analytical model of several microgrid components was developed in such a way that the models can be interconnected. This is, the output current of one model serves as the input current of another, and likewise with the voltages.

Even though the models are already useful as such for stability analysis (using for example eigenvalue analysis), the key definition also introduced in this chapter is the incremental phasor impedance or admittance. This corresponds to the magnitude/magnitude channel of the resulting transfer function of a given component, $H^{a,a}(s)$, which will become the fundamental descriptor of such component for the impedance matching analysis. Its successful application will be shown in the following chapters.

In addition, the same components modeled on dynamic phasor were also modeled on the simulation software package Simulink. These models have the same

structure of the analytical models, and will be used later to validate the analytical dynamic phasor models.

4 SINGLE SOURCE MICROGRID

A single source microgrid is, for the purposes of this chapter, a microsource connected to either an infinite bus (such as the system depicted in 4.1) or a single load. For a microsource connected to a larger, more complex system, the approach shown in the subsequent chapter may be used.

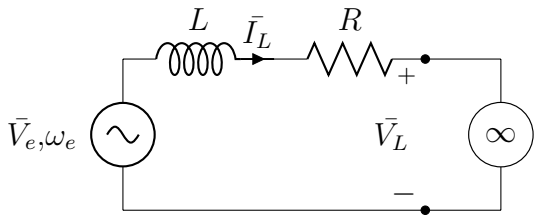

Figure 4.1: One source, infinite bus system

Since the single source case has been thoroughly studied [35, 36, 51], the results obtained in this chapter may serve as a validation of the small perturbation models obtained using dynamic phasors. Hence, the purpose of this chapter is to validate the tools developed in the previous chapter when applied to the stability analysis of a microgrid.

In this chapter, two kinds of single source microgrids will be studied. First, the *single microsource, infinite bus* system will be analytically studied for two reasons: (a) the analytical analysis will serve as a validation process for the dynamic phasor modeling technique, because the results can be directly compared to the analytical results reported on the literature; and (b) the infinite bus, being ideal and having no series impedance, cannot be used with the impedance matching criteria, since the loop gain $Y_1 Z_2$ term becomes zero, leading to an indeterminate form. As part of the validation, the single microsource, infinite bus case will also be numerically studied, and time-domain simulations will be performed as well.

Second, cases of a *single microsource connected to passive loads* will be presented. Even though this system could also be analytically studied using classical eigenvalue methods, the approach used in this case will be to study the stability through the

impedance matching criteria. Numerical results will be contrasted to time-domain simulations.

4.1 Single microsource, infinite busbar

Infinite bus is a term borrowed from large EPS analysis (for example, see [27, Ch. 7]). In such systems, the infinite bus usually represents a large part of the EPS, which is assumed to have infinite power capacity and inertia. Even though the impedance matching stability criteria cannot be applied in this specific case, a deep analysis of the single microsource, infinite bus system will provide meaningful insights on how the dynamics of the system are function of the several parameters of a microsource, specially the droop gain M_p.

As the dynamics of the system increase (i.e. the order of the linearized system increases), it becomes rather difficult to establish any kind of closed-form solution. However, the single microsource, infinite bus system is one of the cases that can be studied in detail, and serves as an intermediate step in understanding the behavior of a larger microgrid.

4.1.1 Closed-form solutions

When a *simple source* is connected to an infinite busbar, as shown in Figure 4.1, the voltage $\bar{V}_L$ is a constant phasor. The dynamics are given by the poles of the system, which in this case are easy to determine. For the second-order system shown in (3.78), the characteristic polynomial is

$$\Delta_{\text{src}}(s) = s^2 + \frac{2R}{L}s + \frac{R^2}{L^2} + \omega_o^2 \tag{4.1}$$

whose roots (poles of the system) are simply $\lambda_{1,2} = -\frac{R}{L} \pm j\omega_o$. This pair of complex-conjugate poles are located in the left-hand side of the complex plane, as shown in Figure 4.2. This ensures the stability of this system under any circumstance.

When a *microsource* is connected to an infinite bus, the characteristic polynomial becomes one order higher, and corresponds to the linear system shown in (3.90).

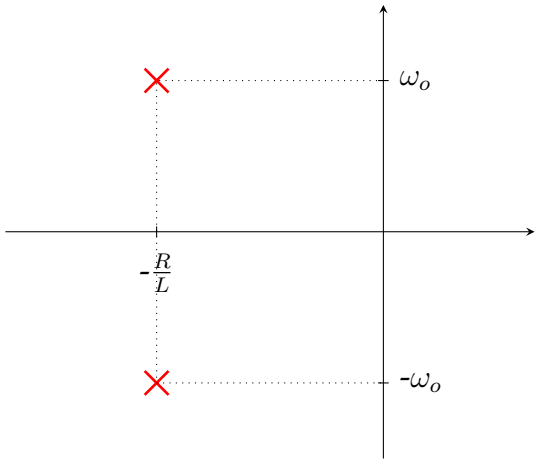

Figure 4.2: Root locus for one simple source, infinite bus system

The characteristic polynomial of this augmented system is

$$\Delta_{\text{usrc}}(s) = s^3 + \underbrace{\frac{2R}{L}}_{B} s^2 + \underbrace{\frac{1}{L^2}\left(Z^2 + \frac{1}{2}LM_pV_e^AV_L^A\sin(\delta)\right)}_{C} s + \underbrace{\frac{1}{2L^2}ZM_pV_e^AV_L^A\sin(\delta+\varphi)}_{D} \tag{4.2}$$

where $Z = \sqrt{R^2+\omega_o^2L^2}$, $\delta = V_L^\Theta - V_e^\Theta$ and $\varphi = \arctan(\frac{\omega_o L}{R})$ are introduced to simplify the notation.

This polynomial will have three roots; since the polynomial coefficients are all real, the roots have to be either all real, or one real and a complex-conjugate pair. One example of a possible root locus is shown in Figure 4.3.

The location of the poles will be a function of the droop gain M_p, as well as the operating point, which appears here as voltage magnitudes V_e^A and V_L^A and phase angle δ. If the operating point is held constant, the increase of the droop gain may have a negative impact on the stability of the system, i.e. for large gains, the system may become unstable.

The stable region, i.e. the range of droop gains with which the system is stable, can be estimated by finding the critical gain $M_p^\star$ at which at least one of the poles

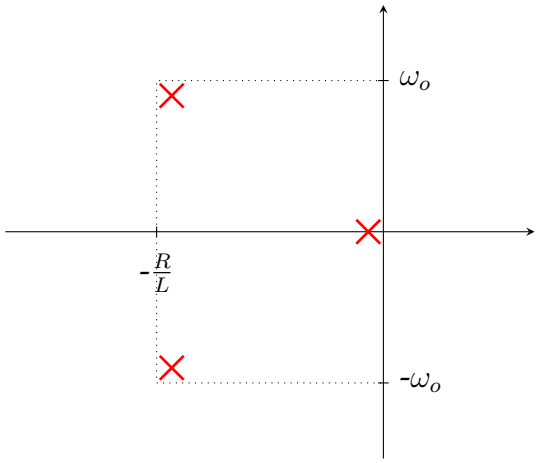

Figure 4.3: Sample root locus for one microsource, infinite bus system

becomes unstable [1]. It could be possible to study the roots of the characteristic polynomial using the discriminant of a cubic polynomial; the complexity, however, renders this approach unmanageable.

Nonetheless, there are a few scenarios of interest, that can be approached with different tools. In particular, we are interested in characterizing the sign of the roots, thus establishing the stability of the system through its eigenvalues. These scenarios are:

- *The three poles are real*. In this case, we can use the Descartes' rule of signs to determine the existence of positive poles. To apply the rule, the polynomial will be rewritten as

$$\Delta_{\text{usrc}}(s) = s^3 + Bs^2 + Cs + D \tag{4.3}$$

  using the definitions of (4.2). The Descartes' rule states that number of sign differences between consecutive non-zero coefficients of this polynomial gives

[1] Only positive droop gains are considered. A similar approach is possible for negative droop gains. This case, however, is out of the scope of this study, as the negative droop gain corresponds to a microsource behavior that contradicts the power sharing objective of a microgrid.

the number of positive roots. As B is always positive, the only coefficients that can tell whether a positive root exists are C and D.

By the observation of those coefficients, one can realize that the sign of D is always determined by the angle $\delta + \varphi$. The angle φ is the series impedance angle, it is always between 0 and $\pi/2$, and is strictly greater that zero when the reactance is not zero. Under the assumption that the angle δ is small, the sign of D is positive, regardless of the droop gain.

The coefficient C, on the other hand, may become negative if

$$Z^2 \leq -\frac{1}{2} L M_p V_e^A V_L^A \sin(\delta) \tag{4.4}$$

which can occur if the droop gain is large enough and $\delta < 0$. If this happens, then there would be two sign differences between consecutive coefficients: C would be negative, and then D would be positive.

The Descartes' rule can only tell, in this case, that there are either two positive real roots, or there are no positive real roots but a complex-conjugate pair (of which we cannot guarantee any property regarding their real part sign). Therefore, the Descartes' rule of sign cannot give enough information in this case, as the system may probably have a complex-conjugate pair (see below for some examples). In general, for small droop gains and small δ, both C and D are positive, and the Descartes' rule can only say that there will not be any *real* positive pole; complex-conjugates with positive real part, however, may still appear.

In addition, the Descartes' rule can be also applied to establish the number of negative real roots. For this purpose, we work with

$$\Delta_{\text{usrc}}(-s) = -s^3 + Bs^2 - Cs + D \tag{4.5}$$

that, under the same assumptions of large droop gain and $\delta < 0$, will only have one sign change. This indicates that the original polynomial $\Delta_{\text{usrc}}(s)$ has

exactly one negative root. In general, for small droop gains and small δ, both C and D are positive, and the polynomial $\Delta_{\text{usrc}}(-s)$ has three consecutive sign changes. This means that the original polynomial has either three negative real roots, or one negative real root and a complex-conjugate pair.

With the results for $\Delta_{\text{usrc}}(s)$ and $\Delta_{\text{usrc}}(-s)$, we can conclude that the polynomial $\Delta_{\text{usrc}}(s)$ has, in general, either one negative root plus a complex-conjugate pair, or three negative real roots. Therefore, in the case where *all poles are real*, they are likely to be all negative.

It is important to note, then, that it is very unlikely that the system will have three real poles, with just one of them being positive.

- *There is one complex-conjugate pole pair, plus a real pole*. In this case, we cannot easily infer any property over the poles. However, there are some properties of polynomial roots that provide some insights about their location on the complex plane.

  The coefficients of a polynomial can be related to its roots by the Vieta's formulas. For our cubic polynomial $\Delta_{\text{usrc}}(s)$, this formulas are

$$-B = \lambda_1 + \lambda_2 + \lambda_3 \tag{4.6}$$

$$C = \lambda_1\lambda_2 + \lambda_1\lambda_3 + \lambda_2\lambda_3 \tag{4.7}$$

$$-D = \lambda_1\lambda_2\lambda_3 \tag{4.8}$$

  The first Vieta's rule (4.6) is providing a key property: the sum of all poles is constant, and it does not depend on the droop gain M_p or the operating point. Hence, the movement of the poles on the complex plane is constrained by (4.6).

  The third Vieta's rule (4.8) is also providing some interesting information: the product of the three poles will grow with D, which in turn grows with M_p. From a magnitude viewpoint, this rule states that the greater M_p is, the greater

the absolute values of the poles will be. In other words, as M_p increases, the poles tend to move away from the origin.

There exist two extreme cases that give some additional insight about the behavior of the poles:

– *If* $M_p = 0$, the characteristic polynomial reduces to

$$\Delta^o_{\text{usrc}}(s) = \left(s^2 + \frac{2R}{L}s + \frac{Z^2}{L^2}\right)s \tag{4.9}$$

in which we have recovered the two complex-conjugate poles of the non-droop-controlled case, plus a pole in the origin. Note how the rule (4.6) holds in this case:

$$-B = -\frac{2R}{L} = \lambda_1 + \lambda_2 + \lambda_3 \tag{4.10}$$

where $\lambda_{1,2} = -\frac{R}{L} \pm j\omega_o$ and $\lambda_3 = 0$. This rule, shown as a constraint on the vector sum of the poles on the complex plane, is presented in Figure 4.4.

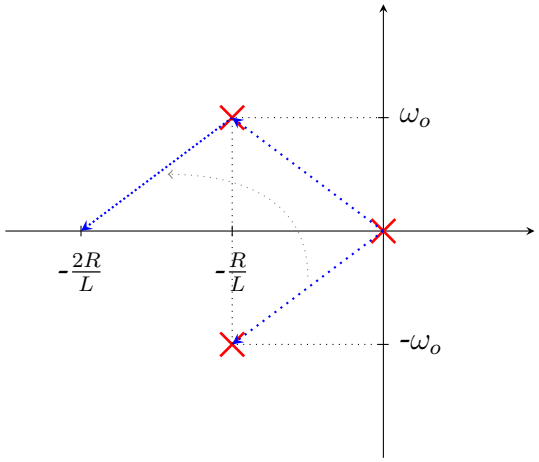

Figure 4.4: Root locus for one microsource, infinite bus system under zero droop gain conditions

– *If the complex-conjugate pair is pure imaginary*, then there is also a pure real pole. The characteristic polynomial in this case will look something like

$$\Delta^{\star}_{\text{usrc}}(s) = (s+\alpha)(s^2+\omega^{\star 2}) \tag{4.11}$$

being the poles $\lambda_1 = -\alpha$ and $\lambda_{2,3} = \pm j\omega^{\star}$. The rule (4.6) will state that, under these circumstances, $\sum_i \lambda_i = -\frac{2R}{L} = -\alpha$, hence

$$\Delta^{\star}_{\text{usrc}}(s) = \left(s + \frac{2R}{L}\right)(s^2+\omega^{\star 2}) = (s+B)(s^2+\omega^{\star 2}) \tag{4.12}$$

Then the root locus would look like Figure 4.5. We call this case the *critical* case, as there are two poles that establish a marginally stable behavior of the system. In this figure, the vectors are drawn to emphasize that Vieta's rule (4.6) also holds.

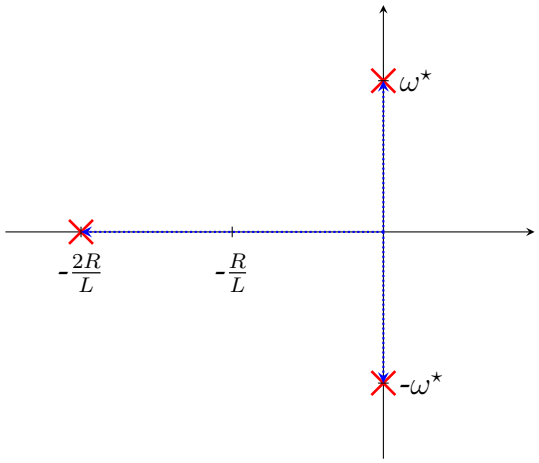

Figure 4.5: Root locus for one microsource, infinite bus system under critical conditions

The critical gain $M_p^{\star}$ and the critical frequency $\omega^{\star}$ can be found if we compare the characteristic polynomials:

$$\begin{aligned} \Delta_{\text{usrc}}(s) &= s^3 + Bs^2 + Cs + D && \text{(general case)} \\ \Delta^{\star}_{\text{usrc}}(s) &= (s+B)(s^2+\omega^{\star 2}) && \text{(critical case)} \end{aligned}$$

If we factor $\Delta_{\text{usrc}}(s)$ by $(s + B)$, then the polynomials could be easily matched. This factorization, obtained using long polynomial division, yields

$$\Delta_{\text{usrc}}(s) = (s + B)(s^2 + C) + \underbrace{(D - CB)}_{R} \tag{4.13}$$

where R is the remainder, which needs to be zero in order for the polynomials $\Delta_{\text{usrc}}(s)$ and $\Delta^{\star}_{\text{usrc}}(s)$ to match.

Setting the reminder to zero yields the following expression for the critical gain:

$$M_p^{\star} = \frac{4Z^2 \frac{R}{L}}{V_e^A V_L^A \left(Z \sin(\delta + \varphi) - 2R \sin(\delta)\right)} \tag{4.14}$$

If the droop gain has this critical value, then the characteristic polynomial has the form of $\Delta^{\star}_{\text{usrc}}$, with $\omega^{\star 2} = C$.

In summary, there are two known cases with complex-conjugate poles: (a) the case where $M_p = 0$ and the two complex-conjugate poles of the non-droop-controlled case appear along with a new pole in the origin, and (b) the case where $M_p = M_p^{\star}$ and the two complex-conjugate poles lie along the imaginary axis. Between these two cases, the poles move continuously with M_p, as it is an established property that the roots of a polynomial are a continuous function of the polynomial's coefficients.

It is important to note that, even though both known cases have a complex-conjugate pair, there may be some values of M_p for which the poles become all real. As it was shown above, it is possible for the system to have three real negative poles, but it is unlikely that the system will have all three positive real poles or only one positive real pole.

Therefore, it is expected that, for $0 < M_p < M_p^{\star}$ the poles will be either all real and negative, or one negative pole plus a complex-conjugate pair; and for $M_p > M_p^{\star}$ the poles will continue being a complex conjugate pair, plus a

negative real pole. As Vieta's formulas (4.6) through (4.8) must hold for any value of M_p, the real negative pole will move towards the left-hand side of the complex plane as M_p increases, while the complex conjugate pair will move towards the right-hand side of the complex plane.

Sketches of possible root loci for the system when varying M_p from 0 to $M_p^\star$ are shown in Figure 4.6.

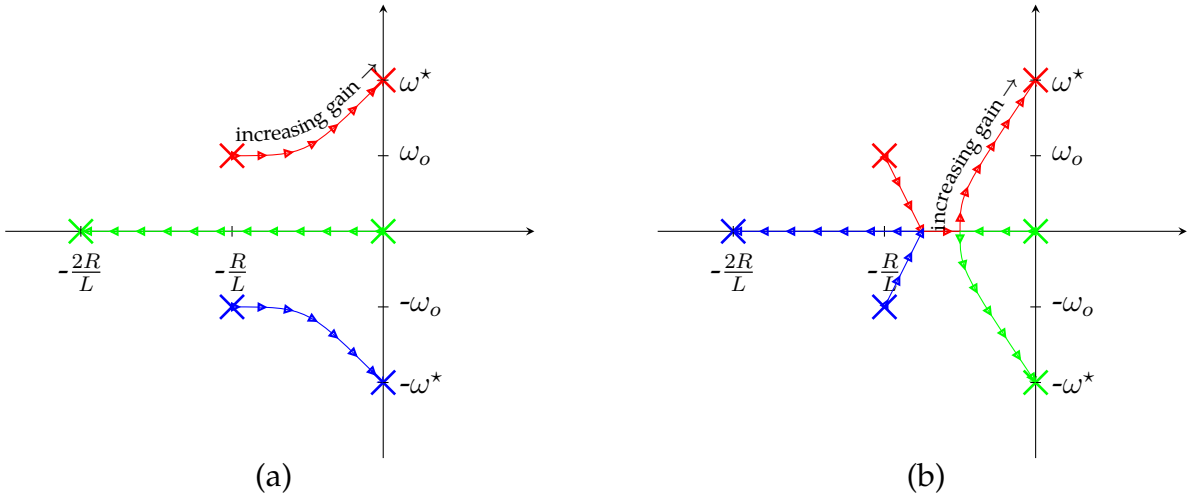

Figure 4.6: Sketch of possible root loci for one microsource, infinite busbar system. (a) shows a case where there are always complex-conjugate poles, while (b) shows a case where the three poles become real for some values of M_p.

The expression (4.14) for $M_p^\star$ can be used to find the critical frequency $\omega^\star$ at which the system becomes unstable:

$$\begin{aligned}\omega^{\star 2} = C|_{M_p^\star} &= \frac{1}{L^2}\left(Z^2 + \frac{1}{2}LM_p^\star V_e^A V_L^A \sin(\delta)\right) \\ &= \frac{Z^2}{L^2}\left[\frac{Z\sin(\delta+\varphi) - R\sin(\delta)}{Z\sin(\delta+\varphi) - 2R\sin(\delta)}\right]\end{aligned} \tag{4.15}$$

If the angle $\delta \approx 0$, then the expressions for $M_p^\star$ and $\omega^\star$ could be simplified:

$$\text{If } \delta \approx 0, \qquad M_p^\star = \frac{4Z^2R}{V_e^A V_L^A \omega_o L^2} \qquad C|_{M_p^\star} = \frac{Z^2}{L^2} \quad \Rightarrow \quad \omega^\star = \frac{Z}{L} \tag{4.16}$$

Moreover, if the impedance is mainly inductive, i.e. $\omega_o L \gg R$, the expressions could be further simplified:

$$\text{If } \omega_o L \gg R, \qquad M_p^\star = \frac{2\omega_o R}{V_e^A V_L^A/2} \qquad C|_{M_p^\star} = \omega_o^2 \quad \Rightarrow \quad \omega^\star = \omega_o \tag{4.17}$$

Expressions (4.17) are equivalent to those in [51], in which a relationship between M_p and R is also found. However, expressions (4.14) and (4.15) are general, i.e. they are valid under any operating condition and are not subject to any simplification of operating points or parameter values.

4.1.2 Numerical solutions

Numerical results are shown in Figure 4.7, where the base parameters of Table 3.1 are being used, with droop gains varying from 0.01% to 4%. The value of $M_p^\star$, using the base parameters, is 2.7413%, which matches with the droop gain at which the poles cross to the right hand side of the complex plane in Figure 4.7. The root locus in this case resembles the sketch of Figure 4.6(a), since the poles never become all real at the same time.

A root locus similar to the sketch of Figure 4.6(b) can also be obtained. The series inductance L was changed from $0.62\,\text{mH}$ to $0.01\,\text{mH}$ and series resistance from $0.0188\,\Omega$ to $0.01\,\Omega$ to produce Figure 4.8. Notice how in this case the poles become all real for some values of M_p. The critical droop gain $M_p^\star$ in this case has a value of 8.3245%, which is not reached with the droop gain ranges of Figure 4.8.

The practical realization of the model is done in Matlab, using the Control System Toolbox. Using the function `ss`, the state space realization (incremental phasor model) of the microgrid model is obtained. The function `pzmap` is used to obtain the pole-zero map, and functions `bode` and `nyquist` are used to obtain the Bode and Nyquist plots respectively.

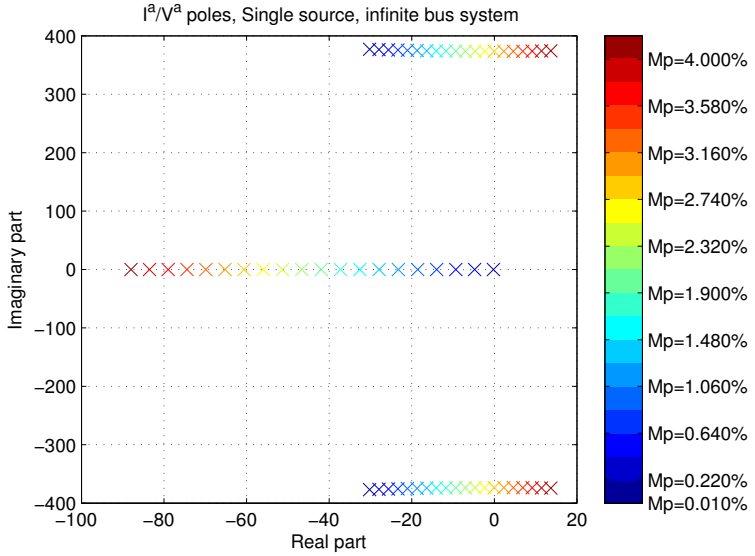

Figure 4.7: Root locus for one microsource, infinite bus system (base parameters)

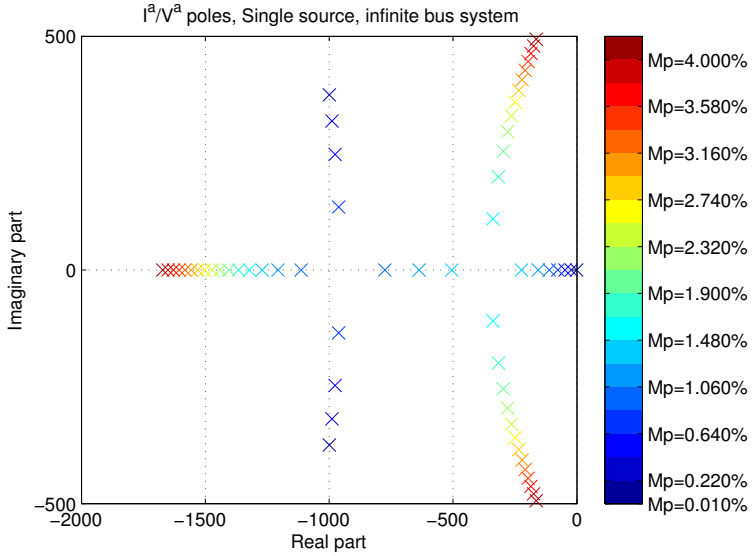

Figure 4.8: Root locus for one microsource, infinite bus system (modified impedance)

4.1.3 Time-domain simulations

Using the base parameters of Table 3.1, a time-domain simulation was carried out. The Simulink block diagram is shown in Figure 4.9.

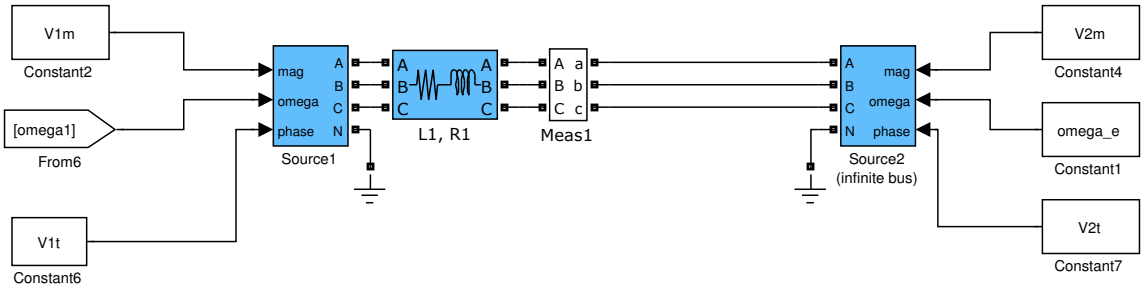

Figure 4.9: One microsource, infinite bus block diagram

Three phase power, voltage and current waveforms of the simulation results are shown in Figure 4.10. During the time-domain simulation, the droop gain was increased from 1.0% to 4.0%, and the system quickly became unstable: immediately after the gain step, the power oscillations begin, and the current slowly starts to diverge. Notice, however, how the voltage remains steady and sinusoidal. This is due to the ideality of the infinite bus, which is not perturbed by any current injection.

The power oscillations are of approximately $59.5\,\text{Hz} = 374.8\,\text{rad}\,\text{s}^{-1}$, which matches the angular frequency (imaginary part) of the unstable poles at that gain ($374.2\,\text{rad}\,\text{s}^{-1}$ in Figure 4.7).

4.1.4 Effects of power measurement filter

If we include the power measurement filter on the microsource model, and going back to using the base parameters, the root locus looks like the one shown in Figure 4.11. The power filter, which has a cut-off frequency of $30\,\text{Hz}$, adds an extra pole, which interacts with the pole that travels to the left on the real axis. Note, however, that the droop gain at which the system becomes unstable is not $M_p^\star$ anymore. In

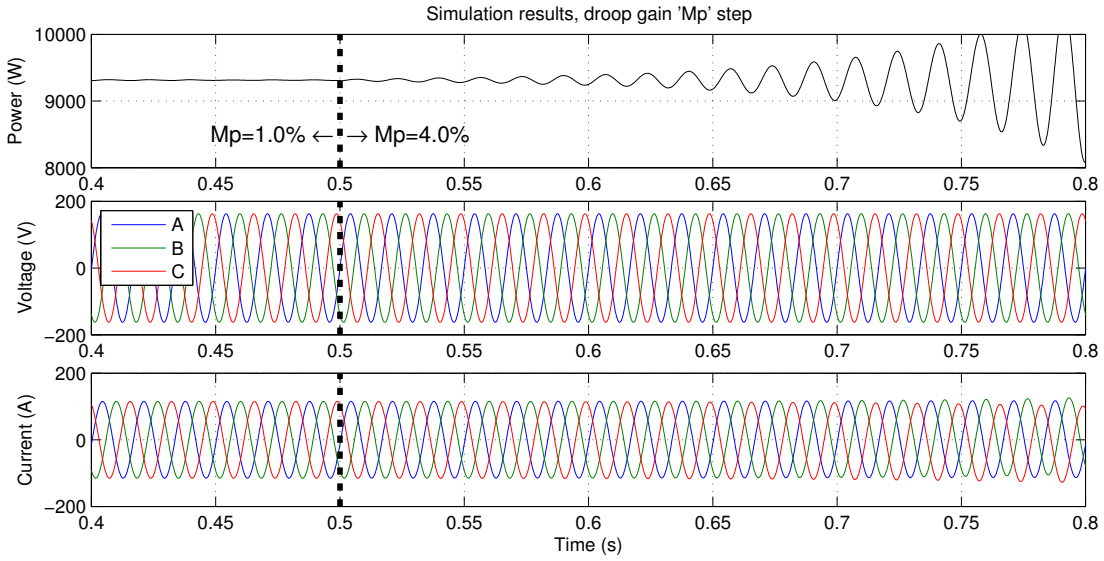

Figure 4.10: Simulation results for one microsource, infinite bus system. At time $t = 0.5\,\mathrm{s}$, the droop gain M_p is increased from 1.0% to 4.0%, entering the unstable region.

fact, the system is always stable under these conditions, and may probably require a much higher droop gain to become unstable.

The effect of the power measurement filter is more radical when the cut-off frequency is reduced. In Figure 4.12 the numerical results are shown when a cut-off frequency of $5\,\mathrm{Hz}$ is used. The root locus shows how the far left complex conjugate poles (that could be attributed to the series impedance, as in Figure 4.2) move towards the left of the complex plane instead of the right, while the real poles (that could be attributed to the filter and the droop controller) interact and become a pair of complex conjugate poles for certain gains. Even though the system is still stable for the whole droop gain range, the instability would probably be driven by these new complex conjugate pair of poles.

A time-domain simulation of the filtered power measurement case was carried out under the same conditions of Section 4.1.3, and its results are shown in Figure 4.13. It can be clearly seen that, in this case, the system does not become unstable after the droop gain step.

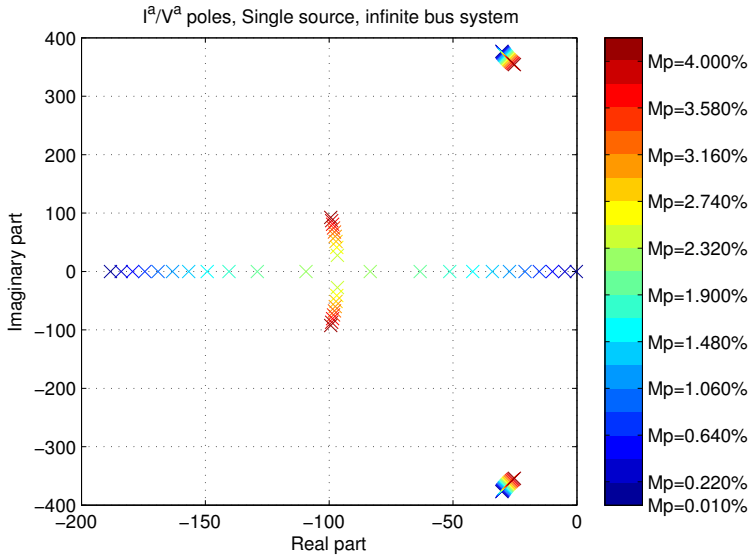

Figure 4.11: Root locus for one microsource, infinite bus system (including power measurement filter)

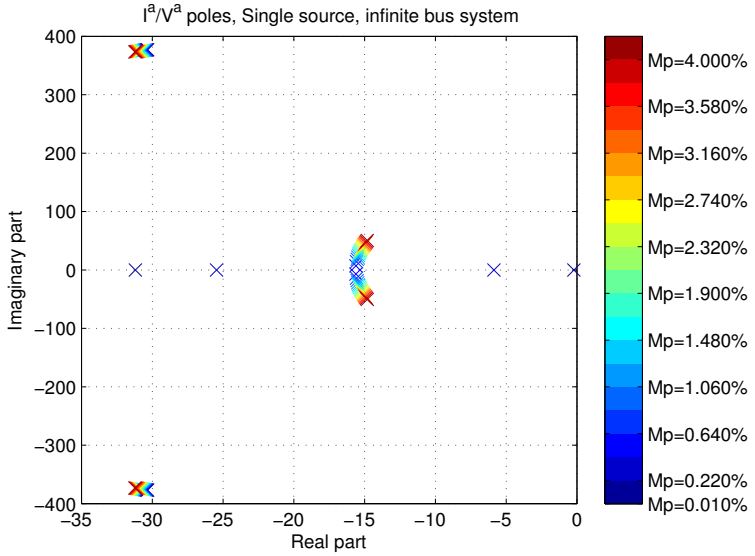

Figure 4.12: Root locus for one microsource, infinite bus system (filter with low cut-off frequency)

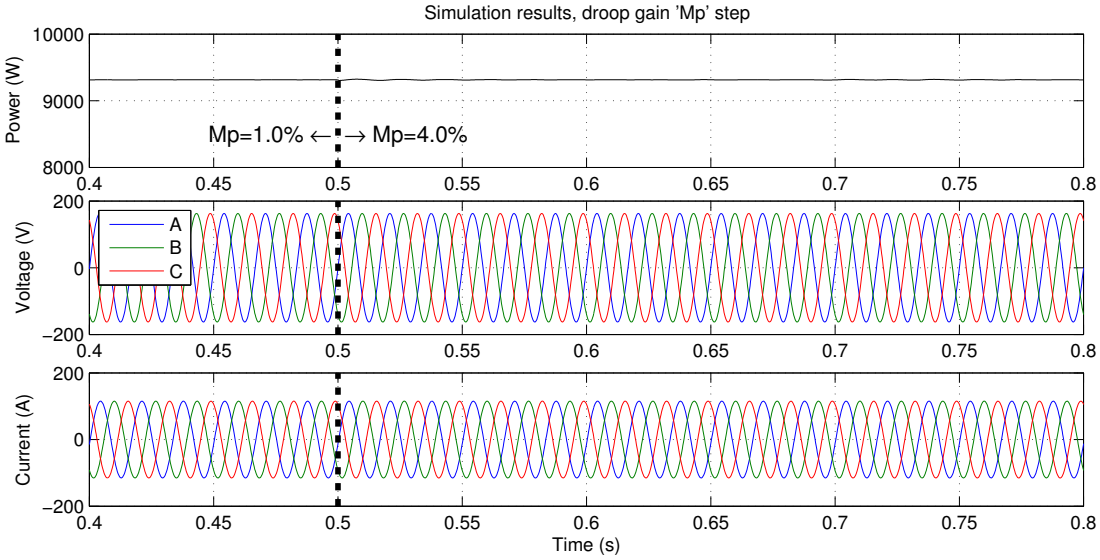

Figure 4.13: Simulation results for one microsource, infinite bus system with power filter. (Under the same conditions of Figure 4.10

4.2 Single microsource, resistive load

In this section, the impedance matching criteria is used to establish the stability of a microgrid comprising a single microsource connected to a resistive load. The behavior of the single microsource, presented in the previous section, is already known when grid-tied. However, in the case of the single microsource feeding a load, the stiffness of the infinite bus is not present.

The single microsource, resistive load system is depicted in Figure 4.14. To study this system, the models of the microsource (Equation (3.90)) and the resistive load (Equation (3.41)) will be used. Note that those models (in this case, the microsource model) is linearized around an operating point. Such operating point $(\bar{V}_L, \bar{I}_L)$ is shared by the microsource and the load. Therefore, it needs to be found *a priori*.

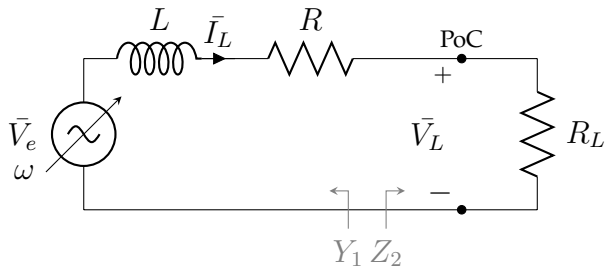

Figure 4.14: One microsource, resistive load system

The operating point is easy to find in this case using phasor algebra and the voltage divider equation:

$$\begin{aligned} \bar{V}_L &= \bar{V}_e \cdot \frac{R_L}{R_L + R + j\omega_o L} \\ \bar{I}_L &= \frac{\bar{V}_L}{R_L} \end{aligned} \tag{4.18}$$

Then, the models of (3.90) and (3.41) can be "plugged" together, i.e. the output current of the microsource is the input current of the load, and the output voltage of the load is the input current of the microsource. Moreover, the incremental phasor impedances Z_2 (Equation (3.105)) and Y_1 (Equation (3.112)) can also be

calculated to be used later in the impedance matching criteria. The incremental phasor impedances interact in a closed-loop fashion, as it was shown in Figure 3.3.

When using the full *incremental phasor model*, an eigenvalue analysis can be carried out on the state matrix. When using the *incremental phasor impedances*, the loop gain $-Y_1 Z_2$ is used to establish the stability properties of the closed-loop system that appears when the models are "plugged" together. These two approaches are compared in the following section.

4.2.1 Numerical results

As shown in Figure 4.14, everything from the PoC to the left is considered the incremental phasor admittance Y_1, while the load at the right of the PoC is the incremental phasor impedance Z_2.

Plots for these impedances are shown in Figure 4.15 using the base parameters of Table 3.1, and varying the droop gain M_p from 0.05% to 5%. In this figure, the incremental phasor impedance Z_2 is constant with a magnitude of 20 dB (equivalent to $R_L = 10\,\Omega$), while the incremental phasor admittance Y_1 is a complex function of frequency.

In this simple case, the overall system eigenvalues are obtained and shown in Figure 4.16 It can be seen that the system has, under these circumstances, eigenvalues only on the left hand side of the complex plane, ensuring stability for all values of droop gain M_p.

On the other hand, the impedance matching criteria looks to the open-loop poles, this is, the poles of the loop gain $-Y_1 Z_2$. Those poles, along with the resulting loop gain bode plots and Nyquist plots are shown in Figure 4.17 for selected values of droop gain M_p. As soon as the open-loop poles cross to the right hand side of the complex plane, the Nyquist plot encirclements of the critical point go from none to two. This ensures the stability of the system for all values of droop gain M_p. A zoom over the critical point is shown in Figure 4.18.

These numerical results show how the stability properties of the system are, in this case, the same whether using the eigenvalue analysis or the impedance

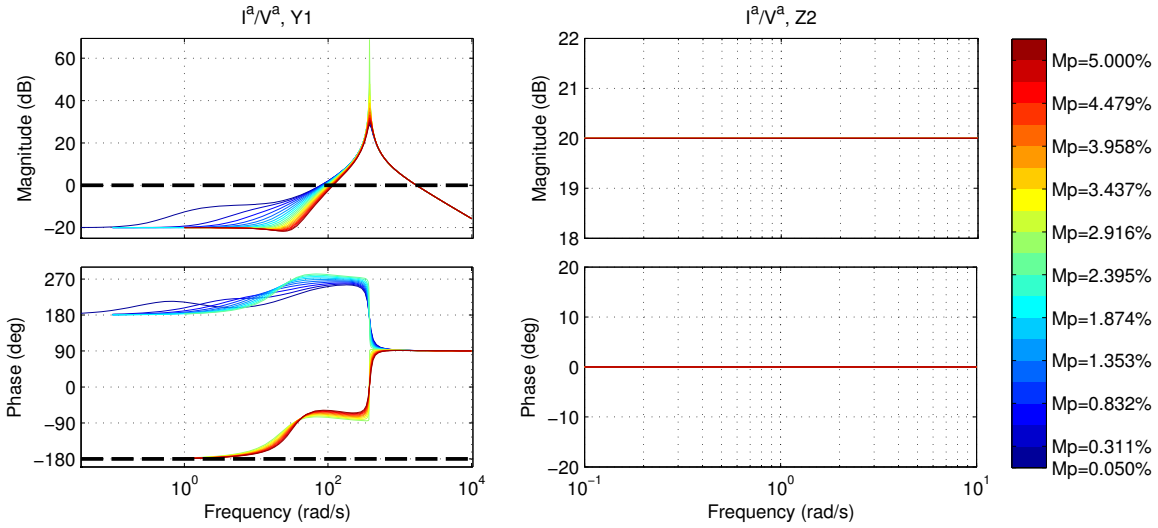

Figure 4.15: Incremental phasor impedance (right) and admittance (left) bode plots for one microsource, resistive load system

matching criteria.

Several other operating points and load resistor values were tested, giving in all cases a stable system, confirmed by both eigenvalue analysis and impedance matching criteria.

4.2.2 Time-domain simulations

The single microsource, resistive load system was simulated using the block diagram shown in Figure 4.19. The load Rstep is a resistor that is inserted for a load step change during the simulation.

The results of the simulation are shown in Figure 4.20, where a droop gain step and a load step are performed. The droop gain is increased from 0.1% to 1.0%, and the load is increased from 0.16pu to 0.86pu. None of these steps has a detrimental effect on the stable operation of the system, as predicted by the impedance matching criteria.

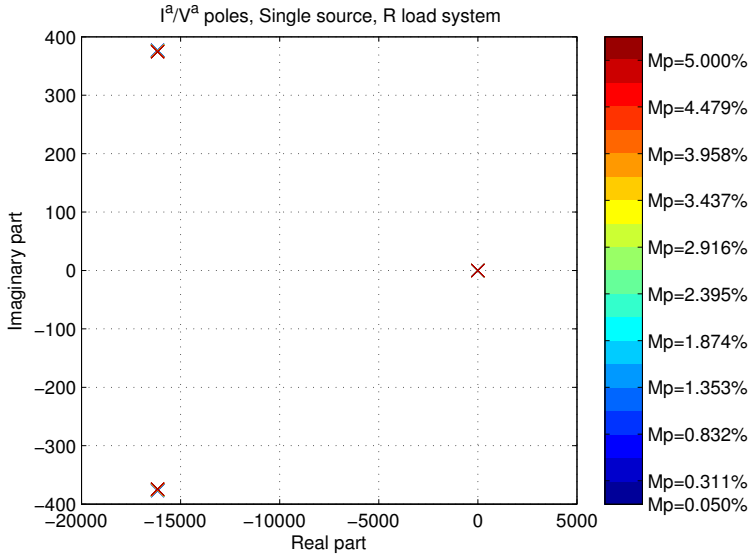

Figure 4.16: Root locus for one microsource, resistive load system

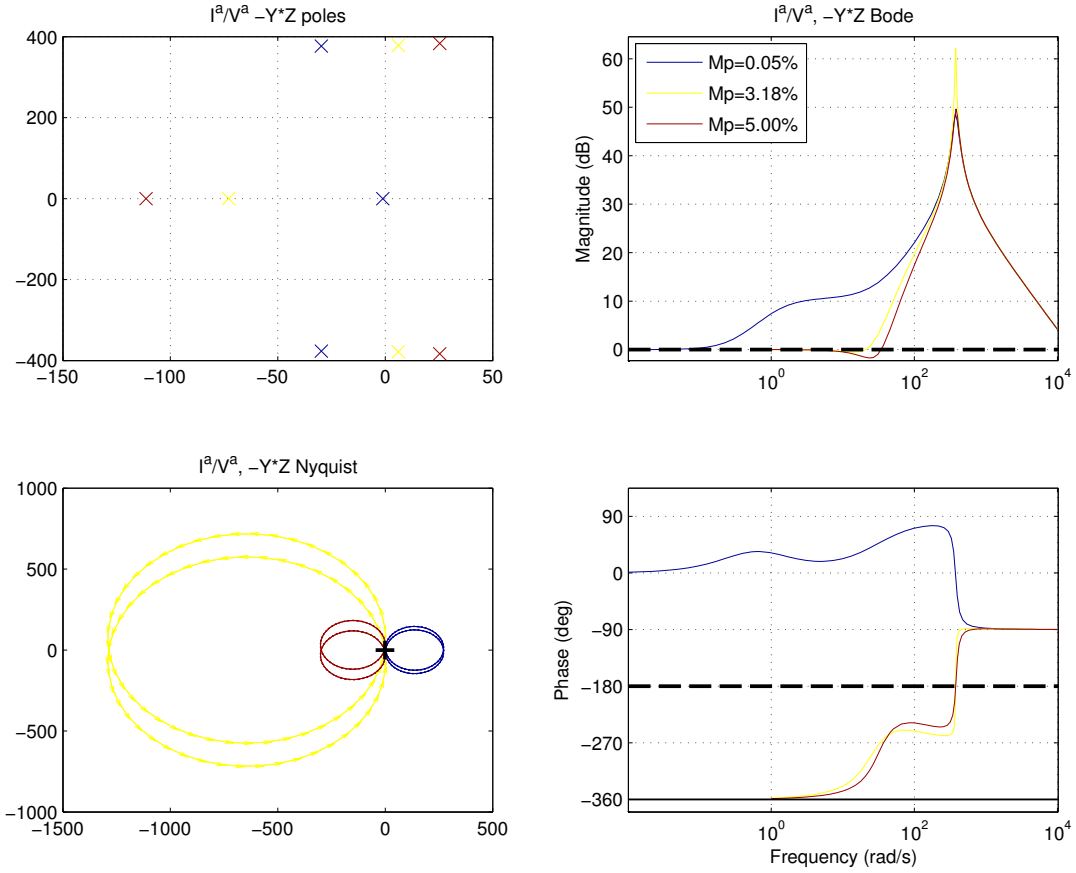

Figure 4.17: Plots for one microsource, resistive load system.

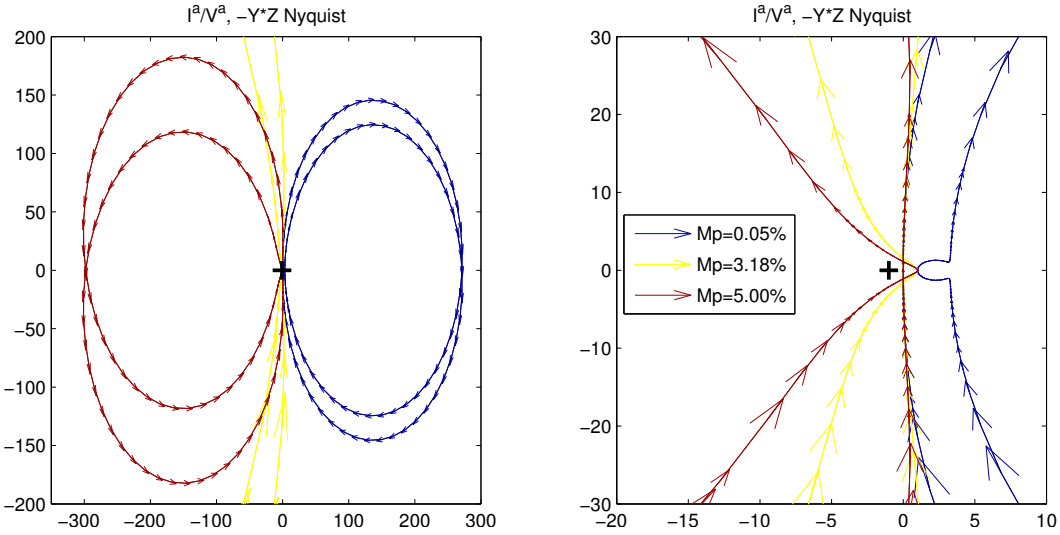

Figure 4.18: Detailed Nyquist plot for one microsource, resistive load system. Note how the encirclements go from none to two as the complex conjugate poles cross the imaginary axis.

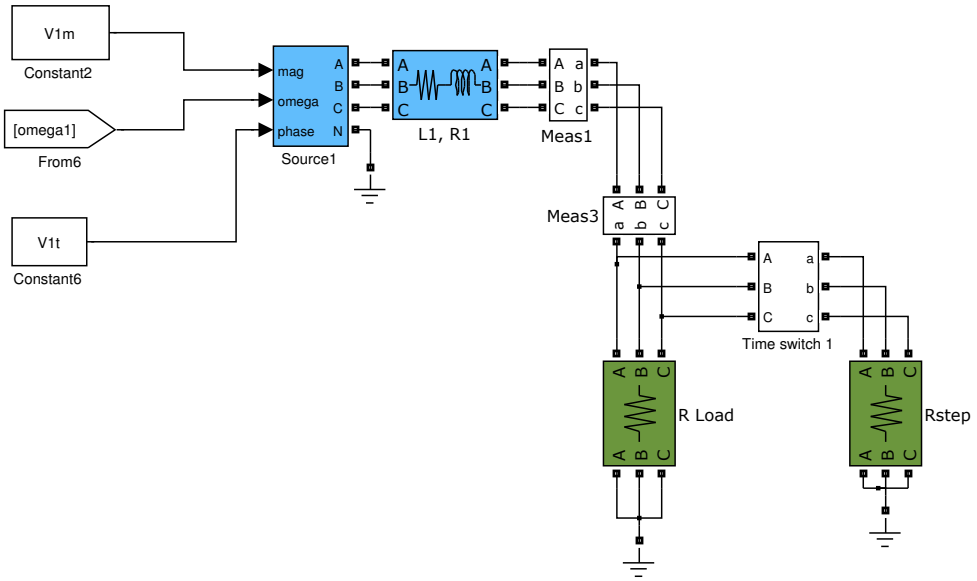

Figure 4.19: One microsource, infinite bus block diagram

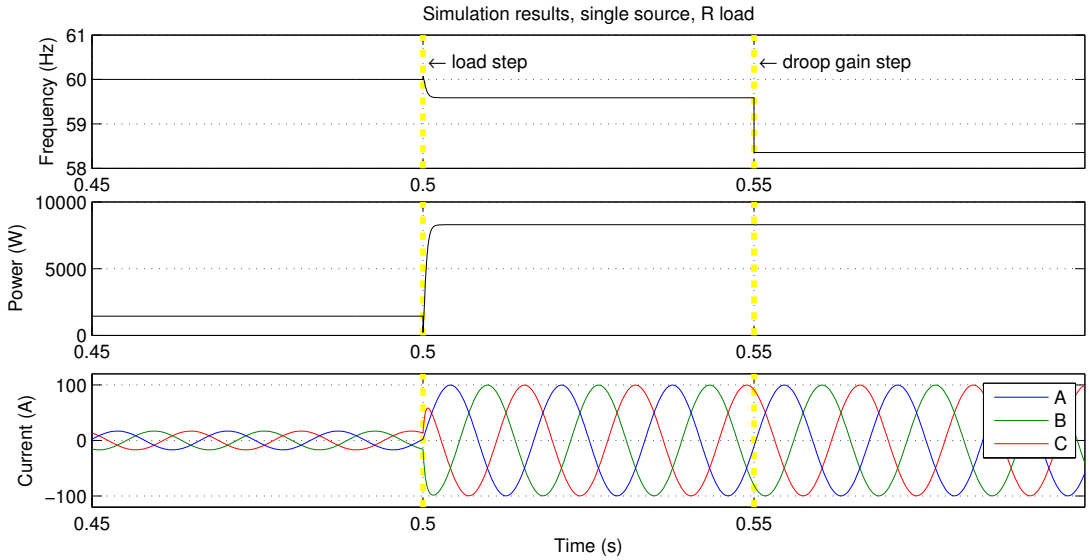

Figure 4.20: Simulation results for one source, resistive load system. At time $t = 0.5\,\mathrm{s}$, the load is stepped from 0.16pu to 0.86pu, and at time $t = 0.55\,\mathrm{s}$ the droop gain M_p is increased from 0.1% to 1.0%

4.3 Single microsource, R-L load

The the single microsource, R-L load microgrid is remarkably similar to the single source, resistive load microgrid. In fact, the time-domain simulation results are practically equal, hence not shown here.

The schematic of this microgrid is shown in Figure 4.21. As in the previous case, the models of the microsource (Equation (3.90)) and the R-L load (Equation (3.54)) will be used.

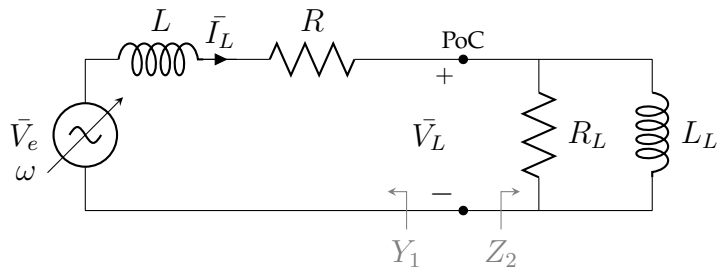

Figure 4.21: One microsource, R-L load system

The operating point is also calculated with phasor algebra, with a result similar to (4.18), but replacing R_L with the parallel combination of R_L and L_L.

The eigenvalues of the overall system are presented in Figure 4.22. It can be seen that a pair of new poles appear when comparing this root locus to Figure 4.16. These new poles could be atributed to the inductor L_L.

The incremental phasor impedances are shown in Figure 4.23 using the base parameters of Table 3.1, and varying the droop gain M_p from 0.05% to 5%. The incremental phasor impedance Z_2 now has a magnitude of $20\,\text{dB}$ (equivalent to the resistive component $R_L = 10\,\Omega$) and a resonance peak around the system's frequency $\omega_o = 377\,\text{rad}\,\text{s}^{-1}$. The incremental phasor admittance Y_1 remains a complex function of frequency, similar to the one in Figure 4.15.

The open loop poles, along with the resulting loop gain Bode plots and Nyquist plots are shown in Figure 4.24 for selected values of droop gain M_p. A similar behavior is observed, in which the encirclements of the critical point go from zero

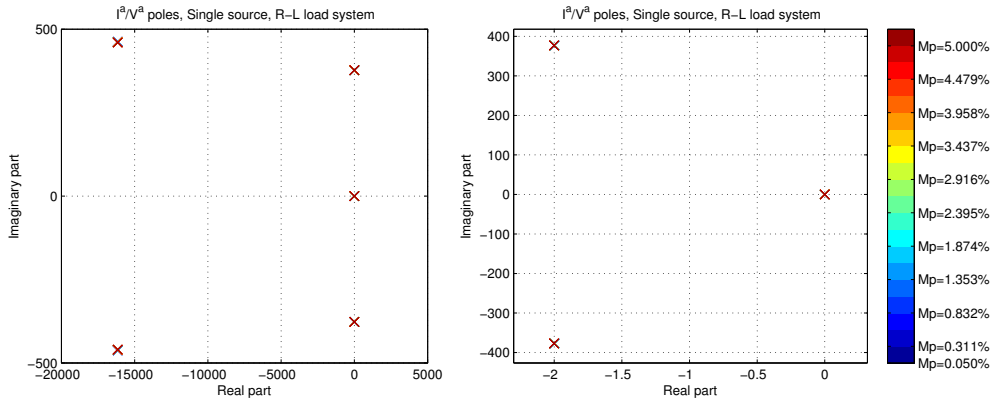

Figure 4.22: Root locus for one microsource, R-L load system. (A zoom around the imaginary axis is provided on the right plot)

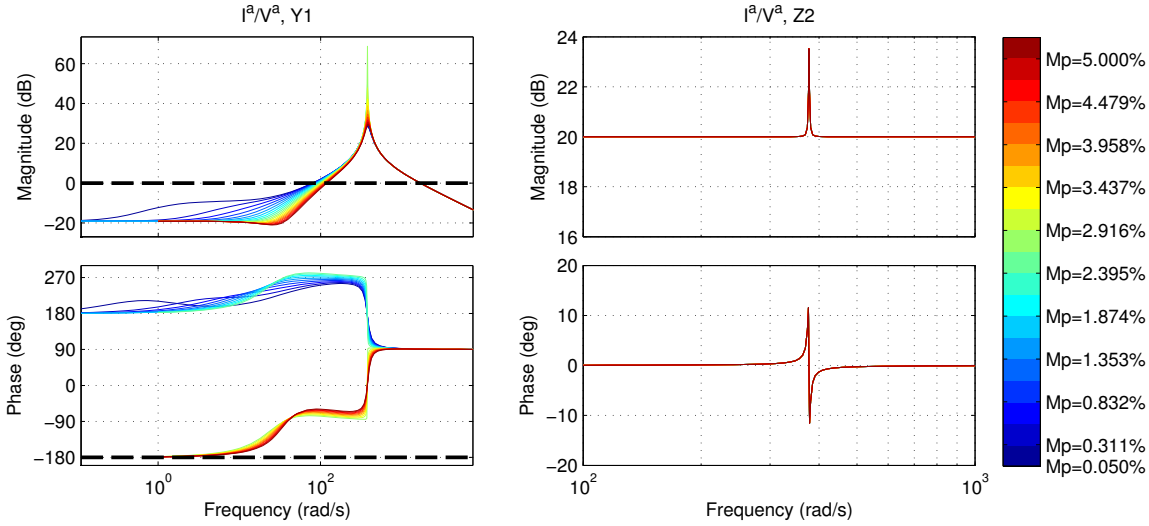

Figure 4.23: Incremental phasor impedance (right) and admittance (left) bode plots for one microsource, R-L load system

to two as soon as a pair of poles travel to the right hand side of the complex plane. A zoom over the critical point is shown in Figure 4.25.

The dynamics introduced by the inductor do not impact in the stability properties of the system in the presented example. These dynamics appear as extra loops in the Nyquist diagrams of Figure 4.24. Those loops are in fact far from the

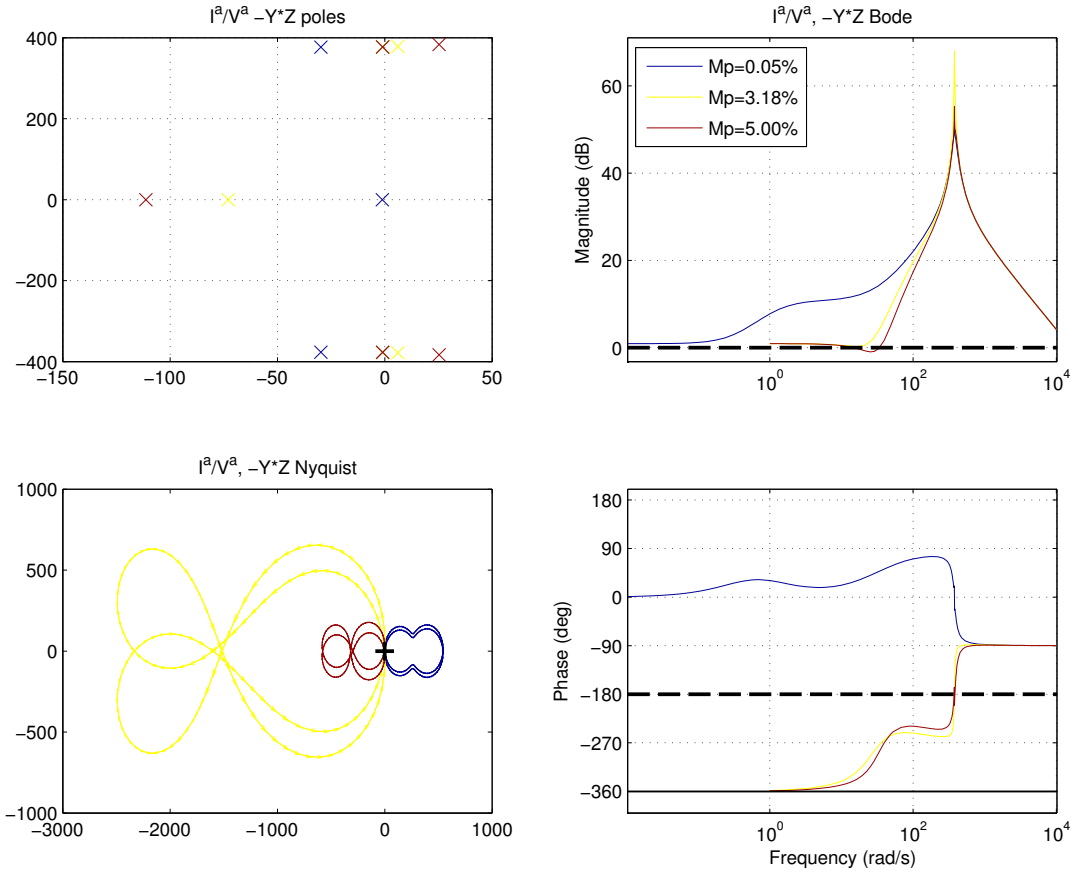

Figure 4.24: Plots for one microsource, R-L load system

critical point. However, it is important to note that, even the slight difference in a incremental phasor impedance, such as the differences shown between R and R-L loads of Figures 4.15 and 4.23, may have a noticeable impact on the Nyquist plot and, hence, the stability properties of the system.

4.4 Summary

In this chapter, single source microgrids were studied from the analytical, numerical and simulation point of view.

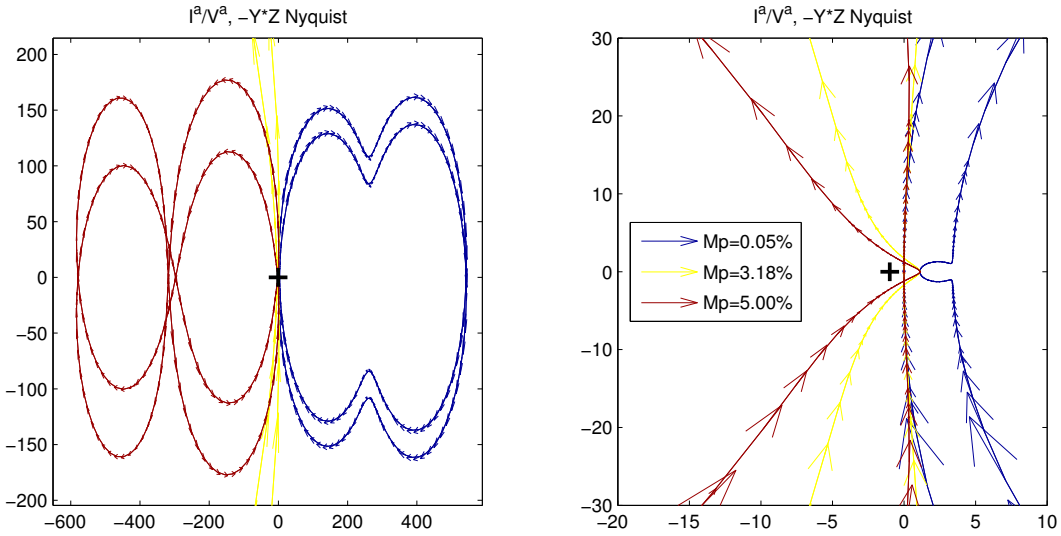

Figure 4.25: Detailed Nyquist plot for one microsource, R-L load system. Compare this to Figure 4.18.

The case of a single microsource coupled to an infinite bus is one of the most popular ones in literature. The microsource model of Section 3.4, which uses dynamic phasors, was thoroughly studied. The analytical results agree with the results found in literature. For example, the eigenvalues of a microsource and the characteristic polynomials found in [36] are the same as the ones of the incremental phasor model, presented in Section 4.1.1. An stability region was also found, along with an analytical expression for the critical droop gain M_p^*, which is equivalent to the results of [51].

The case of a single microsource coupled to a load was used to validate the dynamic phasor and incremental phasor models. The numerical results predicted, in the cases shown in Section 4.2 and 4.3, that the system would be stable under several operating conditions. In fact, the time-domain simulations showed that, when the droop gain and the load was changed, the system maintained its stable operation. This is a particularly important result, because it ensures that the microsource, operating in islanded mode, will have no problems feeding a resistive or R-L load, which is one of the typical loads found in a microgrid.

5 TWO SOURCE MICROGRID

In this chapter, the microgrid model will be extended to include a second microsource and a load. The goal of this larger model is to study the dynamics of multiple source interaction, and the stability analysis through the impedance matching criteria.

The two microsource microgrid is presented in Figure 5.1, where a generic load is shown at the point of connection.

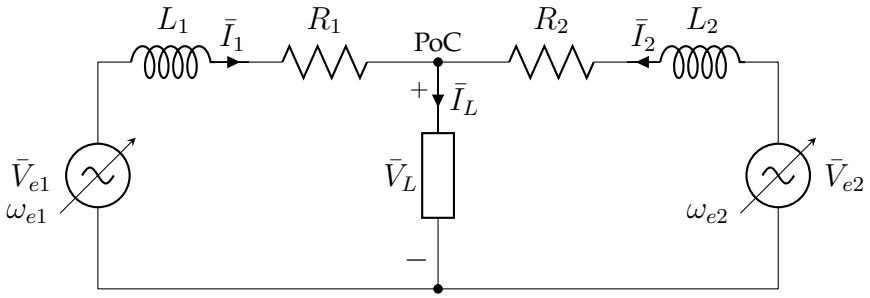

Figure 5.1: Two-microsource microgrid schematic

In this microgrid, several cases might be represented depending on the configuration of each element. For example, if the droop gain of the microsource 2 is very small, it could represent a larger grid (which will be stiff at the power levels of a smaller microgrid, an *infinite bus* [27, Ch. 7]), with the impedance elements R_2 and L_2 representing the grid connection impedance, which in turn determines the short circuit level at the PoC. Another example is the use of the microsource 2 as an equivalent of a larger portion of a microgrid.

5.1 Impedance matching on the two-microsource microgrid

The two-microsource microgrid can be represented by the block diagram of Figure 5.2, where the current outputs of each microsource are added onto the load cur-

rent $\bar{I}_L$. If we split this system in two parts, as shown in Figure 5.3(a), the block diagram can be redrawn as in Figure 5.3(b), where the admittance Y_1 represents the microsource 1, and the impedance Z_2 represents the rest of the system (local load and microsource 2). In this configuration, the stability of the system can be analyzed using an impedance matching criteria, since it resembles the structure of Figure 3.3(a).

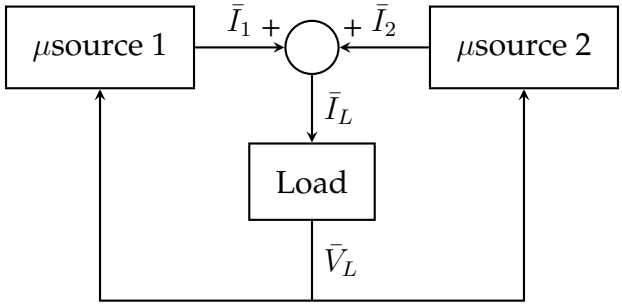

Figure 5.2: Block diagram of the two-microsource microgrid

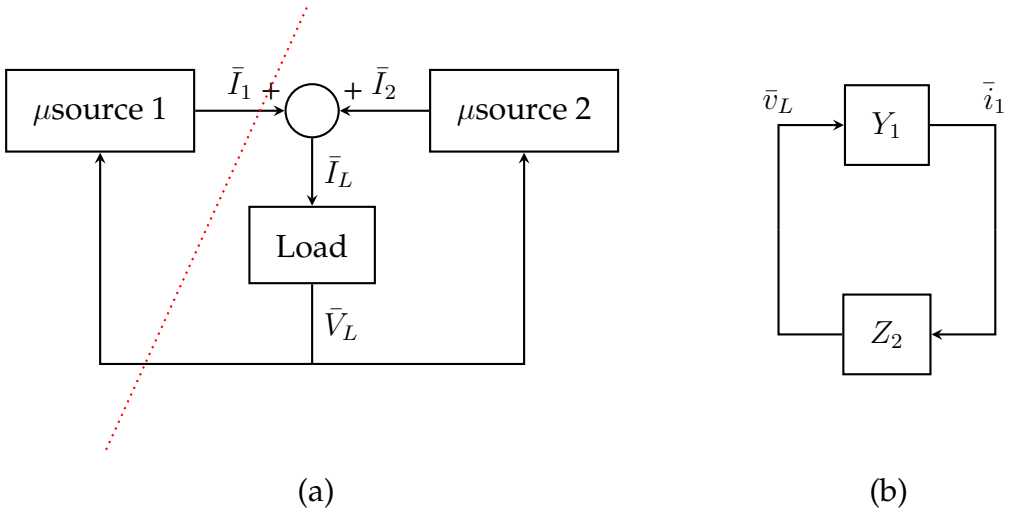

Figure 5.3: Impedance-admittance block diagram of the two-microsource microgrid. On (a), everything at the right of the dotted line becomes the impedance Z_2, while the microsource 1 is represented as an admittance Y_1.

5.2 Operating point

The operating point is easy to find when the local load is a passive linear component that can be represented by an impedance Z_L. In this case, the operating point for this two-microsource microgrid can be determined using, for example, mesh analysis.

5.2.1 Linear load

It is assumed that the frequency of the system is the rated frequency (i.e. $60\,\text{Hz}$) and the droop controllers are set such that the frequency of each unit matches the frequency of the system at whatever power levels result from the operating point to be found. In other words, the power setpoints on each source are equal to the power levels that result from the operating point calculation.

Mesh currents i_a and i_b are defined (and indicated on gray) in Figure 5.4.

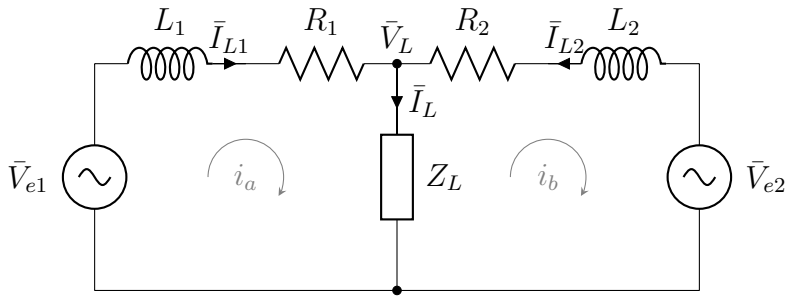

Figure 5.4: Two-source microgrid schematic for operating point calculation

The Kirchoff Voltage Law (KVL) applied on each loop results in the linear system of equations

$$0 = -\bar{V}_{e1} + Z_1 i_a + Z_L(i_a - i_b) \tag{5.1}$$

$$0 = Z_L(i_b - i_a) + Z_2 i_b + \bar{V}_{e2} \tag{5.2}$$

where $Z_1 = R_1 + jL_1$ and $Z_2 = R_2 + jL_2$. The system can be rewritten in the matrix

form

$$\underbrace{\begin{pmatrix} Z_L + Z_1 & -Z_L \\ -Z_L & Z_L + Z_2 \end{pmatrix}}_{A} \underbrace{\begin{pmatrix} i_a \\ i_b \end{pmatrix}}_{\vec{i}} = \underbrace{\begin{pmatrix} \bar{V}_{e1} \\ -\bar{V}_{e2} \end{pmatrix}}_{\vec{v}} \tag{5.3}$$

The solution to this system will simply be $\vec{i} = A^{-1} \cdot \vec{v}$, which gives us the following solutions:

$$\bar{I}_1 = i_a = \frac{Z_L + Z_2}{Z_L(Z_1 + Z_2) + Z_1 Z_2} \bar{V}_{e1} - \frac{Z_L}{Z_L(Z_1 + Z_2) + Z_1 Z_2} \bar{V}_{e2} \tag{5.4}$$

$$\bar{I}_2 = -i_b = \frac{Z_L + Z_1}{Z_L(Z_1 + Z_2) + Z_1 Z_2} \bar{V}_{e2} - \frac{Z_L}{Z_L(Z_1 + Z_2) + Z_1 Z_2} \bar{V}_{e1} \tag{5.5}$$

The voltage on the load is easily found by either of these two expressions:

$$\bar{V}_L = \bar{V}_{e1} - Z_1 \bar{I}_1 \qquad \bar{V}_L = \bar{V}_{e2} - Z_2 \bar{I}_2 \tag{5.6}$$

5.2.2 Non-linear loads and others

In the general case, the load cannot be represented by a linear impedance. There exist well known tools that can be applied in that case. For instance, the operating point of an EPS can be obtained by an iterative process, such as a load flow [92, Ch. 5], which is readily applicable to the two source microgrid.

5.3 Current node

Every small signal model was developed with their ports being a single voltage and a single current. When connecting two or more sources together, e.g. to a common coupling point (such as the load point), it is necessary to add a "current node" small signal system, which will compute the total current coming to such node.

For a generic node, such as the one shown in Figure 5.5, the sum of all currents

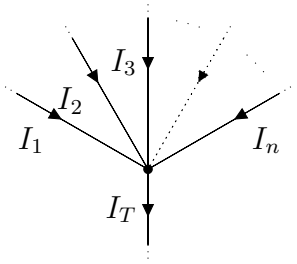

Figure 5.5: Generic current node

is zero. Using the current directions of the figure, this condition is given by

$$I_T = I_1 + I_2 + \ldots + I_n = \sum_{i=1}^{n} I_i \tag{5.7}$$

In terms of dynamic phasors, these relationship becomes

$$I_T^a = \sqrt{\left(\sum_{i=1}^{n} I_i^a \cos(I_i^\theta)\right)^2 + \left(\sum_{i=1}^{n} I_i^a \sin(I_i^\theta)\right)^2} \tag{5.8}$$

$$I_T^\theta = \arctan\left(\frac{\sum_{i=1}^{n} I_i^a \sin(I_i^\theta)}{\sum_{i=1}^{n} I_i^a \cos(I_i^\theta)}\right) \tag{5.9}$$

This non-linear relationship needs to be linearized around the operating point of the whole system. For the current node linearization, all current magnitudes and angles at the operating point are needed.

Since there are no dynamics in the current node equations, the small signal model will be a single gain matrix.

For a given $k \in \{1, \ldots, n\}$,

$$\begin{aligned}
\frac{\mathrm{d}I_T^a}{\mathrm{d}I_k^a} &= \cos(I_T^\Theta - I_k^\Theta) \\
\frac{\mathrm{d}I_T^a}{\mathrm{d}I_k^\theta} &= I_k^A \sin(I_T^\Theta - I_k^\Theta) \\
\frac{\mathrm{d}I_T^\theta}{\mathrm{d}I_k^a} &= -\frac{1}{I_T^A} \sin(I_T^\Theta - I_k^\Theta) \\
\frac{\mathrm{d}I_T^\theta}{\mathrm{d}I_k^\theta} &= \frac{I_k^A}{I_T^A} \cos(I_T^\Theta - I_k^\Theta)
\end{aligned} \tag{5.10}$$

If the current inputs and output are arranged such that

$$\bar{I}_i = \begin{pmatrix} I_i^a \\ I_i^\theta \end{pmatrix} \quad i = 1, \ldots, n \qquad \bar{I}_T = \begin{pmatrix} I_T^a \\ I_T^\theta \end{pmatrix} \tag{5.11}$$

and the same designation applies for the small signal quantities $\tilde{i}_i, \tilde{i}_T$, then

$$\begin{aligned}
\tilde{i}_T &= \sum_{i=1}^{n} D_i \tilde{i}_i \\
D_i &= \begin{pmatrix} \cos(I_T^\Theta - I_k^\Theta) & I_k^A \sin(I_T^\Theta - I_k^\Theta) \\ -\frac{1}{I_T^A} \sin(I_T^\Theta - I_k^\Theta) & \frac{I_k^A}{I_T^A} \cos(I_T^\Theta - I_k^\Theta) \end{pmatrix} \qquad i = 1, \ldots, n
\end{aligned} \tag{5.12}$$

5.4 Two microsources, resistive load

In this section, the impedance matching stability criteria will be applied to the microgrid that comprises two microsources, shown in Figure 5.1, with a resistor in place of the load at the PoC. The procedure to obtain the numerical results is similar to the one used in the previous chapter.

The practical realization of the models is done in Matlab, using the Control System Toolbox. The function `ss` is used to obtain the state space realization of the incremental phasor model of the microgrid components. First, models for the

Microsources 1 and 2 are obtained. Then, the model for the load and the current node are also obtained. The load, current node and Microsource 2 are connected using the toolbox's function `connect`, and the full microgrid system is then obtained closing the loop with the function `feedback`. The functions `pzmap`, `bode` and `nyquist` are used to obtain the Pole-Zero, Bode and Nyquist plots respectively.

5.4.1 Numerical results

The eigenvalues of the full system are shown in Figure 5.6, where the base parameters of Table 3.1 are being used, with droop gain M_{p1} varying from 0.1% to 6%. There is a group of complex-conjugate pairs of poles located far left from the imaginary axis that do not participate in the dynamics that affect the stability of the microgrid. A zoom around the imaginary axis is also provided in the figure: it can be seen that these poles behave like the poles of the single source case, shown in Figure 4.7.

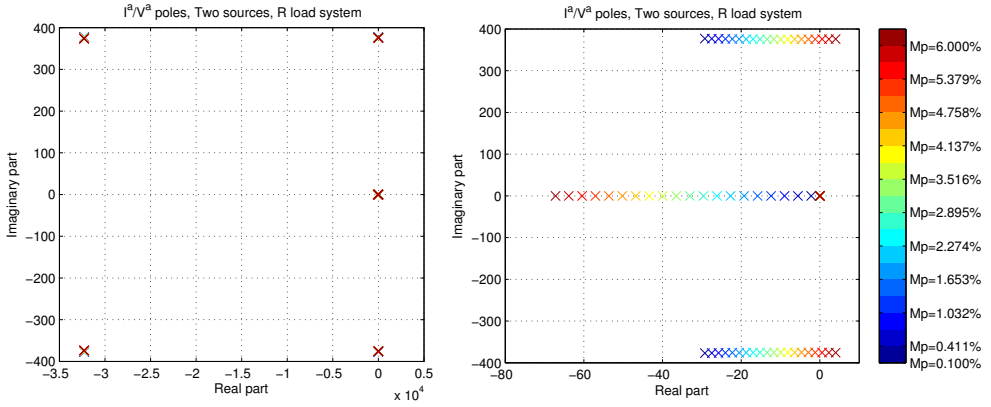

Figure 5.6: Root locus for two microsource system. (A zoom around the imaginary axis is provided on the right plot)

Plots for the incremental phasor admittance Y_1 (Microsource 1) and impedance Z_2 (Microsource 2 and load) are shown in Figure 5.7. In this figure, the incremental phasor impedance Z_2 shows a magnitude of $20\,\mathrm{dB}$ for high frequencies, which corresponds to the resistance of the load $R_L = 10\,\Omega$; for low frequencies, however,

the shape is more complex. The incremental phasor admittance Y_1 remains a complex function of frequency, similar to the one in Figure 4.15.

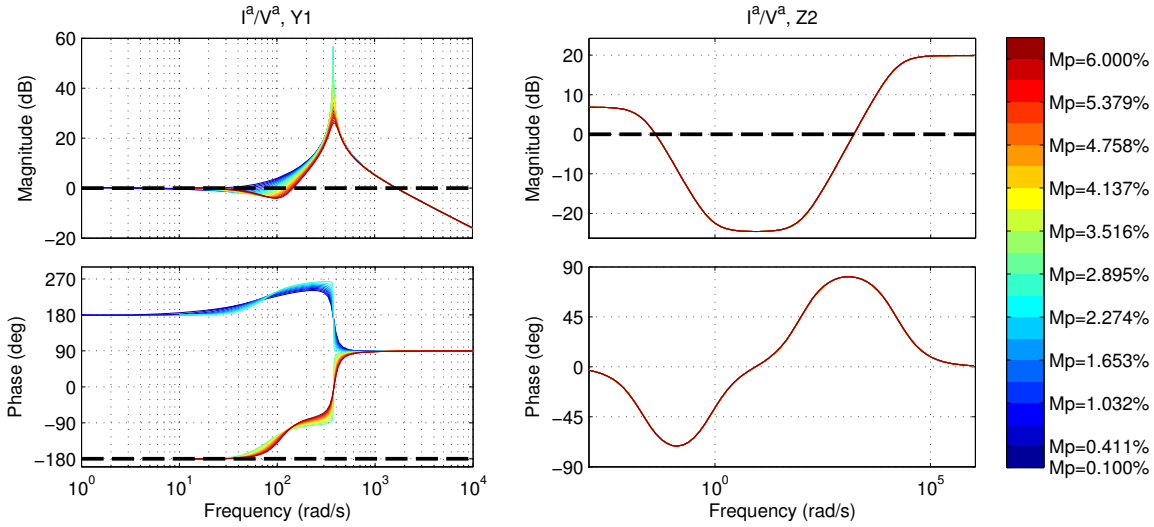

Figure 5.7: Incremental phasor impedance (right) and admittance (left) bode plots for two microsources, resistive load system

The open loop poles, along with the resulting loop gain Bode plots and Nyquist plots are shown in Figure 5.8 for selected values of droop gain M_{p1}. On the one hand, the Nyquist plot shows encirclements of the critical point that go from zero for the lowest gain, to two encirclements for $M_{p1} = 3.83\%$, and back to zero encirclements for $M_{p1} = 6.0\%$. On the other hand, the open-loop poles cross to the right hand side of the complex plane for droop gains above 3.83%, as shown in the zoom in Figure 5.9. This means that the system *does not* become unstable immediately after the open-loop poles become unstable, because the encirclements on the Nyquist plot go from zero to two at the same time. In fact, the system becomes unstable when the gain is high enough that there are two open-loop unstable poles and the encirclements go back to zero, not fulfilling the Nyquist Stability Criterion. In the numerical results, this happens for a droop gain of $M_{p1} \approx 5.3\%$.

Notice how this configuration, with two microsources and a load, allows the droop gain M_{p1} to be larger than the case of a single microsource connected to the

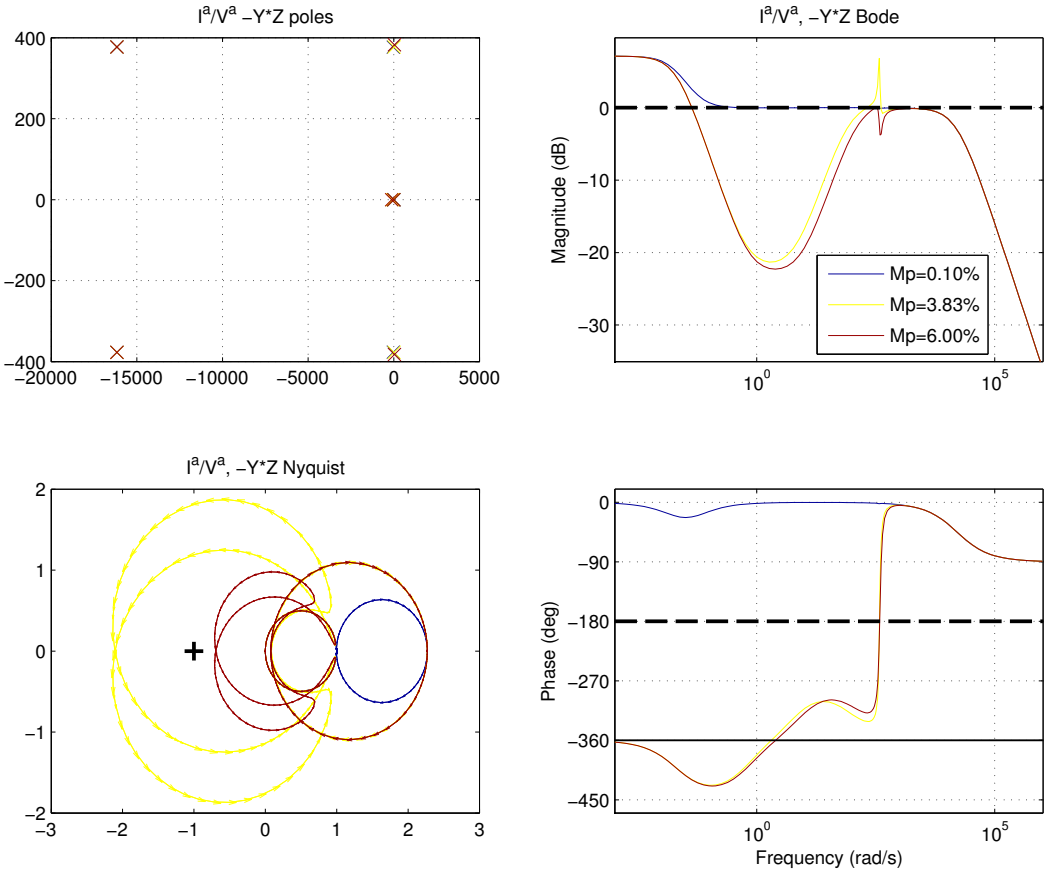

Figure 5.8: Plots for two microsources, resistive load system.

infinite bus (which had a critical droop gain of $M_{p1} = 2.7413\%$).

5.4.2 Time-domain simulations

The two microsources, resistive load microgrid was simulated using the block diagram shown in Figure 3.16. The load Rstep, a resistor that is inserted for a load step change, was nos used in this case. The base parameters of Table 3.1 are used the simulation.

The results of the simulation are shown in Figure 5.10, where the droop gain M_{p1} is increased from 3.0% to 6.0%. As predicted by the impedance matching criteria,

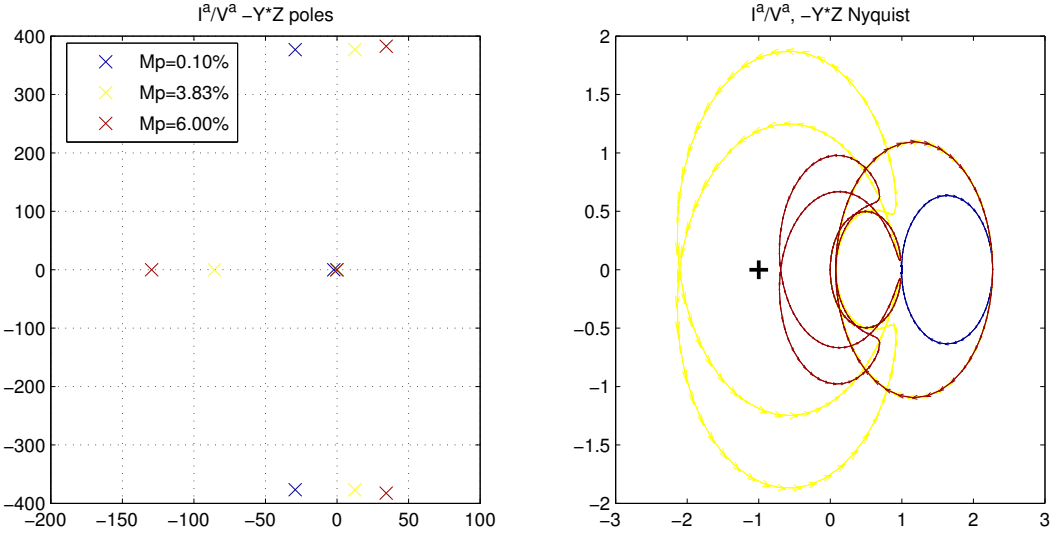

Figure 5.9: Detailed plots for two microsources, resistive load system. Pole locations (left) show how the loop gain goes from having none to two unstable poles. Nyquist plot (right) shows several counter-clockwise encirclements of the critical point (-1,0); however, only the highest gain case is unstable.

the system quickly becomes unstable after the gain step: there are clear active power oscillations that destabilize the system. Notice how the currents become asymmetric and the frequency also presents oscillations of exponentially increasing amplitude.

5.4.3 Frequency-domain simulations

The time-domain simulations are confirming the results of the impedance matching stability criteria. Using the developed models and microgrid parameters, the incremental phasor impedances can be numerically obtained and the stability of the microgrid can be assessed. However, in a practical system, the numerical models of the microgrid components will not be known. This is particularly true for a large microgrid in which a new unit is being connected. The approach in those cases is to experimentally measure the impedance at the PoC.

As an additional validation of the impedance matching criteria, several time-

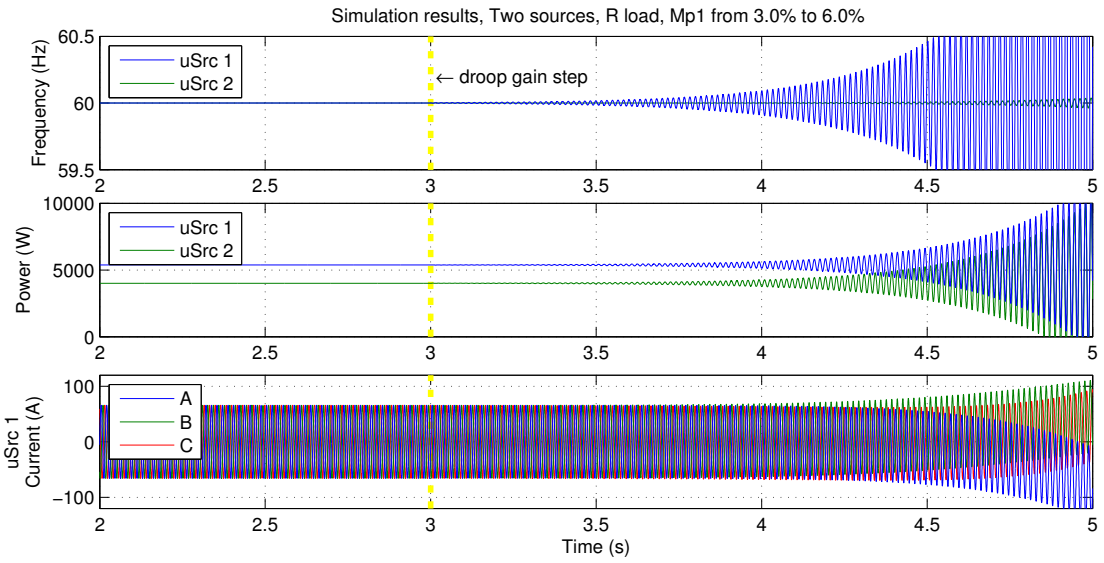

Figure 5.10: Time-domain simulation results for two microsources, resistive load system. At time $t = 3.0\,\mathrm{s}$ the droop gain M_{p1} is increased from 3.0% to 6.0%

domain simulations were carried out, in which small signal currents and voltages were injected into the system, at the PoC, and the small signal response of the currents and voltages of the microgrid components were recorded and post-processed. The idea behind this small signal injection is to recover the incremental phasor impedances and admittances shown in Figure 5.7. This approach resembles several of the methods presented in Section 2.4.1.

The small signal injection is performed at the block diagram level, as shown in Figure 5.11. The Current injection block is generating a small current of programmable frequency, and the Small signal impedance measurement block is processing the measured voltages and currents through Fourier component decomposition. The Fourier components that corresponds to the injected small signals (identified by the frequency signal wt+phi in those blocks) are obtained and saved into Matlab's workspace for further post-processing tasks.

Several time-domain simulations were performed, for small-signal frequencies from $10\,\mathrm{Hz}$ to $1000\,\mathrm{Hz}$, and droop gain M_{p1} varying from 0.1% to 4.0%. The results

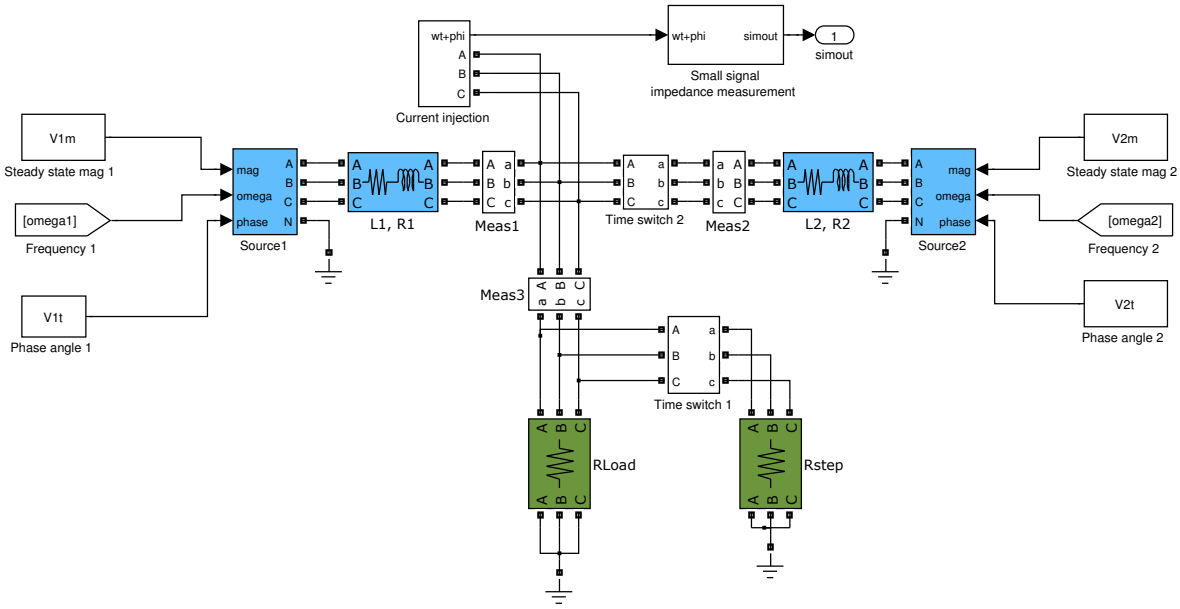

Figure 5.11: Current injection block diagram for frequency-domain simulations

are presented in Figure 5.12. A zoom over the low frequency region is shown in Figure 5.13. In these figures, the diamonds represent the time-domain simulation results for individual frequencies, and the continuous lines are the numerical results from the model.

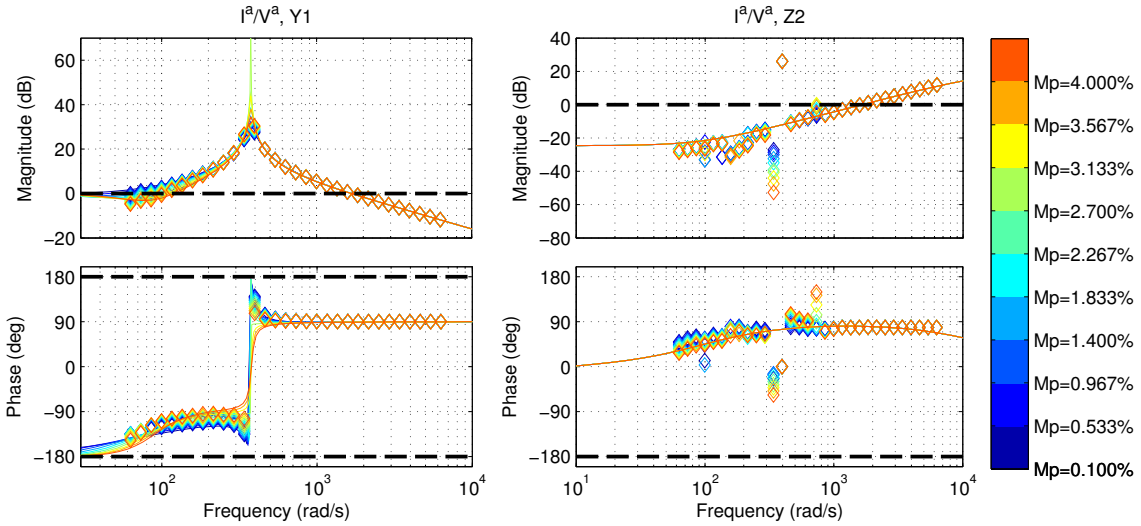

Figure 5.12: Frequency-domain simulation results for two microsources, resistive load system. Impedance (right) and admittance (left) bode plots are obtained by voltage and current injection respectively.

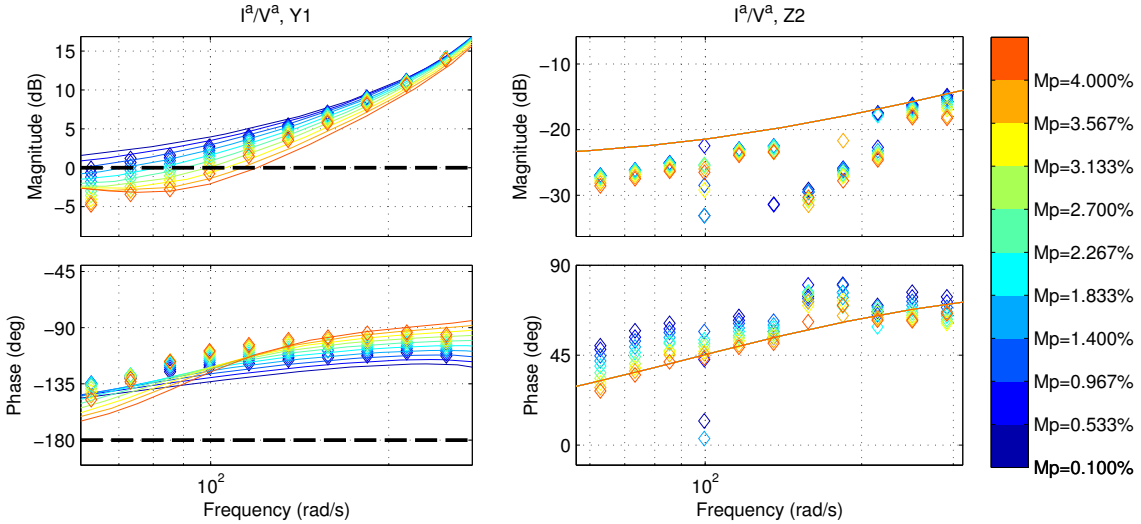

Figure 5.13: Frequency-domain simulation results for two microsources, resistive load system. Impedance (right) and admittance (left) are zoomed-in in the low frequency region.

5.5 Two microsources, R-L load

The two microsources, R-L load microgrid is remarkably similar to the two sources, resistive load case. In fact, the stability properties shown below are exactly the same. As in the single source cases, the introduction of the inductor load only creates slight differences in the impedance Z_2. Due to this similarity, the time-domain simulations were almost identical, and the simulation results are not presented in this section.

The eigenvalues of the full system are shown in Figure 5.14, where the base parameters of Table 3.1 are being used. Once again, the droop gain M_{p1} is varied from 0.1% to 6%. In addition to the group of complex-conjugate pairs of poles located far left from the imaginary, there are now a pair of complex conjugate poles close to the imaginary axis. In the zoom around the imaginary axis, shown at the right of Figure 5.14, it can be seen that these new poles do not move, and do not participate in the dynamics that destabilize the system.

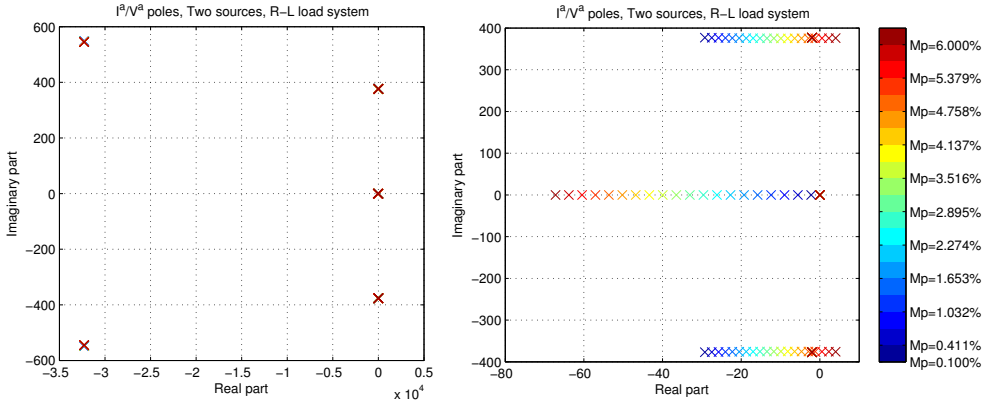

Figure 5.14: Root locus for two microsource, R-L load system. (A zoom around the origin is provided on the right plot)

Plots for the incremental phasor admittance Y_1 (Microsource 1) and impedance Z_2 (Microsource 2 and load) are shown in Figure 5.15. These impedance and admittance are almost identical to the ones shown in Figure 5.7.

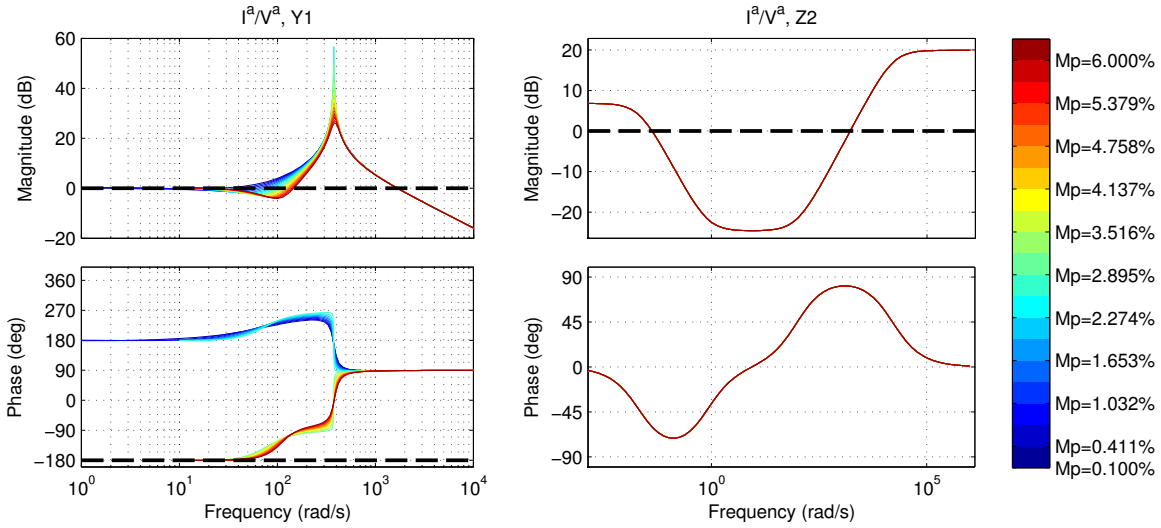

Figure 5.15: Incremental phasor impedance (right) and admittance (left) bode plots for two microsources, R-L load system

The open loop poles, along with the resulting loop gain Bode plots and Nyquist plots are shown in Figure 5.16 for selected values of droop gain M_{p1}. The Nyquist plot shows the same encirclements of the critical point and open-loop pole movement than the resistive load case in Figure 5.8. The system does not become unstable immediately after the open-loop poles become unstable, because the encirclements on the Nyquist plot go from zero to two at the same time. In the numerical results, the instability happens for a droop gain of $M_{p1} \approx 5.3\%$ as well. A zoom over the critical point in the Nyquist diagram and the imaginary axis in the pole-zero map is also shown in Figure 5.17.

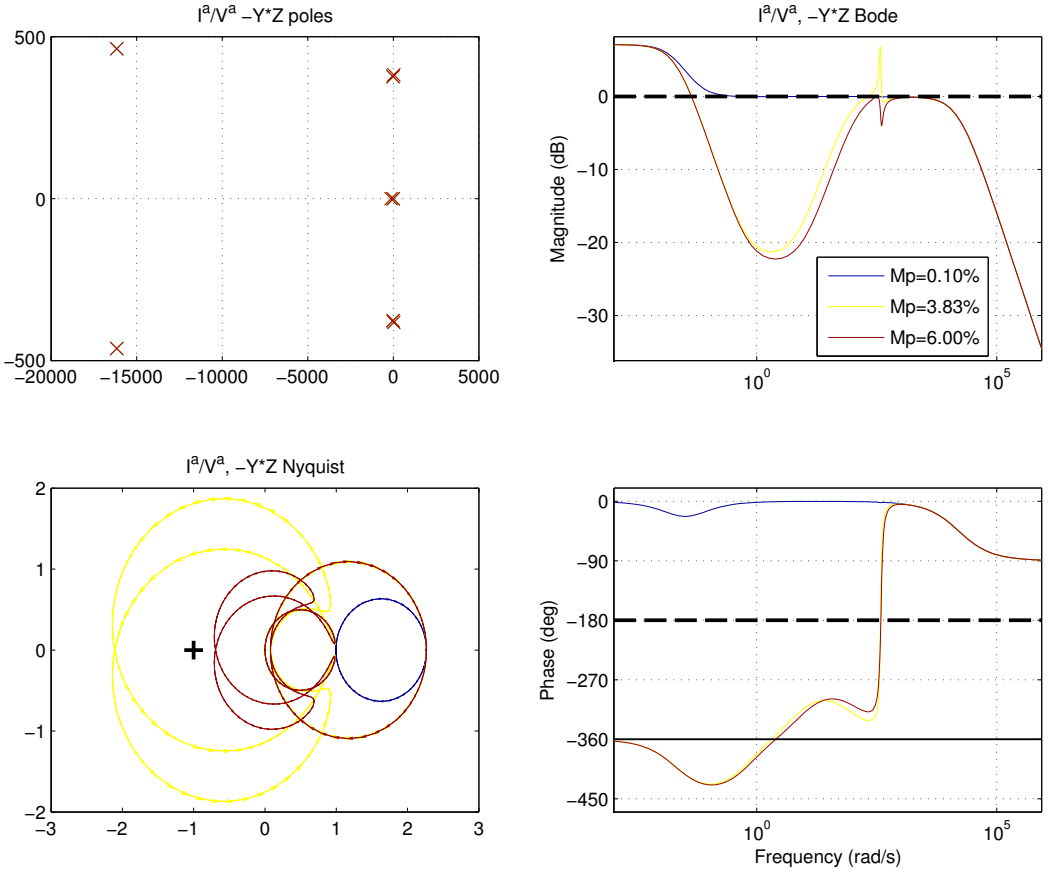

Figure 5.16: Plots for two microsources, R-L load system

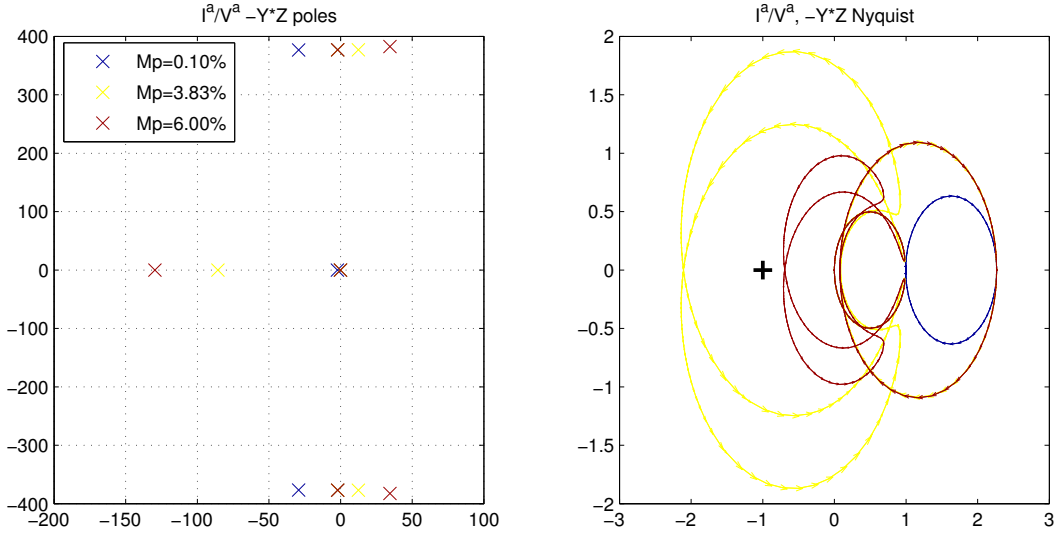

Figure 5.17: Detailed plots for two microsources, R-L load system. The result is very similar to Figure 5.9 .

5.6 Summary

In this chapter, a microgrid that comprises two microsources and a load was studied. The stability of this microgrid was established using the impedance matching stability criteria.

The results obtained with the analytical model match the results obtained by time-domain simulations. Power and frequency oscillations were observed for droop gains M_{p1} above 5.3%, as predicted by the model.

A measurement of the incremental phasor impedance was carried out using the time-domain simulation block diagram, injecting a small signal current or voltage. The incremental phasor impedances and admittances were successfully obtained, and closely match the results obtained with the microgrid analytical model. This is as important result that validates the method that can be used in hardware experiments.

6 LABORATORY-SCALE MICROGRID AT UW-MADISON

In this chapter, the impedance matching stability criteria will be validated in a laboratory-scale microgrid, by verifying that incremental phasor impedances are actually measurable in a hardware setup.

The existing microgrid at the University of Wisconsin-Madison is the perfect environment to carry out experiments that help validate the proposed stability study approach: it has two inverter-based microsources and several passive loads that are easily reconfigurable; the existing interconnection cables resemble a distribution network with realistic line parameters; the microgrid has a connection to the grid, hence experiments with a grid-tied microgrid are possible; and there is access to a variety of equipment that would make the validation task possible.

The first section introduces the UW Microgrid and its components. Section 6.2 introduces the modifications to the models presented in previous chapters that are necessary to take into account, while section 6.3 presents the simulation model with which the experimental results will be contrasted. Section 6.4 details the hardware and software necessary to conduct the experiments, and Section 6.5 presents the experimental results. The chapter ends with related discussion and conclusions.

6.1 UW Microgrid

The University of Wisconsin Microgrid is a hardware installation located in the Wisconsin Electric Machines and Power Electronics Consortium (WEMPEC) premises within the Electrical and Computer Engineering department. A diagram of the microgrid is presented in Figure 6.1.

6.1.1 Existing hardware and software

The most important components of the UW Microgrid are itemized below.

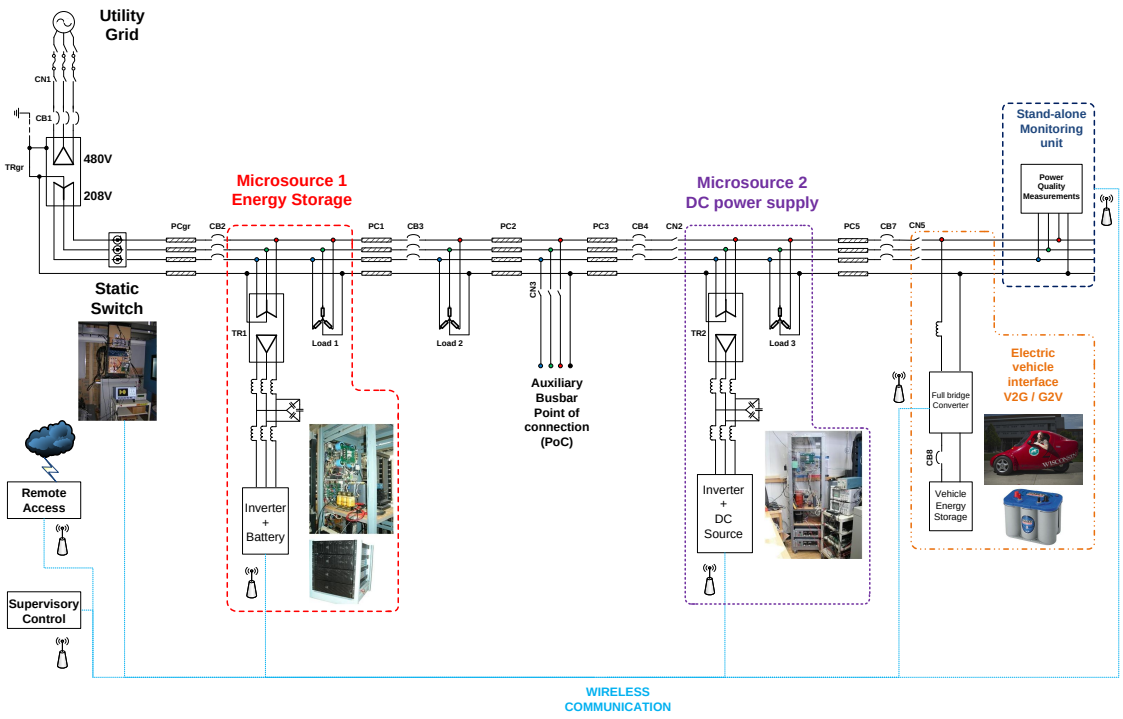

Figure 6.1: UW Microgrid schematic diagram

- *Microsources:* The UW Microgrid comprises two inverter-based distributed generators that were designed, built, and improved over the years by students [53, 33, 50]. The current generation model is a two-level, sinusoidal PWM, $480\,\mathrm{V}$ AC inverter with frequency and voltage droop control. The inverters have L-C-L filters at their outputs (L-C filter in addition to coupling inductor), and are coupled to the microgrid through $480/208\,\mathrm{V}$ transformers.

  One of the microsources has a $750\,\mathrm{V}$ lead-acid battery bank at its DC bus, thus acting as a battery energy storage system (BESS) [93]. The other microsource has a programmable DC power supply, which enables that microsource to mimic the behavior of different distributed generation technologies, such as photovoltaic panels, wind turbines, among others. These are shown in Figure

6.1 as Microsource 1 and Microsource 2 respectively.

The microsources are controlled remotely by a Labview interface that provides quick measurements and a control panel for the two inverters. Fundamental parameters such as the droop gains and power and voltage setpoints can be adjusted in this control panel. A screenshot of the control panel is shown in Figure 6.2.

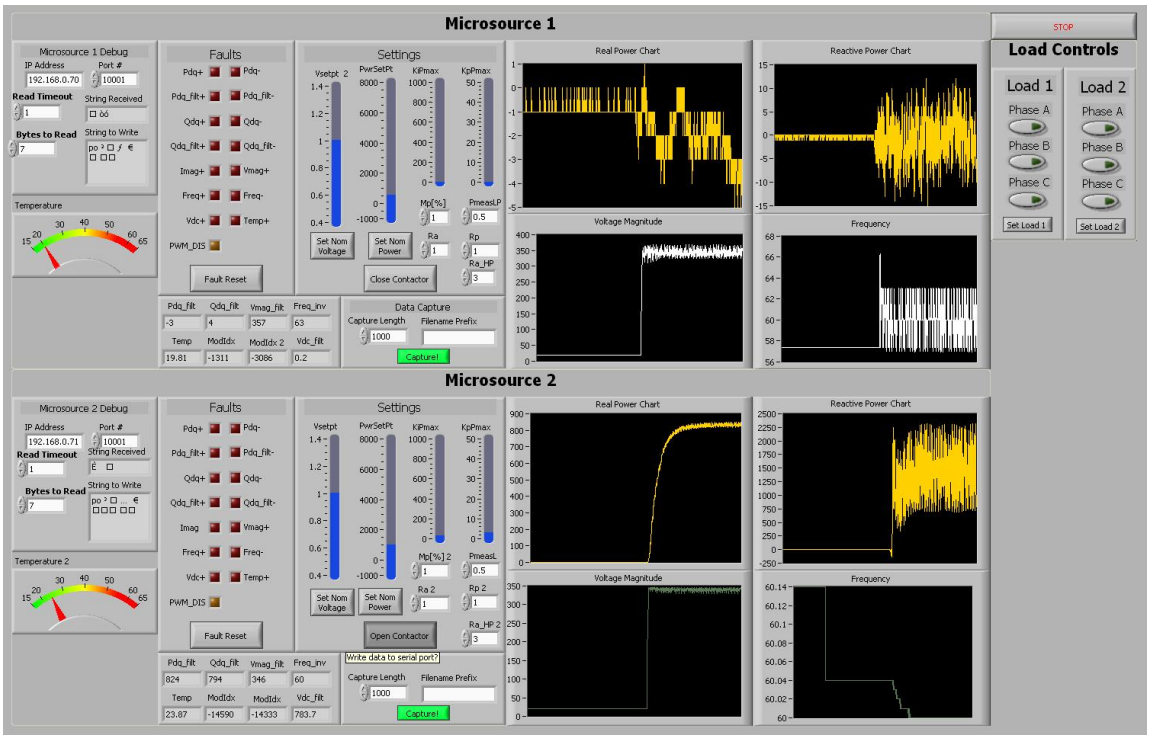

Figure 6.2: Labview control panel for microsources

- *Fixed and controllable loads:* There are several loads distributed within the microgrid. The loads are usually resistive, but capacitor and inductors could be easily added when needed.

  Some of the loads are remotely controlled by the Labview interface shown in Figure 6.2. These loads could be controlled phase by phase, thus are useful

when testing unbalanced conditions in islanded or grid-connected mode. These corresponds to Load 2 and Load 3 in the diagram in Figure 6.1.

Other loads are fixed, but are equipped with manual switches for disconnection during operation and/or maintenance. One of such loads is shown as Load 1 in Figure 6.1.

- *Static switch:* The static switch is the piece of equipment in charge of islanding the microgrid and (re)connecting it to the grid. It is governed by protection relays that oversee the power quality and operating conditions of the grid and the microgrid.

  The main component of the static switch is a set of six thyristors in anti-parallel configuration that are switched on and off by the protection relays.

- *Other components:* There are other components that were not actively used in the experiments. Among those components, there are several power quality monitoring stations (only one shown in Figure 6.1), which act as power quality events recorder and power meters.

  The microgrid has also the possibility of interfacing with electric vehicles, through a vehicle-to-grid (V2G) interface. This interface has been upgraded from simple single-phase chargers to three-phase full bridge converters that allow bidirectional power transfer between the vehicle's energy storage device and the microgrid. Experiments have been done in the microgrid [94], but are out of the scope of this thesis.

  There is an auxiliary bus, which is used as an internal PoC for the microgrid. This PoC will be used for the impedance measurements in the laboratory.

6.2 Incremental phasor models and impedances

The analytical models for the UW microgrid are the same already shown in Section 3.4. For example, the models for the loads are shown in (3.41), (3.47), (3.59) and (3.66).

In addition to the series impedance, the microsources now include an L-C filter and a transformer. This filter and transformer are modeled as an L-C section, as shown in Figure 6.3. What is shown to the left of the figure is the microsource model already presented in Figure 3.13, whose incremental phasor model is presented in (3.90). The magnetizing reactance of the transformer has been neglected in this model.

If we combine the series impedances together, naming $L_x = L_f + L_t$, $R_x = R_f + R_t$ and $C_x = C_f$, it is possible to write a relationship between the input voltage and output current of the microsource and the input voltage and output current of the filter:

$$\begin{aligned} \bar{V}_o &= (R_x + j\omega_o L_x)\bar{I}_m + \bar{V}_m \\ \bar{I}_o &= \bar{I}_m + j\omega_o C_x \bar{V}_o \end{aligned} \tag{6.1}$$

The phasor equation above can be properly written in terms of dynamic phasors as follows:

$$\frac{\mathrm{d}I_m^a}{\mathrm{d}t} = \frac{1}{L_x}\left(V_o^a \cos(V_o^\theta - I_m^\theta) - V_m^a \cos(V_m^\theta - I_m^\theta) - R_x I_m^a\right) \tag{6.2}$$

$$\frac{\mathrm{d}I_m^\theta}{\mathrm{d}t} = \frac{1}{L_x I_m^a}\left(V_o^a \sin(V_o^\theta - I_m^\theta) - V_m^a \sin(V_m^\theta - I_m^\theta)\right) \tag{6.3}$$

$$\frac{\mathrm{d}V_o^a}{\mathrm{d}t} = \frac{1}{C_x}\left(I_o^a \cos(I_o^\theta - V_o^\theta) - I_m^a \cos(I_m^\theta - V_o^\theta)\right) \tag{6.4}$$

$$\frac{\mathrm{d}V_o^\theta}{\mathrm{d}t} = \frac{1}{C_x V_o^a}\left(I_o^a \sin(I_o^\theta - V_o^\theta) - I_m^a \sin(I_m^\theta - V_o^\theta)\right) \tag{6.5}$$

The variables are chosen such that this L-C filter model can be connected in series with the microsource model of Equation (3.90). The state, input and output variables of the L-C filter model are:

$$x = \begin{pmatrix} I_m^a \\ I_m^\theta \\ V_o^a \\ V_o^\theta \end{pmatrix}, \quad u = \begin{pmatrix} I_o^a \\ I_o^\theta \\ V_m^a \\ V_m^\theta \end{pmatrix}, \quad y = x \tag{6.6}$$

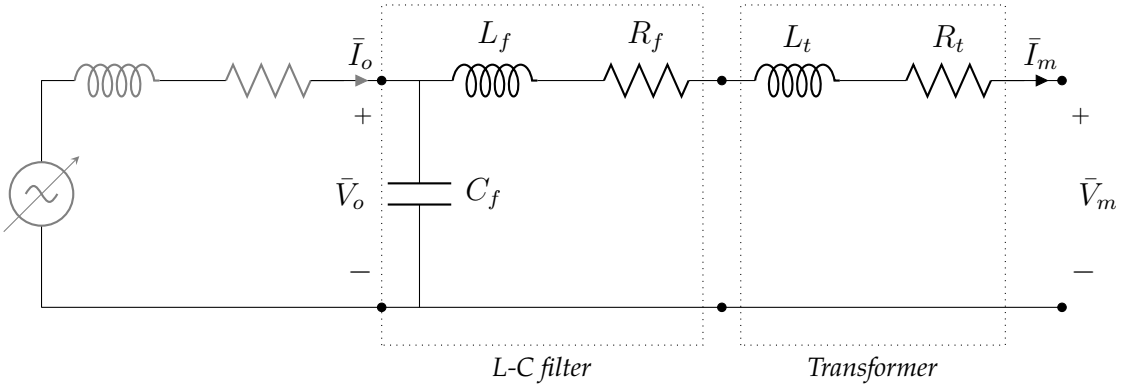

Figure 6.3: Schematic of the L-C filter and transformer

Using the same procedure outlined in Section 3.4, an incremental phasor model for the L-C filter can be obtained:

$$
\begin{aligned}
\dot{\tilde{x}} &= A\tilde{x} + B\tilde{u} \\
\tilde{y} &= C\tilde{x}
\end{aligned}
$$

$$
A = \begin{pmatrix}
-\frac{R_x}{L_x} & \omega_o I_m^A & -\frac{1}{L_x}\cos(V_o^\Theta - I_m^\Theta) & -\frac{V_o^A}{L_x}\sin(V_o^\Theta - I_m^\Theta) \\
-\frac{\omega_o}{I_m^A} & -\frac{R_x}{L_x} & \frac{1}{L_x I_m^A}\sin(V_o^\Theta - I_m^\Theta) & \frac{V_o^A}{L_x I_m^A}\cos(V_o^\Theta - I_m^\Theta) \\
-\frac{1}{C_x}\cos(I_m^\Theta - V_o^\Theta) & \frac{I_m^A}{C_x}\sin(I_m^\Theta - V_o^\Theta) & 0 & \omega_o V_o^A \\
-\frac{1}{C_x V_o^A}\sin(I_m^\Theta - V_o^\Theta) & -\frac{I_m^A}{C_x V_o^A}\cos(I_m^\Theta - V_o^\Theta) & -\frac{\omega_o}{V_o^A} & 0
\end{pmatrix}
$$

$$
B = \begin{pmatrix}
-\frac{1}{L_x}\cos(V_m^\Theta - I_m^\Theta) & -\frac{V_m^A}{L_x}\sin(V_m^\Theta - I_m^\Theta) & 0 & 0 \\
-\frac{1}{L_x I_m^A}\sin(V_m^\Theta - I_m^\Theta) & -\frac{V_m^A}{L_x I_m^A}\cos(V_m^\Theta - I_m^\Theta) & 0 & 0 \\
0 & 0 & \frac{1}{C_x}\cos(I_o^\Theta - V_o^\Theta) & -\frac{I_o^A}{C_x}\sin(I_o^\Theta - V_o^\Theta) \\
0 & 0 & \frac{1}{C_x V_o^A}\sin(I_o^\Theta - V_o^\Theta) & \frac{I_o^A}{C_x V_o^A}\cos(I_o^\Theta - V_o^\Theta)
\end{pmatrix}
$$

$$
C = \begin{pmatrix}
1 & 0 & 0 & 0 \\
0 & 1 & 0 & 0 \\
0 & 0 & 1 & 0 \\
0 & 0 & 0 & 1
\end{pmatrix}
$$

(6.7)

Figure 6.4 show how the admittance of a microsource change when including the L-C filter and transformer components into the model. The filter introduces

notorious changes in the high frequency region, where it is supposed to filter switching frequencies, while also distorting the admittance at low frequencies.

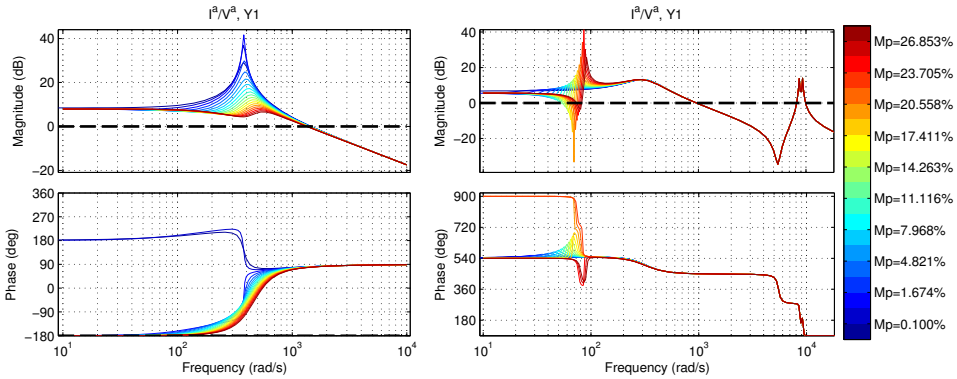

Figure 6.4: Comparison of microsource admittances without (left) and with (right) L-C filter

6.3 Simulation models

A full-featured model has been developed in Simulink, using SimPowerSystems blocks for the power system wiring, in the same fashion of the models presented in Section 3.6. An overview of this extended model is presented in Figure 6.5.

The system comprises several components of the UW Microgrid: the two microsources, two of the controlled loads, and the connection to the grid. This model greatly resembles the diagram of Figure 6.1 and includes enough components to be regarded as a close approximation of the existing hardware setup.

Existing laboratory transmission lines PCgr, PC1, PC2 and PC3 are represented by impedances Z2, Z3 and Z4 in Figure 6.5. Controllable loads are shown as well. The static switch is implemented as an ideal circuit breaker, and the grid model corresponds to the one of the "simple source" in Figure 3.18. The coupling transformers are represented by their series impedances, shown as T1 and T2 in the diagram.

The microsource model is strongly based in the model shown in Section 3.6, and is presented in Figure 6.5. The L-C filters are included, and shown in detail in Figure

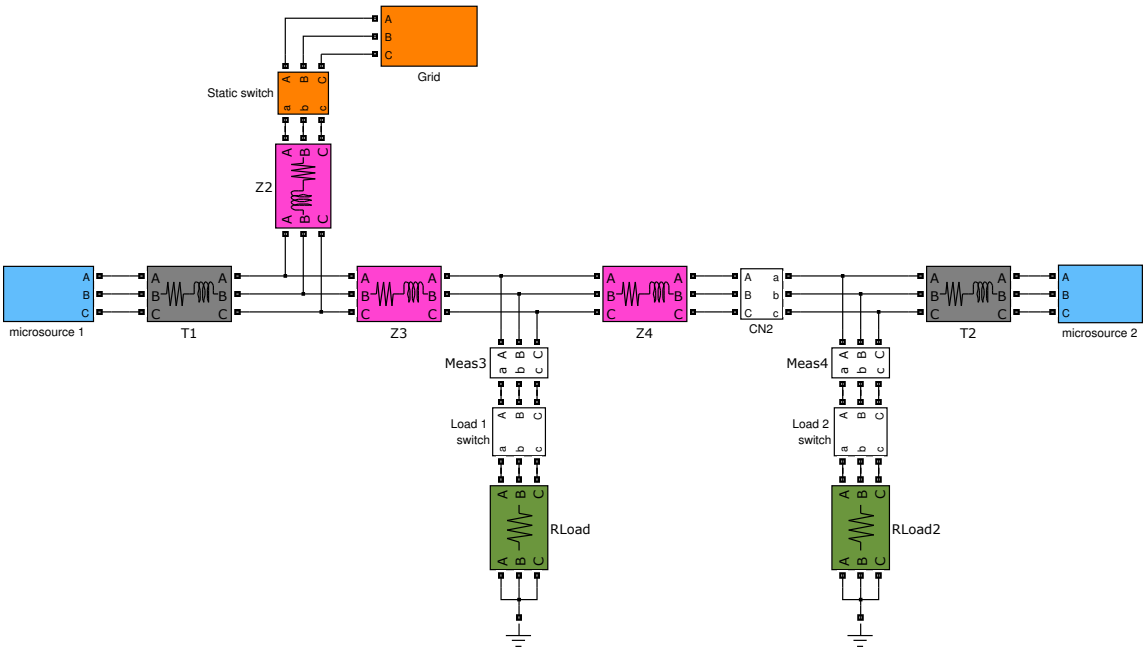

Figure 6.5: Overview of the UW Microgrid simulation block diagram

6.7. The droop controllers are the same shown in Figure 3.22. The parameters for these additional components are shown in Table 6.1

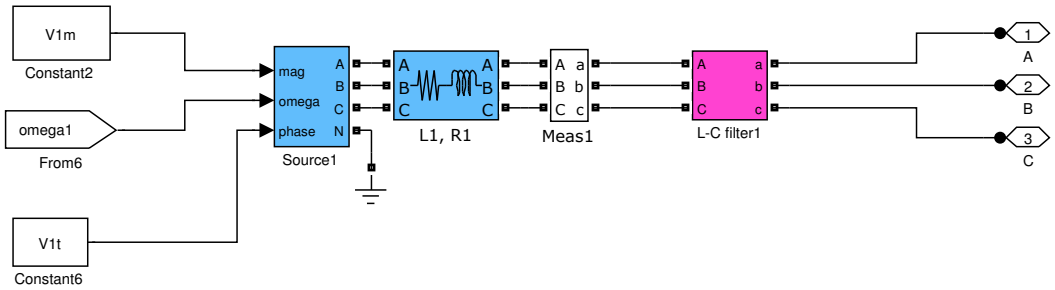

Figure 6.6: UW Microgrid microsource block diagram

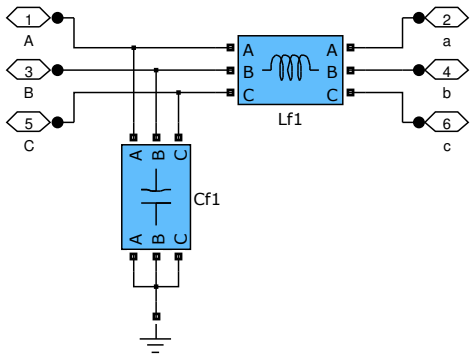

Figure 6.7: Details of the L-C filter for UW Microgrid microsource

Table 6.1: Parameters for additional UW Microgrid components

Parameter	Symbol	Value	Units
LC Filter inductance	L_f	0.3379	mH
LC Filter capacitance	C_f	53.2544	µF
LC Filter series resistance	R_f	0.026	Ω
Transformer series reactance	X_t	0.0481	Ω
Transformer series resistance	R_t	0.0481	Ω
Distribution line Z_2 reactance	X_{Z2}	0.00064	Ω
Distribution line Z_2 resistance	R_{Z2}	0.0049	Ω
Distribution line Z_3 reactance	X_{Z3}	0.0072	Ω
Distribution line Z_3 resistance	R_{Z3}	0.0547	Ω
Distribution line Z_4 reactance	X_{Z4}	0.0024	Ω
Distribution line Z_4 resistance	R_{Z4}	0.0182	Ω

6.4 Incremental phasor impedance measurement

The impedance measurement technique that was followed in this thesis is the small signal injection at the PoC. Currents and voltages of variable frequency are injected and selected frequency components are post-processed in order to identify the small-signal impedance or admittance of the systems. This schemes are shown in Figure 6.8.

The approach presented in this thesis has some similarities with the techniques

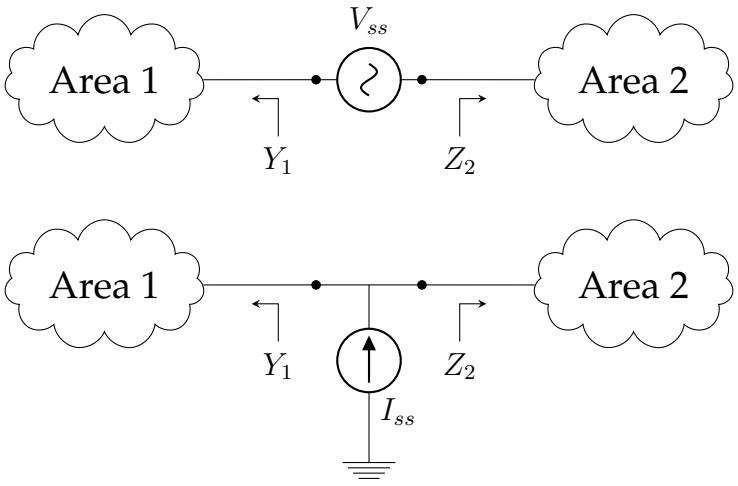

Figure 6.8: Small signal injection schemes for impedance measurement

presented in [69, 70]. Even though those articles theoretically cover both series and shunt injection, only shunt current injection is experimentally verified. As it will be shown below, the series voltage injection gives better results than shunt current injection in the covered microgrid cases.

6.4.1 Technique

As covered in Section 3.3, the dynamic phasors represent deviations on top of a rotating vector of constant, known frequency ω_o. In order for the injections to be regarded as deviations of this kind, the injected voltages and currents should be able to generate currents and voltages of the form

$$\begin{aligned} i_{ssa} &= I_{ss}\left(1 + A_s\cos(\omega_s t + \phi_s)\right)\cos(\omega_o t) \\ i_{ssb} &= I_{ss}\left(1 + A_s\cos(\omega_s t + \phi_s)\right)\cos(\omega_o t - 2\pi/3) \\ i_{ssc} &= I_{ss}\left(1 + A_s\cos(\omega_s t + \phi_s)\right)\cos(\omega_o t + 2\pi/3) \end{aligned} \tag{6.8}$$

$$\begin{aligned} v_{ssa} &= V_{ss}\left(1 + A_s\cos(\omega_s t + \phi_s)\right)\cos(\omega_o t) \\ v_{ssb} &= V_{ss}\left(1 + A_s\cos(\omega_s t + \phi_s)\right)\cos(\omega_o t - 2\pi/3) \\ v_{ssc} &= V_{ss}\left(1 + A_s\cos(\omega_s t + \phi_s)\right)\cos(\omega_o t + 2\pi/3) \end{aligned} \tag{6.9}$$

where A_s, ω_s and ϕ_s are the magnitude, frequency and phase angle of the injected small signal. The injection has to be correctly generated in this form, such that the rest of the system's currents and voltages have those modulated components as well.

By using trigonometric identities, it can be seen that, in fact, the absolute frequencies present in the system are the sum and difference of ω_o and ω_s (the amplitude A_s and phase angle ϕ_s of the injected signals are not shown for simplicity). For example, for the current on phase A,

$$i_{ssa} = \frac{I_{ss}}{2}\cos\left((\omega_s + \omega_o)t\right) + \frac{I_{ss}}{2}\cos\left((\omega_s - \omega_o)t\right) \tag{6.10}$$

One possible way of obtaining the correct signals is to inject these sum a difference components directly into the system. Another possibility is to directly generate the modulated components by actual modulation in the system. This last technique was chosen.

With the help of power electronics, voltages and currents are easily modulated. For example, PWM converters can be modulated to perform power quality tasks such as maintaining nominal voltage (the dynamic phasor's magnitude) for sensitive loads [95]. These kind of converters have the potential to perform the modulation task needed for the injection of modulated currents and voltages, which are necessary for the incremental phasor impedance spectroscopy.

As stated in Section 3.5, we are interested in the magnitude components of the incremental phasor impedances. Therefore, we are interested in magnitude modulation, easily achieved in PWM converters. Phase angle modulation, which would be also possible to obtain with converters (although at higher complexity), is not necessary for the purposes of this study.

Most of the materials covered in this section are also available in [96], a thorough

documentation of the experimental phase of this thesis.

6.4.2 Hardware

Three-phase PWM Buck converter

The AC PWM buck converter comprises six insulated gate bipolar transistors (IGBT) connected as buck converters in each phase, as shown in Figure 6.9. The converter topology details are covered in [95, 96].

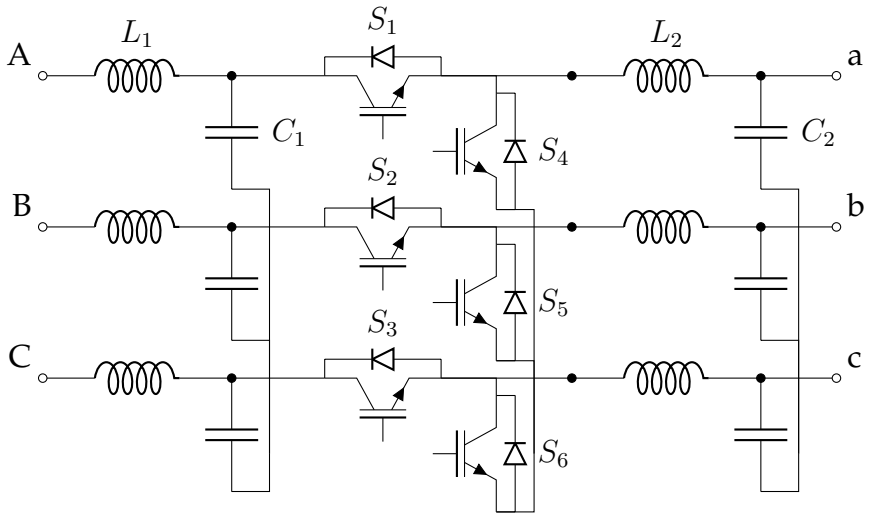

Figure 6.9: Schematic of the three-phase PWM Buck converter

The converter is interfaced through a Variac, because the buck converter operation always reduces the voltage at its output. Then, the Variac helps to increase the voltage magnitude at the input of the converter such that the output voltage can be adjusted to be higher or lower than the nominal or rated voltage.

The converter is operated with the three legs switched at the same time, being S_1, S_2 and S_3 switched with the PWM signal, and S_4, S_5 and S_6 switched with the inverted PWM signal. A constant PWM signal is equivalent to no modulation, and changes in the PWM command create the desired amplitude modulation.

The converter is then connected as shown in Figure 6.10. For the series voltage injection, the converter directly modulates the voltage across the PoC; this way, both sides of the converter see a modulated voltage, function of the PWM duty ratio. For the shunt connection, the converter cannot inject modulated current by itself; therefore, a burden resistor is connected at one of its terminals, such that the converter draws modulated current from the PoC. The amount of the injected (drawn) current is a function of the PWM duty ratio and the burden resistor R_b.

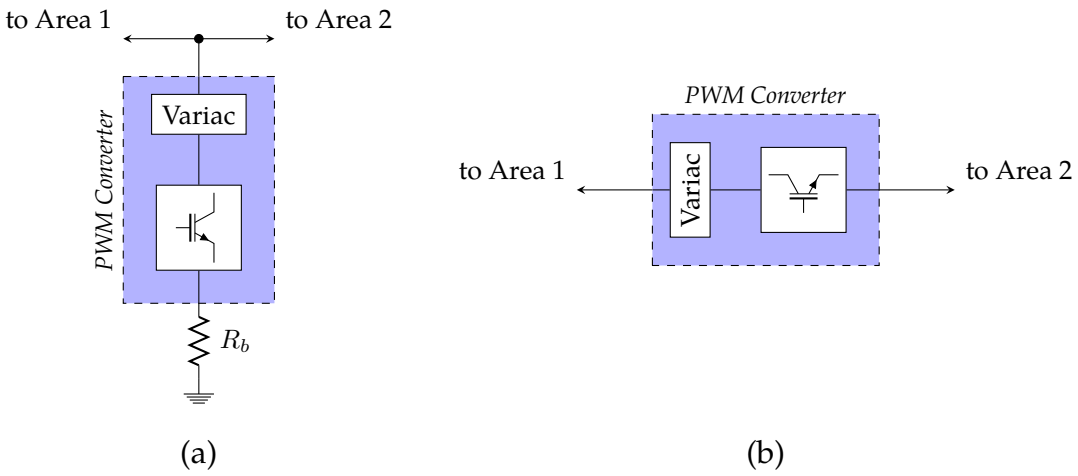

Figure 6.10: PWM Buck converter connection: (a) shunt current injection, (b) series voltage injection.

Microcontroller-based PWM control and software

The PWM control was programmed in a microcontroller evaluation board for the STM32 family of microcontrollers [97]. Using the programming features and developer's tools and libraries, a simple PWM controller was built. The switching frequency was chosen to be $10\,$kHz, a good compromise between converter losses and simplicity of input and output filter designs. The microcontroller has preset frequencies at which the voltage would be modulated, in a logarithmic scale that covers the range of $0.2\,$Hz to $200\,$Hz. The microcontroller board is shown in Figure 6.11(a).

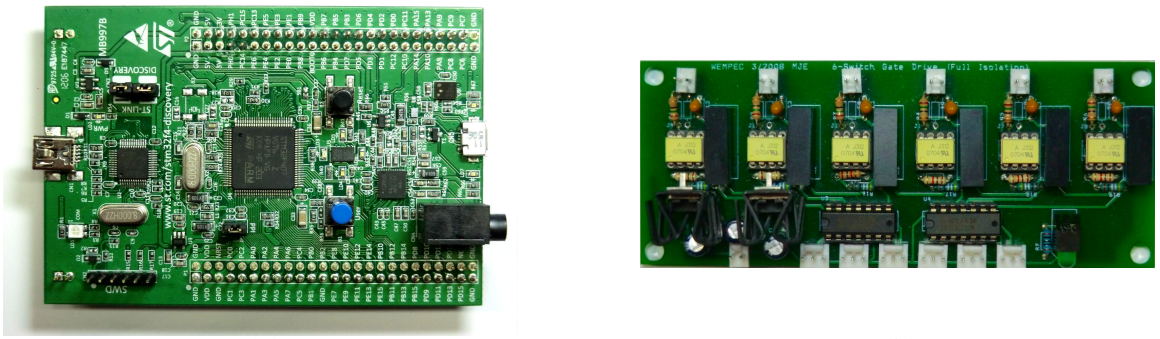

(a) (b)

Figure 6.11: (a) STM32-Discovery microcontroller evaluation board and (b) gate driver

The PWM pulses for S_1–S_3 and S_4–S_6 are both generated by software. This way, the IGBT dead time can be easily controlled. The PWM pulses are interfaced by a gate driver board, shown in Figure 6.11(b).

6.4.3 Data acquisition and small signal filtering software

The data acquisition is performed by the Yokogawa DL750 ScopeCorder [98], which combines the features of a multi-channel oscilloscope and a data acquisition recorder. From the available 12 channels, 6 channels were used for voltages and 6 channels for currents. For series voltage injection, voltages and currents at both sides of the converter were measured. For shunt current injection, the voltage at the PoC and the currents at both sides of the PoC were measured.

Once the voltages and currents are recovered from the oscilloscope recordings, the waveforms are post-processed in Matlab, where the Fourier components corresponding to the modulation frequency are obtained. Algorithms using the Fast Fourier transform (FFT) and the short-term Fourier transform (STFT) were tested, giving both very similar results. This processing technique was already used in Section 5.4.3 for the frequency-domain simulations of a two-source microgrid.

6.5 Experimental results

The experiments that were carried out on the UW Microgrid are divided in three classes:

- *Passive loads incremental impedance*: Being these loads the ones with less complex models, their impedances (or admittances) were measured to verify that the incremental phasor impedances are in fact measurable.
- *Microgrid impedance spectroscopy*: The full microgrid hardware setup was used while measuring incremental phasor impedances of two areas, both in islanded and grid connected modes.
- *Microgrid stability margins*: The full microgrid was driven at its limit, making the system go into instability. By using the microgrid models, it is possible to estimate at which point the microgrid is actually going into unstable operating mode, and this was verified in the laboratory.

6.5.1 Incremental phasor impedances of passive loads

By connecting a load directly to the grid, a PoC is established at the terminals of such load. The small signal injection (both series and shunt) was tested in several passive loads. The results for the individual loads are given below.

Resistor

A delta-connected three-phase resistor of resistance $R = 75\,\Omega$ was used on this experiment. The impedance of the resistor is shown in Figure 6.12. As expected, the resistor had a constant impedance, regardless of frequency injection, equal to R (approximately 28 dB), and zero phase shift. This experiment shows the results for series voltage injection.

The results for shunt current injection were not as good as the ones for series voltage injection. In Figure 6.13, both results are presented in the same plot, along with the theoretical resistor impedance. It can be clearly seen that the results for

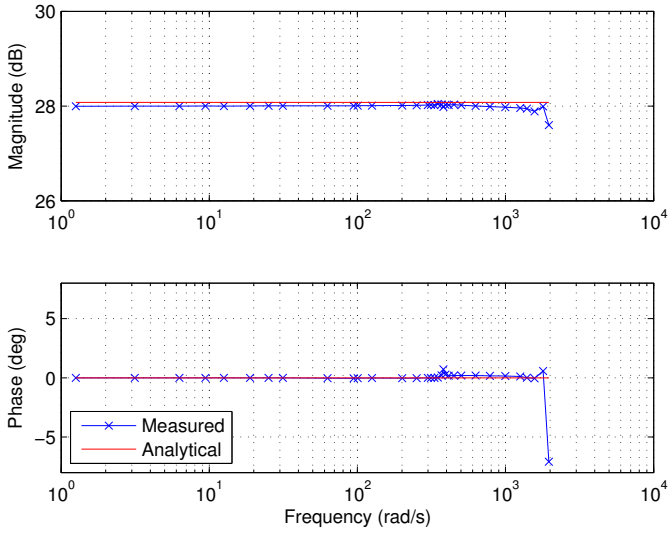

Figure 6.12: Measured incremental phasor impedance for resistive load

current injection method are more noisy, specially for frequencies near 60 Hz, and differences of more than 1 dB are shown for low frequencies, which is the range of interest for our experiments.

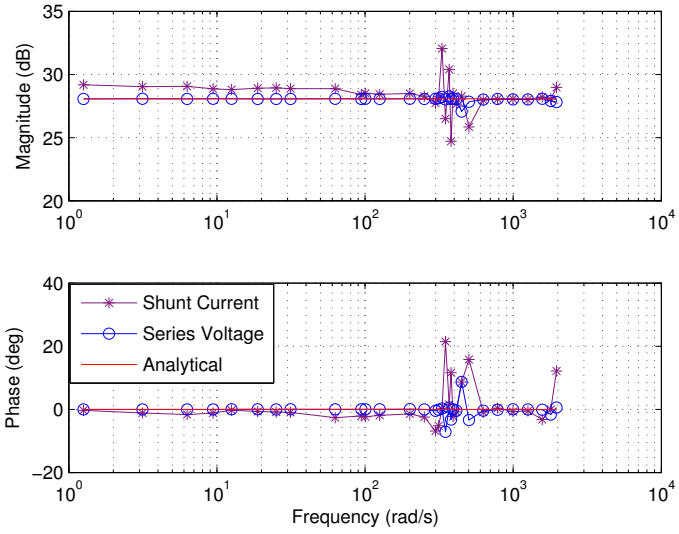

Figure 6.13: Comparison of series and shunt injection on a resistive load

For this reason, series voltage injection will be preferred over shunt current injection. The rest of the loads' incremental phasor impedances were also measured by series voltage injection.

R-C load

A delta-connected three-phase R-C parallel load was also measured in the laboratory. The resistance is $R = 38\,\Omega$ and the capacitance is $C = 24\,\mu\text{F}$. Its impedance is shown in Figure 6.14, along with the theoretical impedance. There is an extremely good match for this kind of load as well. For frequencies above $200\,\text{Hz}$ ($1250\,\text{rad}\,\text{s}^{-1}$), the filters present in the system start to interact with the injected signals, negatively impacting the results. Only a couple points above this frequency are shown.

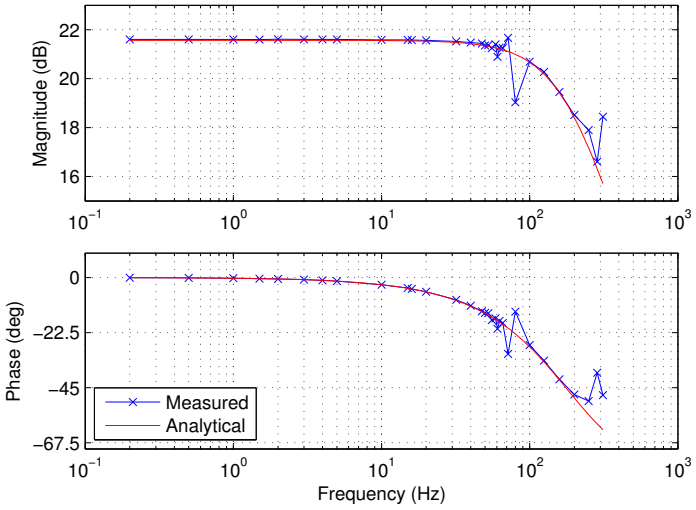

Figure 6.14: Measured incremental phasor impedance for R-C parallel load

R-L load

A delta-connected three-phase R-L series load was measured in the laboratory as well. The inductance is $L = 30.5\,\text{mH}$, and the resistance $R = 0.9\,\Omega$ is the inductor's own resistance, so no external resistor was necessary. The incremental phasor admittance measurement results are shown in Figure 6.15, along with the

theoretical admittance. The differences between the theoretical and experimental admittances could be attributable to the existence of additional damping resistance in the system, which might not be considered in the theoretical model.

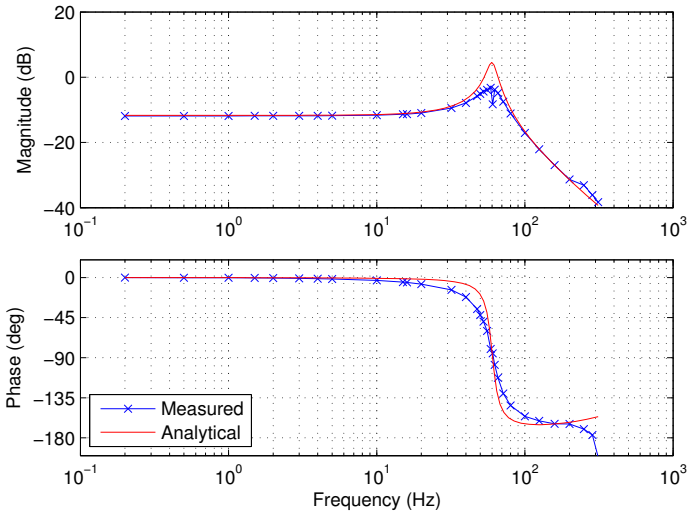

Figure 6.15: Measured incremental phasor admittance for R-L series load

6.5.2 Impedance spectroscopy at the UW Microgrid

The incremental phasor impedance measurement of two areas of the UW microgrid is presented in this section. As pointed out above, there is an auxiliary bus denominated as the PoC of the microgrid, shown in Figure 6.1. From this point, the microgrid is conceptually split in two areas. One of the areas contain Microsource 2 and loads. The other area contains Microsource 1 and the connection to the grid, along with some other loads.

Several experiments were carried out under this configuration, under which it is only possible to inject small signal shunt currents. Even though it was discussed above that the series voltage injection provides better measurements, the complexity of inserting the converter in series with the microgrid, along with the difficulties of controlling the converter while series connected, discouraged the use of the series voltage injection technique.

Two impedance measurement experiments are presented below.

Single microsource, resistive load

A single microsource connected to a resistive load was studied as the natural step after the successful measurement of passive loads. The results of the measurement, contrasted with the analytical model, are shown in Figure 6.16. At the left of this figure, the admittance of the microsource is presented. At the right of the figure, the impedance of the resistive load is shown.

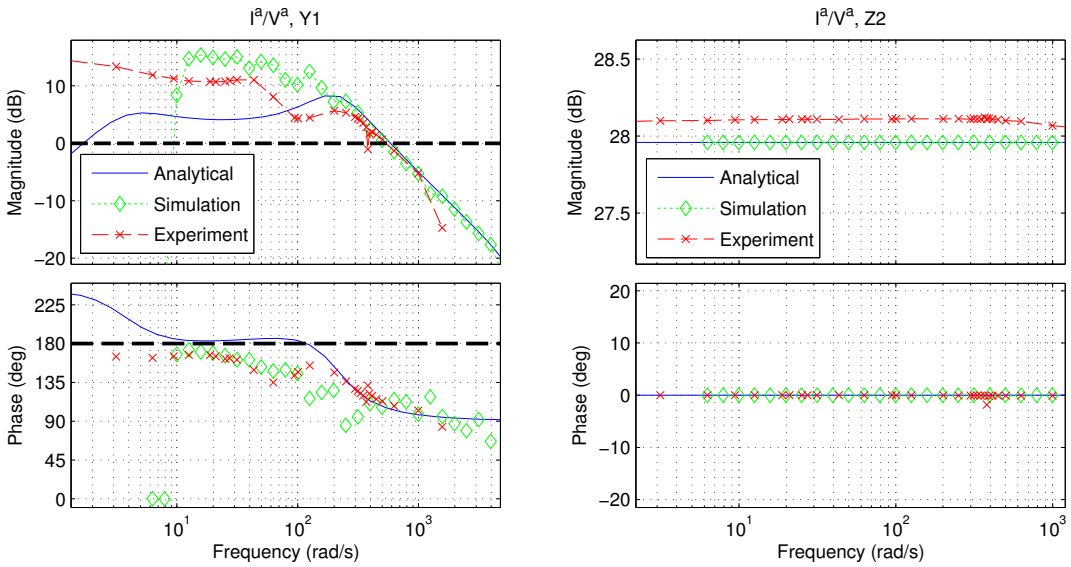

Figure 6.16: Incremental phasor impedances of the single microsource, resistive load case

The experimental results for the resistive load side closely match the analytical model. The same is not true for the microsource, as the experimental admittance magnitude departs from the analytical model for low frequencies, although maintaining a fairly close phase angle.

Two microsources, grid connected

Another interesting experiment was carried out while the microgrid was parallel to the utility grid. The results of this experiment are shown in Figure 6.17, where the left plot shows the incremental phasor admittance of Microsource 2, and the right plot shows the incremental phasor impedance of the grid.

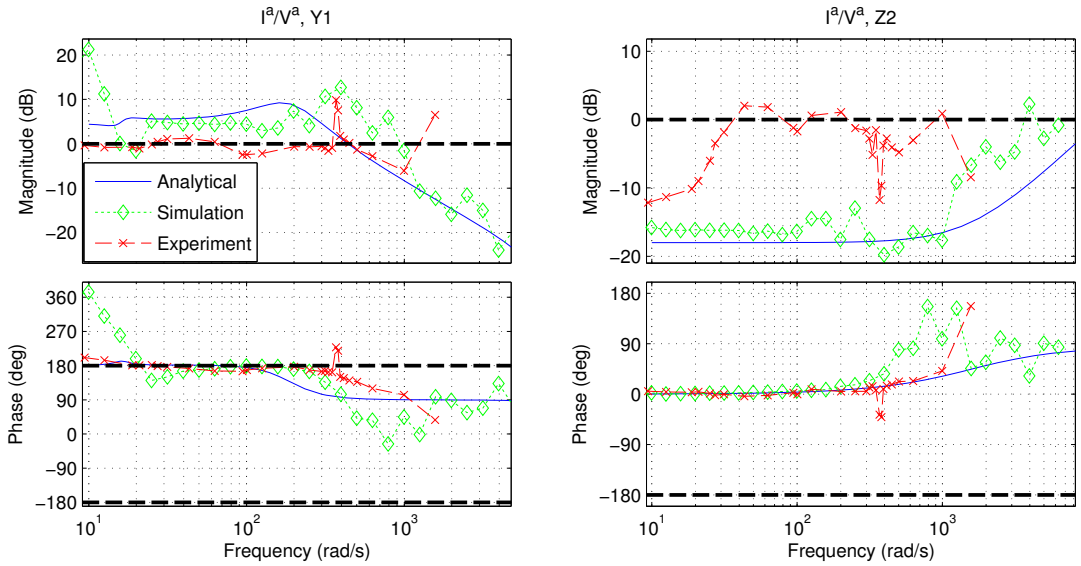

Figure 6.17: Incremental phasor impedances of the microsource connected to the grid

This particular experiment is very challenging, as the impedance of the grid is usually low and, in most cases, unknown. By injecting small signal currents into the system, it is very difficult to generate, under the presence of the grid, the small voltage perturbations needed to determine the incremental phasor impedances.

Discussion

As shown in the previous experiments, the measurement of relatively large passive load impedances closely match their analytical models. However, for more complex systems such as a microsource, the results present notorious discrepancies. This

was mainly due to the difficulties in maintaining a constant operating point during the experiments.

As these experiments were done using shunt current injection, some noise in the results was expected. However, larger discrepancies are due to the same injection, which needed to be fairly large at some frequencies and modified the operating point. The low impedance values for distributed energy sources (inverter-based or inertial) increase the complexity of the measurements, and could endanger the application of this technique on larger systems. Moreover, the experiments took, in practice, several minutes, rendering the technique useless in systems with fast-varying operating points, which is the common case of a dynamically changing microgrid.

One possible solution is to use impulse-based methods, covered in Section 2.4.1. Those methods, along with others such as noise-injection-based, could help determine the impedances in a shorter time. However, the may need to be adapted for the incremental phasor impedance measurements, because these impedances are a result of magnitude modulation of currents and voltages rather than a simple side-frequency small signal injection.

6.5.3 Stability margins at the UW Microgrid

Studying stability margins by experiments is a difficult task. On the one hand, there are risks of putting the system into a dangerous operating condition, which could cause serious equipment problems depending on the installation, not to mention safety risks. On the other hand, the protection schemes incorporated into many devices may not permit at all the operation of equipment near the stability limits. The last is true at the UW microgrid, where the inverters are equipped with fast acting protection that disables the system under dangerous current levels or out of bound frequencies, among other control features.

Before the experiments of this section were carried out, the stability margins were obtained by the analytical and simulation models. For example, using the analytical model of the UW Microgrid, it was established that, for the two microsources in

islanded operation, certain combinations of droop gains M_{p1} and M_{p2} may cause instabilities.

The case exposed here comprises the Microsource 2 with a droop gain of $M_{p_2} = 30\%$, a relatively high value that would put the system into a stability limit if the Microsource 1 droop gain is above a certain value.

Figure 6.18 shows the impedance and admittance of the two portions of the microgrid under this operating condition. The droop gain M_{p1} is varied from 1% to 30%.

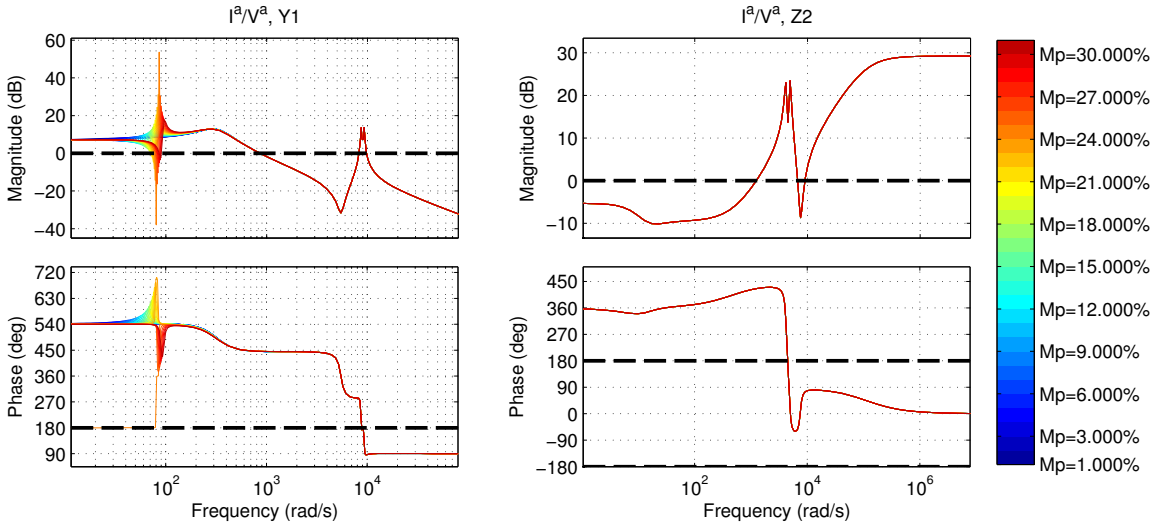

Figure 6.18: Incremental phasor impedances of an islanded microgrid

During the numerical calculations, it was determined that the system would hit an unstable operation for $M_{p1} > 25\%$. This is analyzed by using the impedance matching stability criterion over the range of operating points of varying M_{p1}. Figure 6.19 shows the Nyquist plot, Bode plot and open-loop root locus of three cases, with M_{p1} equal to 1%, 16% and 30% respectively. It can be seen in the picture that, for gains 1% and 16%, the encirclements of the critical point are none and the open-loop poles are on the left hand side of the complex plane, hence the system is stable. For a droop gain of 30%, however, the encirclements are still none, with two unstable poles.

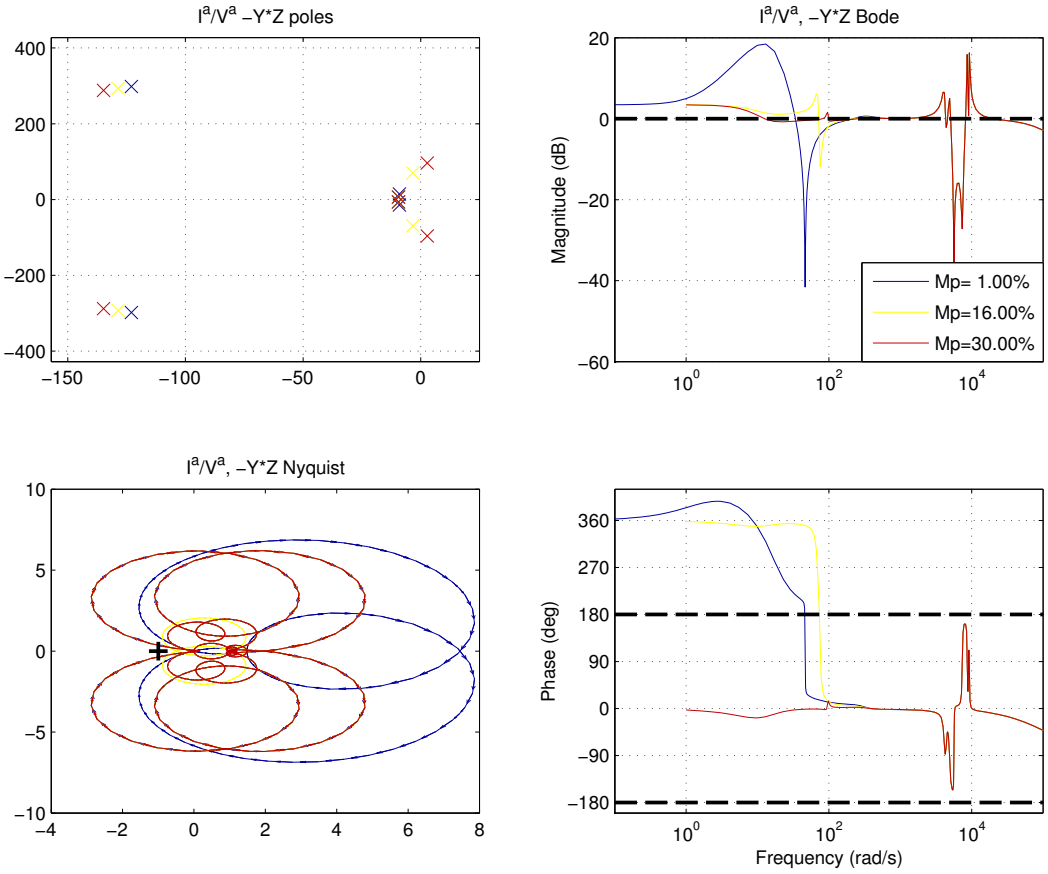

Figure 6.19: Plots for an islanded microgrid

These three cases were tested in the lab, during the impedance spectroscopy process. While injecting a low frequency perturbation into the system, the droop gain of the Microsource 1 was changed from 1% to 16%, then to 30%. The droop gain of Microsource 2 was equal to 30%. The simulation results and experimental results are shown side by side in Figures 6.20, 6.21 and 6.22 respectively. It can be seen that there is a close correlation between the simulated waveforms (in terms of amplitudes and frequencies) and the experimental results, despite the low frequency injection occurring at the same time.

An interesting fact is that, by controlling the impedance or admittance of a component of the microgrid, it could be possible to move the system away from

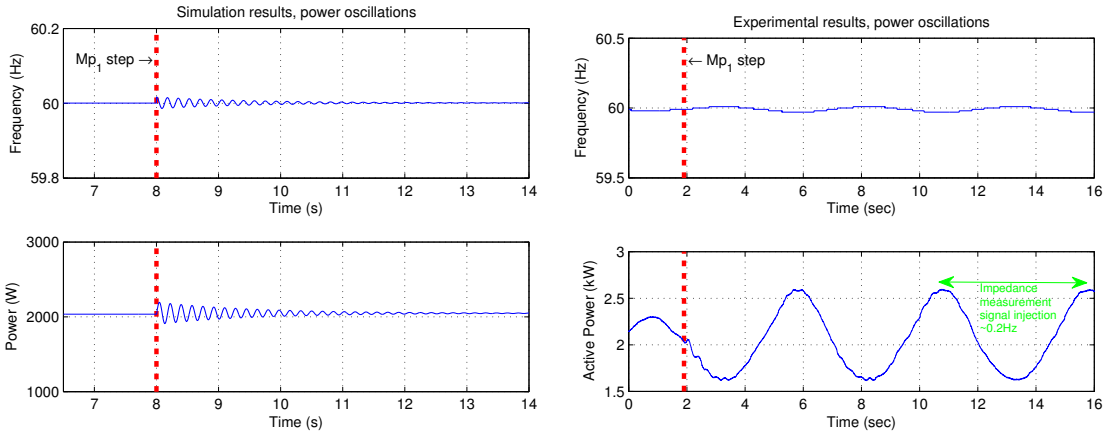

Figure 6.20: Power oscillations for $M_{p1} = 1\%$, $M_{p2} = 30\%$

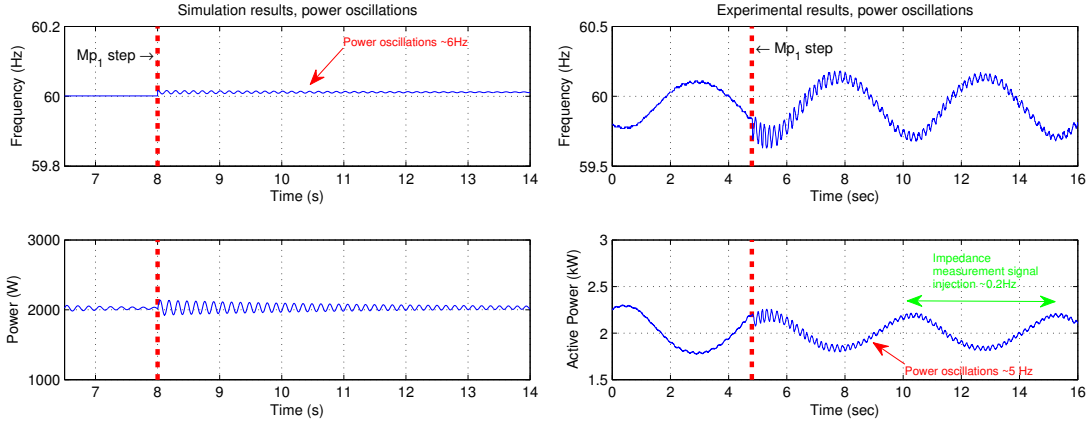

Figure 6.21: Power oscillations for $M_{p1} = 16\%$, $M_{p2} = 30\%$

instability. In Figure 6.23, a simulation result for a system recovery action is presented. The model used for this simulation is the one presented in Figure 6.5, in islanded operation. Microsource 2 has a droop gain of $M_{p2} = 30\%$. At time $t = 7.0\,\text{s}$, the impedance of Microsource 1 is modified by reducing its equivalent reactance, moving the system into unstable operation. At time $t = 8.0\,\text{s}$, a corrective action is introduced into the simulation, and the droop gain of Microsource 2 is reduced to $M_{p2} = 7.5\%$. The system resumes normal operation after the corrective measure.

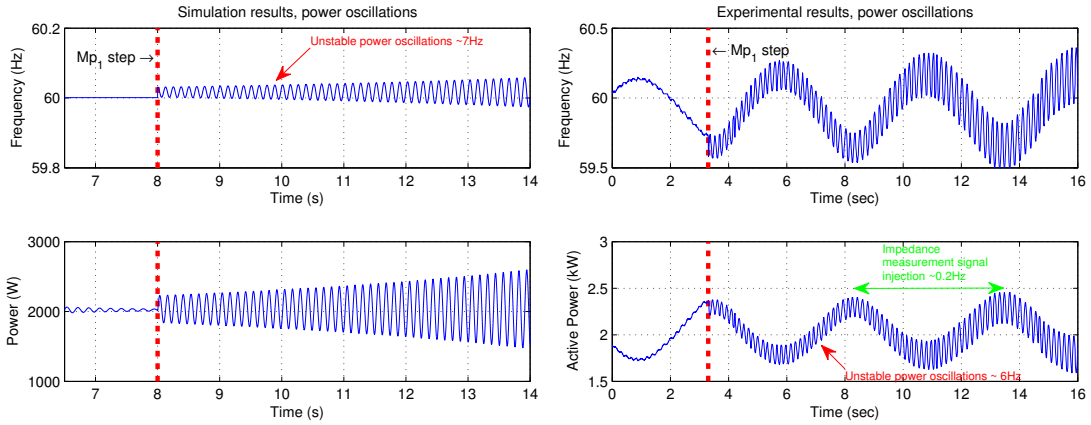

Figure 6.22: Power oscillations for $M_{p1} = 30\%$, $M_{p2} = 30\%$

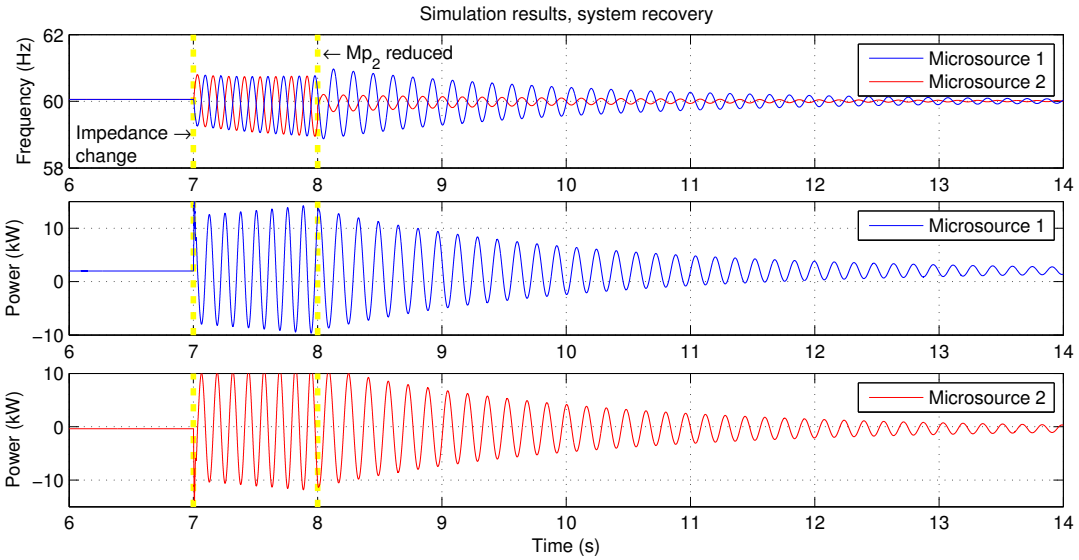

Figure 6.23: Simulation results for a system recovery action

In this thesis, the studies have been mainly carried out over variations of the droop gains M_p. But the impedance, as shown in the analytical models of Chapter 3, is a function of a much larger collection of parameters. The same corrective action could have been done, for example, by modifying operating voltage or incorporating virtual impedance.

6.6 Summary

In this chapter, the impedance matching based stability criteria was verified on a laboratory scale microgrid. The UW Microgrid was an invaluable hardware installation that allowed several configurations and operating conditions to be tested.

The incremental phasor model of the microsource was expanded to include the L-C filter found on the hardware setup. The addition of this filter generated changes in the incremental phasor impedance and admittance, and its model was incorporated in all analytical and simulation results presented in this chapter.

The phasor measurement technique was detailed in Section 6.4, in which both series voltage injection and shunt current injection were projected to be used. In the experimental setup, series voltage injection was used for the measurement of passive loads, and shunt current injection was used for the measurement of the full microgrid.

The experiments covered the measurement of the impedance of passive loads, which showed an excellent match with the analytical models. Resistive, R-C and R-L loads were tested.

The impedance spectroscopy was done with a single microsource and resistive load in islanded condition, and a microsource connected to the grid. Both experiments showed good results, although some discrepancies between the models were found, specially at low frequencies. Nevertheless, the results exposed in section 6.5 indicate that some features are missing from the analytical and simulation model. For example, the simulation models give a better approximation of the experimental results, but at the same time they share similarities with the analytical models. Full-featured simulation models can resemble the physical installation with more detail than a simplified analytical model, and could give insight about what components need to be modeled in a better way.

The microgrid was also put a its limits while validating the stability margins given by the incremental phasor model. Droop gain limits were recognized by the analytical model, determining that some combinations of droop gains may drive

the system to unstable operation. The unstable operation was indeed obtained for droop gains out of the limits determined by the models.

As an example of the benefits that the incremental phasor models could offer, a "system recovery" simulation was carried out. In this simulation, the system was modified to generate an unstable operating condition. By understanding the dynamics of the microsource, and having the ability to set controller gains, the system was taken out of the unstable region.

7 DYNAMIC PHASOR MODEL FOR COMPLEX LOADS

In this chapter, two additional kinds of loads will be modeled using the dynamic phasor technique detailed in Chapter 3. It is of interest to model the components that, in practice, one would face when working in a microgrid environment. Being the microgrid an active research area, there exist a large variety of components that would be very difficult to consolidate in simpler models such as the ones shown in previous chapters.

To broaden the scope of this thesis, two extra models are introduced. First, the induction machine is introduced in the dynamic phasor modeling. The motivation to model an induction machine is its wide popularity in several applications, including microgrids, both as motor and as generator. Basic induction machine models are introduced at this stage.

Second, constant power loads are introduced. Being this another type of popular component, constant power loads are found in many applications, usually as a power converter with integrated controls. Its analytical development would bring some challenges for the modeling techniques already presented in this thesis.

7.1 Induction machine

The induction machine model presented in this section is based on the traditional d-q axis model [99, Ch. 2], which has been expressed in voltage and current variables to make it compatible with the formulations of Section 3.4. The d-q model is converted into dynamic phasor variables (polar coordinates) and further developed to obtain the *incremental phasor model* and *incremental phasor impedance* of the induction machine.

For the purposes of this section, it will be assumed that the machine is operating as a motor. The rotor of the machine will be assumed short-circuited, as in a

squirrel cage induction machine. As a first approach, the machine will be modeled for constant speed operation; later, this constraint will be relaxed.

7.1.1 Dynamic phasor model for the induction machine

The induction machine model, in the synchronous reference frame using complex variables and matrix notation, is shown in (7.1), where the derivative is expressed using the operator $\mathcal{P}$.

$$\begin{pmatrix} v_s \\ 0 \end{pmatrix} = \begin{bmatrix} r_s + (\mathcal{P} + j\omega_e)L_s & (\mathcal{P} + j\omega_e)L_m \\ (\mathcal{P} + j(\omega_e - \omega_r))L_m & r_r + (\mathcal{P} + j(\omega_e - \omega_r))L_r \end{bmatrix} \cdot \begin{pmatrix} i_s \\ i_r \end{pmatrix} \tag{7.1}$$

The parameters r_s and r_r represent the winding resistance of the stator and the rotor; L_s and L_r are the stator and rotor inductances, which are equal to the leakage inductances L_{ls} and L_{lr}, plus the mutual inductance L_m. The rotor speed is ω_r and the synchronous reference frame is rotating at ω_e. An equivalent circuit is shown in Figure 7.1. In this figure, $\lambda_s = L_s i_s + L_m i_r$ and $\lambda_r = L_r i_r + L_m i_s$.

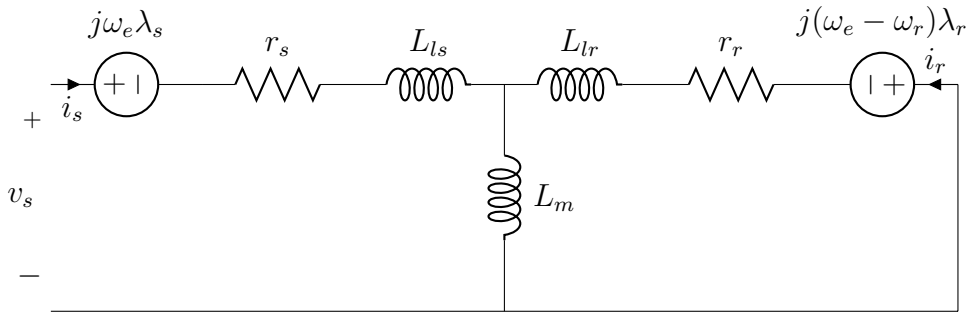

Figure 7.1: Schematic of the induction machine model in complex variables

In order to convert the model to a dynamic phasor equivalent, it is necessary to isolate the derivative terms. Those terms correspond to those of the stator current

i_s and rotor current i_r:

$$\mathcal{P}\begin{pmatrix} i_s \\ i_r \end{pmatrix} = \begin{bmatrix} Ls & L_m \\ L_m & L_r \end{bmatrix}^{-1} \cdot \begin{pmatrix} V_s \\ 0 \end{pmatrix} - \begin{bmatrix} r_s + (\mathcal{P} + j\omega_e)L_s & j\omega_e L_m \\ j(\omega_e - \omega_r)L_m & r_r + j(\omega_e - \omega_r)L_r \end{bmatrix} \cdot \begin{pmatrix} i_s \\ i_r \end{pmatrix} \tag{7.2}$$

Developing further, it is possible to obtain the matrix equations for the induction machine:

$$\mathcal{P}\begin{pmatrix} i_s \\ i_r \end{pmatrix} = \frac{1}{L_s L_r - L_m^2} \cdot \begin{bmatrix} Lr & -L_m \\ -L_m & L_s \end{bmatrix} \cdot \begin{pmatrix} v_s - r_s i_s - j\omega_e L_s i_s - j\omega_e L_m i_r \\ 0 - j(\omega_e - \omega_r)L_m i_s - j(\omega_e - \omega_r)L_r i_r - r_r i_r \end{pmatrix} \tag{7.3}$$

The system could be further expressed in a state space representation (as in (3.1)) as follows:

$$\begin{aligned} \mathcal{P}\, i_s = \frac{L_r}{L_s L_r - L_m^2} \Bigg(& v_s - r_s i_s - j\omega_e L_s i_s - j\omega_e L_m i_r + j(\omega_e - \omega_r)\frac{L_m^2}{L_r} i_s \\ & + \frac{L_m}{L_r} r_r i_r + j(\omega_e - \omega_r) L_m i_r \Bigg) \end{aligned} \tag{7.4}$$

$$\begin{aligned} \mathcal{P}\, i_r = \frac{L_m}{L_s L_r - L_m^2} \Bigg(& - v_s + r_s i_s + j\omega_e L_s i_s + j\omega_e L_m i_r - j(\omega_e - \omega_r) L_s i_s \\ & - \frac{L_s}{L_m} r_r i_r - j(\omega_e - \omega_r)\frac{L_s L_r}{L_m} i_r \Bigg) \end{aligned} \tag{7.5}$$

The conversion of the system from complex variables to dynamic phasor quantities is direct: it is a conversion from rectangular to polar coordinates. This is due to the fact that the model is expressed in the synchronous reference frame. Hence, the stator variables would be seen as DC in this frame, the same as the dynamic phasors for constant rotating angular frequency equal to the system's frequency ω_o.

An algorithmic way of developing the equations is the following:

1. Begin with the model of a system in d-q coordinates. Express the model in the synchronous reference frame, such that this reference frame is rotating at the desired dynamic phasor known frequency ω_o.

2. Express the equations in the form presented above, i.e. the derivative of state variables as functions of other variables.

3. For each complex state variable x_i, define two dynamic phasor variables X_i^a and X_i^θ that will represent the magnitude and phase angle of the complex variables. Do the same for input variables u_j and output variables y_k

4. Write the equation for the magnitude variable X_i^a by "projecting" every term of the right hand side of the complex equation over the direction of the dynamic phasor $\bar{X}_i$.

   - For a complex variable m_p, its projection over the dynamic phasor $\bar{X}_i$ is equal to $M_p^a \cos(M_p^\theta - X_i\theta)$.
   - For variables accompanied by the imaginary unit j, the projection is rotated 90 degrees. For example, the projection of jm_p over the dynamic phasor $\bar{X}_i$ is equal to $-M_p^a \sin(M_p^\theta - X_i^\theta)$.

5. Write the equation for the phase angle variable X_i^θ by finding the "tangential" component of every term on the right hand side of the equation (tangent to the dynamic phasor), scaled by the dynamic phasor's magnitude.

   - For a complex variable m_p, its tangential component to the dynamic phasor $\bar{X}_i$ is equal to $M_p^a \sin(M_p^\theta - X_i^\theta)$.
   - For variables accompanied by the imaginary unit j, the projection is rotated 90 degrees as well. For example, the tangent of jm_p to the dynamic phasor $\bar{X}_i$ is equal to $M_p^a \cos(M_p^\theta - X_i\theta)$.

6. Write similar equations for output variables if needed.

7. The resulting dynamic phasor model will have twice as many equations as the system expressed in complex variables.

The dynamic phasor model for the induction machine is shown in (7.6)–(7.9), whose left-hand sides will be called f_1 through f_4.

$$\frac{\mathrm{d}I_s^a}{\mathrm{d}t} = \frac{1}{L_sL_r - L_m^2}\left(L_rV_s^a\cos(V_s^\theta - I_s^\theta) - L_rr_sI_s^a + \omega_rL_mL_rI_r^a\sin(I_r^\theta - I_s^\theta)\right.$$
$$\left. + L_mr_rI_r^a\cos(I_r^\theta - I_s^\theta)\right) \tag{7.6}$$

$$\frac{\mathrm{d}I_s^\theta}{\mathrm{d}t} = \frac{1}{(L_sL_r - L_m^2)I_s^a}\left(L_rV_s^a\sin(V_s^\theta - I_s^\theta) - \omega_eL_rL_sI_s^a - \omega_rL_mL_rI_r^a\cos(I_r^\theta - I_s^\theta)\right.$$
$$\left. + L_mr_rI_r^a\sin(I_r^\theta - I_s^\theta) + (\omega_e - \omega_r)L_m^2I_s^a\right) \tag{7.7}$$

$$\frac{\mathrm{d}I_r^a}{\mathrm{d}t} = \frac{1}{L_sL_r - L_m^2}\left(-L_mV_s^a\cos(V_s^\theta - I_r^\theta) + L_mr_sI_s^a\cos(I_s^\theta - I_r^\theta)\right.$$
$$\left. - \omega_rL_mL_rI_s^a\sin(I_s^\theta - I_r^\theta) - L_sr_rI_r^a\right) \tag{7.8}$$

$$\frac{\mathrm{d}I_r^\theta}{\mathrm{d}t} = \frac{1}{(L_sL_r - L_m^2)I_r^a}\left(-L_mV_s^a\sin(V_s^\theta - I_r^\theta) + L_mr_sI_s^a\sin(I_s^\theta - I_r^\theta)\right.$$
$$\left. + \omega_rL_mL_rI_s^a\cos(I_s^\theta - I_r^\theta) + \omega_eL_m^2I_r^a - (\omega_e - \omega_r)L_sL_rI_r^a\right) \tag{7.9}$$

Besides the electrical differential equations, the connection of this model to the mechanical end is represented by the mechanical load balance equation. The dynamic equation that describes this interaction is:

$$\frac{\mathrm{d}\omega_r}{\mathrm{d}t} = \frac{P}{2J}(T_e - T_l) \tag{7.10}$$

where J is the inertia of the machine rotor and mechanical load combined; P is the number of poles, and T_e and T_l are the electrical and mechanical torques respectively. The left hand side of (7.10) is called f_5, completing a fifth order model for the induction machine.

The electrical torque T_e is given by

$$T_e = \frac{3}{2}\frac{P}{2}L_mI_s^aI_r^a\sin(I_s^\theta - I_r^\theta) \tag{7.11}$$

while the mechanical torque expression will depend on whatever load is coupled to the machine. At steady state, $T_e = T_l$.

7.1.2 Incremental phasor model for the induction machine

As it was done for the other non-linear models in state space representation, the *incremental phasor model* for the induction machine is obtained by linearizing the dynamic phasor model. By setting the time derivatives of (7.6)–(7.9) to zero, the sinusoidal steady state operating point could be found. The operating point has been omitted here, as it is the same one would find with traditional phasor algebra. At this operating point $\bar{x}$, it will be assumed that the rotor speed is known, i.e. $\omega_r|_{\bar{x}} = \omega_R$, a rotational speed in electrical radians per second. It will be assumed also that the synchronous speed is the dynamic phasor's system frequency, i.e. $\omega_e|_{\bar{x}} = \omega_o$.

In this linear model, the input, state and output vectors are:

$$x = \begin{pmatrix} I_s^a \\ I_s^\theta \\ I_r^a \\ I_r^\theta \\ \omega_r \end{pmatrix}, \quad u = \begin{pmatrix} V_s^a \\ V_s^\theta \\ T_l \end{pmatrix}, \quad y = \begin{pmatrix} I_s^a \\ I_s^\theta \\ \omega_r \end{pmatrix} \tag{7.12}$$

where superscripts $()^a$ and $()^\theta$ have the usual meaning of magnitude and phase angle components of the dynamic phasors for stator current I_s, rotor current I_r and stator voltage V_s.

The linearized model is shown term by term in Equations (7.13)–(7.21). For the resulting state matrix A, the stator-stator dynamics are given by

$$\begin{aligned} \frac{\partial f_1}{\partial I_s^a} &= \frac{L_r}{L_s L_r - L_m^2} r_s \\ \frac{\partial f_1}{\partial I_s^\theta} &= \left(\frac{L_m^2}{L_s L_r - L_m^2} \omega_R + \omega_o \right) I_s^A \\ \frac{\partial f_2}{\partial I_s^a} &= -\left(\frac{L_m^2}{L_s L_r - L_m^2} \omega_R + \omega_o \right) \frac{1}{I_s^A} \\ \frac{\partial f_2}{\partial I_s^\theta} &= \frac{L_r}{L_s L_r - L_m^2} r_s \end{aligned} \tag{7.13}$$

The rotor-rotor dynamics are given by

$$\begin{aligned}
\frac{\partial f_3}{\partial I_r^a} &= \frac{L_s}{L_s L_r - L_m^2} r_r \\
\frac{\partial f_3}{\partial I_r^\theta} &= \left(\omega_o - \frac{L_s L_r}{L_s L_r - L_m^2}\omega_R\right) I_r^A \\
\frac{\partial f_4}{\partial I_r^a} &= -\left(\omega_o - \frac{L_s L_r}{L_s L_r - L_m^2}\omega_R\right) \frac{1}{I_r^A} \\
\frac{\partial f_4}{\partial I_r^\theta} &= \frac{L_s}{L_s L_r - L_m^2} r_r
\end{aligned} \tag{7.14}$$

The stator-rotor dynamics are given by

$$\begin{aligned}
\frac{\partial f_1}{\partial I_r^a} &= \frac{1}{L_s L_r - L_m^2}\left(\omega_R L_m L_r \sin(I_r^\Theta - I_s^\Theta) + L_m r_r \cos(I_r^\Theta - I_s^\Theta)\right) \\
\frac{\partial f_1}{\partial I_r^\theta} &= \frac{I_r^A}{L_s L_r - L_m^2}\left(\omega_R L_m L_r \cos(I_r^\Theta - I_s^\Theta) - L_m r_r \sin(I_r^\Theta - I_s^\Theta)\right) \\
\frac{\partial f_2}{\partial I_r^a} &= \frac{1}{(L_s L_r - L_m^2) I_s^A}\left(-\omega_R L_m L_r \cos(I_r^\Theta - I_s^\Theta) + L_m r_r \sin(I_r^\Theta - I_s^\Theta)\right) \\
\frac{\partial f_2}{\partial I_r^\theta} &= \frac{I_r^A}{(L_s L_r - L_m^2) I_s^A}\left(\omega_R L_m L_r \sin(I_r^\Theta - I_s^\Theta) + L_m r_r \cos(I_r^\Theta - I_s^\Theta)\right)
\end{aligned} \tag{7.15}$$

And the rotor-stator dynamics are given by

$$\begin{aligned}
\frac{\partial f_3}{\partial I_s^a} &= \frac{1}{L_s L_r - L_m^2}\left(L_m r_s \cos(I_s^\Theta - I_r^\Theta) - \omega_R L_m L_s \sin(I_s^\Theta - I_r^\Theta)\right) \\
\frac{\partial f_3}{\partial I_s^\theta} &= \frac{I_s^A}{L_s L_r - L_m^2}\left(-L_m r_s \sin(I_s^\Theta - I_r^\Theta) - \omega_R L_m L_s \cos(I_s^\Theta - I_r^\Theta)\right) \\
\frac{\partial f_4}{\partial I_s^a} &= \frac{1}{(L_s L_r - L_m^2) I_r^A}\left(L_m r_s \sin(I_s^\Theta - I_r^\Theta) + \omega_R L_m L_s \cos(I_s^\Theta - I_r^\Theta)\right) \\
\frac{\partial f_4}{\partial I_s^\theta} &= \frac{I_s^A}{(L_s L_r - L_m^2) I_r^A}\left(L_m r_s \cos(I_s^\Theta - I_r^\Theta) - \omega_R L_m L_s \sin(I_s^\Theta - I_r^\Theta)\right)
\end{aligned} \tag{7.16}$$

The current-to-speed dynamics are given by

$$\begin{aligned}
\frac{\partial f_1}{\partial \omega_r} &= \frac{L_r}{L_s L_r - L_m^2} L_m I_r^A \sin(I_r^\Theta - I_s^\Theta) \\
\frac{\partial f_2}{\partial \omega_r} &= \frac{1}{(L_s L_r - L_m^2) I_s^A} \left(-L_m I_r^A \cos(I_r^\Theta - I_s^\Theta) - L_m^2 \right) \\
\frac{\partial f_3}{\partial \omega_r} &= \frac{-L_s}{L_s L_r - L_m^2} L_m I_s^A \sin(I_s^\Theta - I_r^\Theta) \\
\frac{\partial f_4}{\partial \omega_r} &= \frac{1}{(L_s L_r - L_m^2) I_r^A} \left(L_s L_m I_s^A \cos(I_s^\Theta - I_r^\Theta) + L_s L_r I_r^A \right)
\end{aligned} \tag{7.17}$$

while the dynamics of the speed with respect to the currents are given by

$$\begin{aligned}
\frac{\partial f_5}{\partial I_s^a} &= \frac{1}{M} \frac{3P}{4} L_m I_r^A \sin(I_s^\Theta - I_r^\Theta) \\
\frac{\partial f_5}{\partial I_s^\theta} &= \frac{1}{M} \frac{3P}{4} L_m I_s^A I_r^A \cos(I_s^\Theta - I_r^\Theta) \\
\frac{\partial f_5}{\partial I_r^a} &= \frac{1}{M} \frac{3P}{4} L_m I_s^A \sin(I_s^\Theta - I_r^\Theta) \\
\frac{\partial f_5}{\partial I_r^\theta} &= -\frac{1}{M} \frac{3P}{4} L_m I_s^A I_r^A \cos(I_s^\Theta - I_r^\Theta) \\
\frac{\partial f_5}{\partial \omega_r} &= 0
\end{aligned} \tag{7.18}$$

For the input, there are voltage-current dynamics given by

$$\begin{aligned}
\frac{\partial f_1}{\partial V_s^a} &= \frac{L_r}{L_s L_r - L_m^2} \cos(V_s^\Theta - I_s^\Theta) \\
\frac{\partial f_2}{\partial V_s^a} &= \frac{L_r}{(L_s L_r - L_m^2) I_s^A} \sin(V_s^\Theta - I_s^\Theta) \\
\frac{\partial f_3}{\partial V_s^a} &= \frac{L_m}{L_s L_r - L_m^2} \cos(V_s^\Theta - I_r^\Theta) \\
\frac{\partial f_4}{\partial V_s^a} &= \frac{L_m}{(L_s L_r - L_m^2) I_r^A} \sin(V_s^\Theta - I_r^\Theta) \\
\frac{\partial f_5}{\partial V_s^a} &= 0
\end{aligned} \tag{7.19}$$

for the voltage magnitude, and

$$\begin{aligned}
\frac{\partial f_1}{\partial V_s^\theta} &= \frac{-L_r}{L_s L_r - L_m^2} V_s^A \sin(V_s^\Theta - I_s^\Theta) \\
\frac{\partial f_2}{\partial V_s^\theta} &= \frac{L_r}{(L_s L_r - L_m^2) I_s^A} V_s^A \cos(V_s^\Theta - I_s^\Theta) \\
\frac{\partial f_3}{\partial V_s^\theta} &= \frac{L_m}{L_s L_r - L_m^2} V_s^A \cos(V_s^\Theta - I_r^\Theta) \\
\frac{\partial f_4}{\partial V_s^\theta} &= \frac{-L_m}{(L_s L_r - L_m^2) I_r^A} V_s^A \sin(V_s^\Theta - I_r^\Theta) \\
\frac{\partial f_5}{\partial V_s^\theta} &= 0
\end{aligned} \tag{7.20}$$

for the voltage angle. In addition, there are torque-current dynamics given by

$$\frac{\partial f_1}{\partial T_l} = \frac{\partial f_2}{\partial T_l} = \frac{\partial f_3}{\partial T_l} = \frac{\partial f_4}{\partial T_l} = 0 \qquad \frac{\partial f_5}{\partial T_l} = -\frac{1}{M} \tag{7.21}$$

For completeness purposes, we will consider, as an example, a simple mechanical load coupled to the induction machine shaft, with a load torque expression of the form

$$T_l = Q\omega_r^2 \tag{7.22}$$

which could represent a fan or centrifugal pump. Its linearized model is

$$\frac{\partial T_l}{\partial \omega_r} = 2Q\omega_R \tag{7.23}$$

which is a single gain linear model.

The resulting *incremental phasor model* for induction machine is presented in (7.26).

$$
\begin{aligned}
\dot{\tilde{x}} &= A\tilde{x} + B\tilde{u} \\
\tilde{y} &= C\tilde{x} + D\tilde{u}
\end{aligned}
$$

$$
A = \begin{pmatrix}
\frac{\partial f_1}{\partial I_s^a} & \frac{\partial f_1}{\partial I_s^\theta} & \frac{\partial f_1}{\partial I_r^a} & \frac{\partial f_1}{\partial I_r^\theta} & \frac{\partial f_1}{\partial \omega_r} \\
\frac{\partial f_2}{\partial I_s^a} & \frac{\partial f_2}{\partial I_s^\theta} & \frac{\partial f_2}{\partial I_r^a} & \frac{\partial f_2}{\partial I_r^\theta} & \frac{\partial f_2}{\partial \omega_r} \\
\frac{\partial f_3}{\partial I_s^a} & \frac{\partial f_3}{\partial I_s^\theta} & \frac{\partial f_3}{\partial I_r^a} & \frac{\partial f_3}{\partial I_r^\theta} & \frac{\partial f_3}{\partial \omega_r} \\
\frac{\partial f_4}{\partial I_s^a} & \frac{\partial f_4}{\partial I_s^\theta} & \frac{\partial f_4}{\partial I_r^a} & \frac{\partial f_4}{\partial I_r^\theta} & \frac{\partial f_4}{\partial \omega_r} \\
\frac{\partial f_5}{\partial I_s^a} & \frac{\partial f_5}{\partial I_s^\theta} & \frac{\partial f_5}{\partial I_r^a} & \frac{\partial f_5}{\partial I_r^\theta} & \frac{\partial f_5}{\partial \omega_r}
\end{pmatrix}
\qquad
B = \begin{pmatrix}
\frac{\partial f_1}{\partial V_s^a} & \frac{\partial f_1}{\partial V_s^\theta} & \frac{\partial f_1}{\partial T_l} \\
\frac{\partial f_2}{\partial V_s^a} & \frac{\partial f_2}{\partial V_s^\theta} & \frac{\partial f_2}{\partial T_l} \\
\frac{\partial f_3}{\partial V_s^a} & \frac{\partial f_3}{\partial V_s^\theta} & \frac{\partial f_3}{\partial T_l} \\
\frac{\partial f_4}{\partial V_s^a} & \frac{\partial f_4}{\partial V_s^\theta} & \frac{\partial f_4}{\partial T_l} \\
\frac{\partial f_5}{\partial V_s^a} & \frac{\partial f_5}{\partial V_s^\theta} & \frac{\partial f_5}{\partial T_l}
\end{pmatrix}
\tag{7.24}
$$

$$
C = \begin{pmatrix}
1 & 0 & 0 & 0 & 0 \\
0 & 1 & 0 & 0 & 0 \\
0 & 0 & 0 & 0 & 1
\end{pmatrix}
\qquad
D = 0
$$

$$
\tilde{T}_l = 2Q\omega_R\tilde{\omega}_r
$$

7.1.3 Constant-speed induction machine model

The incremental phasor model shown in (7.24) can be simplified if a constant speed operation (or equivalently, infinite inertia) is assumed.

Under this simplification, the fifth dynamic equation f_5 does not hold, and the torque input and speed output can be omitted. The input, state and output vectors are reduced as well:

$$
x = \begin{pmatrix} I_s^a \\ I_s^\theta \\ I_r^a \\ I_r^\theta \end{pmatrix}, \quad u = \begin{pmatrix} V_s^a \\ V_s^\theta \end{pmatrix}, \quad y = \begin{pmatrix} I_s^a \\ I_s^\theta \end{pmatrix} \tag{7.25}
$$

Th resulting *incremental phasor model* for the constant-speed induction machine is presented in (7.26).

$$
\begin{aligned}
\dot{\tilde{x}} &= A\tilde{x} + B\tilde{u} \\
\tilde{y} &= C\tilde{x} + D\tilde{u}
\end{aligned}
$$

$$
A = \begin{pmatrix}
\frac{\partial f_1}{\partial I_s^a} & \frac{\partial f_1}{\partial I_s^\theta} & \frac{\partial f_1}{\partial I_r^a} & \frac{\partial f_1}{\partial I_r^\theta} \\
\frac{\partial f_2}{\partial I_s^a} & \frac{\partial f_2}{\partial I_s^\theta} & \frac{\partial f_2}{\partial I_r^a} & \frac{\partial f_2}{\partial I_r^\theta} \\
\frac{\partial f_3}{\partial I_s^a} & \frac{\partial f_3}{\partial I_s^\theta} & \frac{\partial f_3}{\partial I_r^a} & \frac{\partial f_3}{\partial I_r^\theta} \\
\frac{\partial f_4}{\partial I_s^a} & \frac{\partial f_4}{\partial I_s^\theta} & \frac{\partial f_4}{\partial I_r^a} & \frac{\partial f_4}{\partial I_r^\theta}
\end{pmatrix}
\qquad
B = \begin{pmatrix}
\frac{\partial f_1}{\partial V_s^a} & \frac{\partial f_1}{\partial V_s^\theta} \\
\frac{\partial f_2}{\partial V_s^a} & \frac{\partial f_2}{\partial V_s^\theta} \\
\frac{\partial f_3}{\partial V_s^a} & \frac{\partial f_3}{\partial V_s^\theta} \\
\frac{\partial f_4}{\partial V_s^a} & \frac{\partial f_4}{\partial V_s^\theta}
\end{pmatrix}
\tag{7.26}
$$

$$
C = \begin{pmatrix} 1 & 0 & 0 & 0 \\ 0 & 1 & 0 & 0 \end{pmatrix}
\qquad
D = 0
$$

7.1.4 Numerical results

For the verification of the induction machine model, several numerical computations and time-domain simulations were carried out, using the parameters shown in Table 7.1.

Table 7.1: Base parameters for induction machine

Parameter	Symbol	Value	Units
System's frequency	f_o	60	Hz
System's angular frequency	ω_o	377	rad s^{-1}
Rated voltage	V_s^A	$460\sqrt{2}$	V
Rated power	P_r	74.6	kW
Number of poles	P	4	
Stator resistance	r_s	0.015	pu
Stator leakage inductance	L_{ls}	0.1	pu
Rotor resistance	r_r	0.015	pu
Rotor leakage inductance	L_{lr}	0.1	pu
Mutual inductance	L_m	3.0	pu
Rated slip	s_R	1.77	%
Mechanical constant	M	2	s

The induction machine was studied when the mechanical load is present, and the constant speed case as well. In both cases, the machine was connected to an

ideal voltage bus, hence the impedance based stability criteria cannot be applied due to the lack of impedance in the ideal voltage bus.

By using the parameters of Table 7.1, and varying the rotor slip from 0.1% to 50%, the machine's torque curve of Figure 7.2 is obtained.

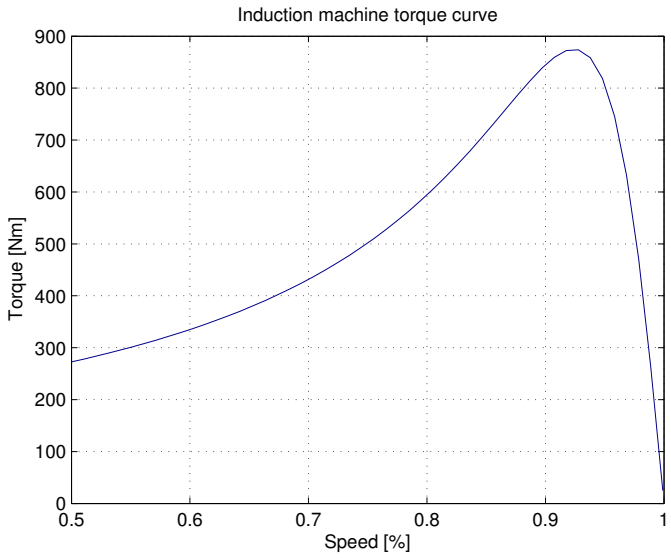

Figure 7.2: Torque curve for the constant-speed induction machine

Constant speed induction machine

Using the model (7.26), an eigenvalue analysis was performed. The eigenvalues were studied for several operating points, by changing the rotor slip while maintaining the other parameters. The results are presented in Figure 7.3. It can be recognized in this plot the location of the stator poles (far from the real axis, mostly unaffected) and the rotor poles (closer to the real axis, larger vertical movement). The constant speed eigenvalues found by the incremental phasor model are in fact the same as the ones described in [99, Sec. 4.8]. The operation of the machine, in all these cases, is stable.

For the set of operating points obtained in the eigenvalue analysis, the *incremental phasor admittance* was obtained numerically. It is presented as a set of Bode plots in

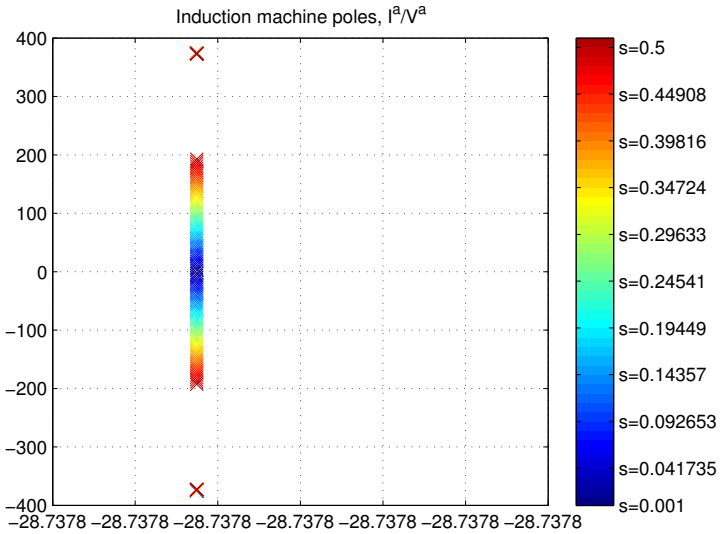

Figure 7.3: Root locus for the constant-speed induction machine

Figure 7.4.

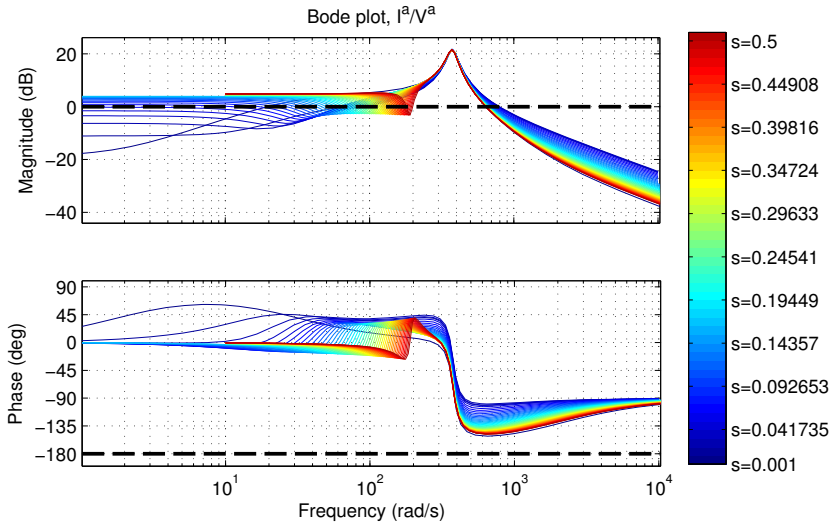

Figure 7.4: Admittance bode plots for the constant-speed induction machine

Induction machine coupled to a mechanical load

The same eigenvalue analysis is performed for the full induction machine model (7.24), but this time keeping a fixed operating point (rated slip) and changing the machine's mechanical constant M (proportional to the inertia). The results are presented in Figure 7.5 for a range of 1% to 200% of the nominal inertia. This is remarkably different than the previous case, as the dynamics of the extra state play along with the existing poles in a very special way. It can be seen in the figure how the single real pole moves towards the origin as the inertia increases, while the pair of rotor poles moves towards, and then away from the imaginary axis. The stator poles are only slightly affected by the inertia change.

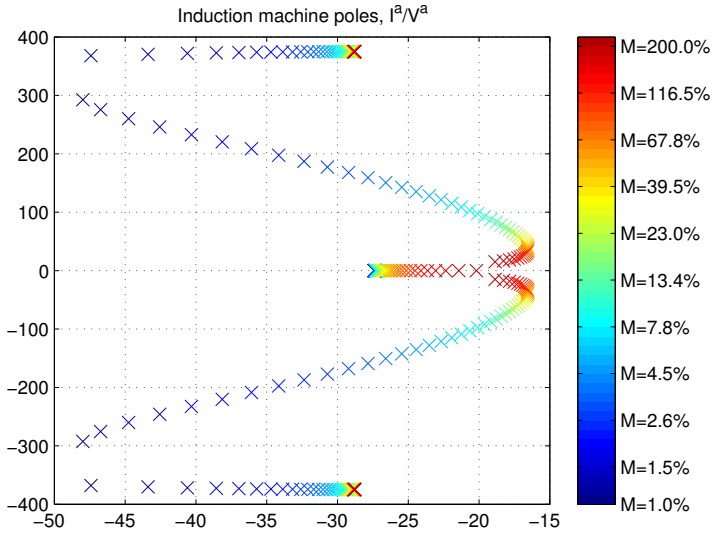

Figure 7.5: Root locus for the induction machine coupled to a mechanical load

The corresponding *incremental phasor admittances* for these cases are shown in Figure 7.6. One of the main differences from the constant-speed admittances shown in 7.4 is that the machine presents a "negative impedance" effect for injections of low frequency. Nevertheless, the machine is stable for all operating conditions.

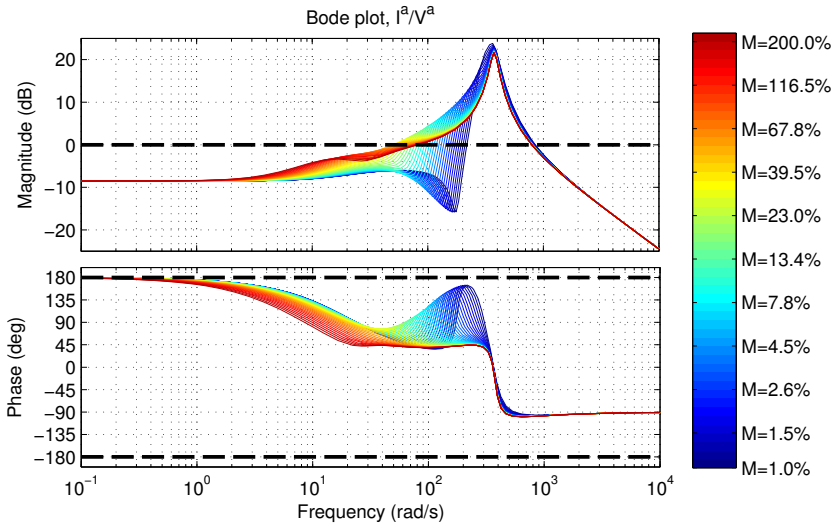

Figure 7.6: Admittance bode plots for the induction machine coupled to a mechanical load

7.1.5 Time-domain simulations

In order to verify the results obtained by the analytical model, a time-domain simulation model was built in Matlab/Simulink using the SimPowerSystems blockset. The full-featured model of the induction machine, presented in Figure 7.7, is connected to a microsource with droop control gain $M_p = 0.1\%$. The rotor is short-circuited, and the full model of mechanical load is included, as shown in Figure 7.8.

During the simulation, the microsource suffers a droop gain step. At time $t = 1.0\,\text{s}$, M_p increases from 0.1% to 5%. The currents, rotor speed and system's frequency are presented in Figure 7.9. It can be seen in the figure how the rotor speed decreases after the frequency of the system is reduced by the changes in the droop gain. Even though there are some oscillations in the frequency signal, the system does not enter into an unstable operation.

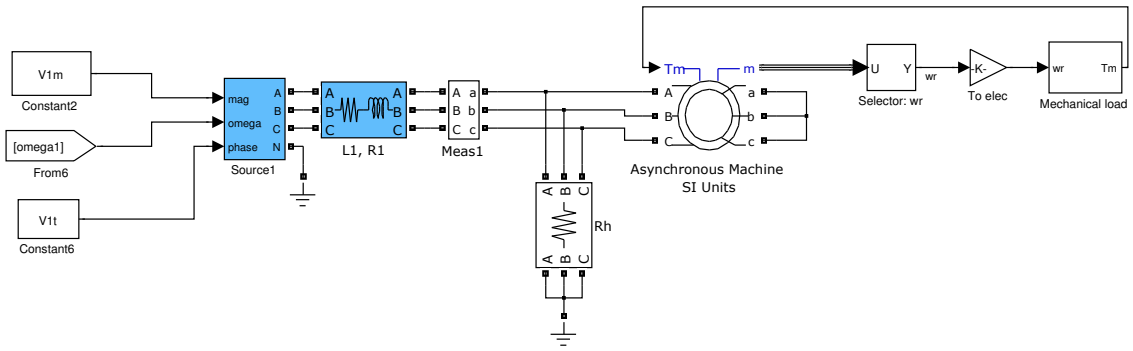

Figure 7.7: Induction machine simulation block diagram

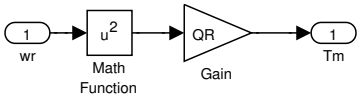

Figure 7.8: Mechanical load simulation block diagram

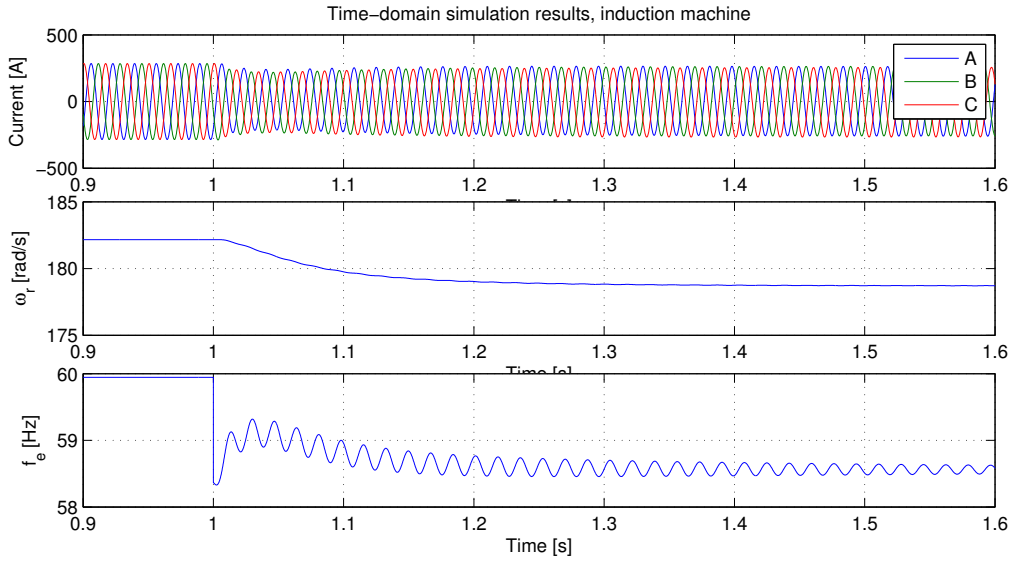

Figure 7.9: Time-domain simulation results for induction machine. At $t = 1.0\,\mathrm{s}$, the droop gain of the microsource is increased.

7.2 Ideal P-Q load

7.2.1 P-Q load model

A P-Q load is a very particular component of the system, which is usually intended to represent a load with a "negative resistance" behavior. Following the voltage and current designations of Figure 7.10, the expression for the apparent power S of the load can be written as

$$\frac{1}{2}\bar{V}_L \cdot \bar{I}_L^* = P + jQ = S \tag{7.27}$$

where P and Q are the active and reactive power components respectively, and * denotes the complex conjugate. From this equation, the real and imaginary components can be separated as

$$\begin{aligned} V_L^a I_L^a \cos(V_L^\theta - I_L^\theta) &= 2P \\ V_L^a I_L^a \sin(V_L^\theta - I_L^\theta) &= 2Q \end{aligned} \tag{7.28}$$

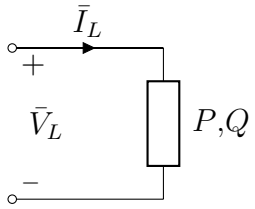

Figure 7.10: Schematic of a P-Q load

If it is desired to express the relationship between currents and voltages as an impedance, then the voltage magnitude and angle could be written as

$$\begin{aligned} V_L^a &= \frac{2S}{I_L^a} \\ V_L^\theta &= I_L^\theta + \arctan\left(\frac{Q}{P}\right) \end{aligned} \tag{7.29}$$

The state space representation of this P-Q load will have output and input variables

$$y = \begin{pmatrix} V_L^a \\ V_L^\theta \end{pmatrix}, \text{and} \quad u = \begin{pmatrix} I_L^a \\ I_L^\theta \end{pmatrix} \tag{7.30}$$

respectively. Since there are no dynamics on the system (as in the resistive load case), the matrix representation will only include a single gain matrix D. The components of such matrix are obtained in (7.31).

$$\begin{aligned} \frac{\partial V_L^a}{\partial I_L^a} &= -\frac{V_L^A}{I_L^A} \\ \frac{\partial V_L^a}{\partial I_L^\theta} &= 0 \\ \frac{\partial V_L^\theta}{\partial I_L^a} &= 0 \\ \frac{\partial V_L^\theta}{\partial I_L^\theta} &= 1 \end{aligned} \tag{7.31}$$

The linearized state space representation of the P-Q load is then presented in (7.32). Note how the gain matrix effectively shows the "negative resistance" effect in the magnitude/magnitude channel.

$$\tilde{y} = \begin{pmatrix} -\frac{V_L^A}{I_L^A} & 0 \\ 0 & 1 \end{pmatrix} \tilde{u} \tag{7.32}$$

7.2.2 Simulation models

There exist many models for P-Q loads, called for example constant-power loads in [4, Ch. 7]. Two models are introduced below.

Dynamic load SimPowerSystems block

The SimPowerSystems blockset include a dynamic load, that can be programmed for constant power, and is shown in Figure 7.11. The inputs to this block are the constant power setpoints PL and QL.

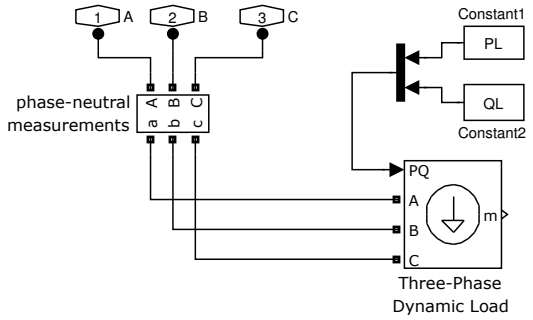

Figure 7.11: P-Q load block diagram, Dynamic load case

Current-source based custom load

Due to the lack of controllability of the SimPowerSystems Dynamic load block, another P-Q load model was developed, based on a current source, as shown in Figure 7.12.

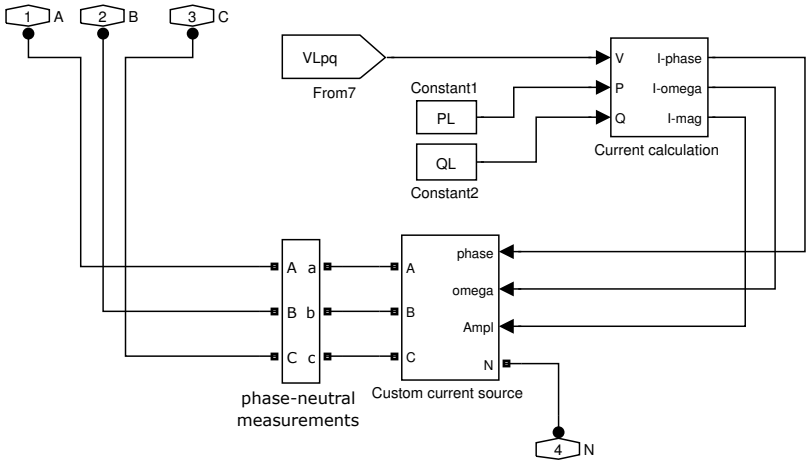

Figure 7.12: P-Q load block diagram, Current-source load case

The power setpoints are converted to current references that are fed into an ideal current source, which is similar to Figure 3.19, except that the controlled voltage sources are replaced by controlled current sources. The current references are generated by dividing the voltage by the apparent power, as shown in Figure

7.13. The voltage of phase one is used as reference for the frequency computation by a PLL; the voltage magnitude is calculated as the magnitude of the positive sequence voltage; the saturation block avoids infinite currents during the beginning of the simulation and transients of extreme low voltage; the delayed switch avoids noisy phase angles at the beginning of the simulation; the current magnitude and phase angles are simply calculated as:

$$|I| = \frac{2|S|}{|V|} \tag{7.33}$$

$$\angle I = \angle V - \angle S \tag{7.34}$$

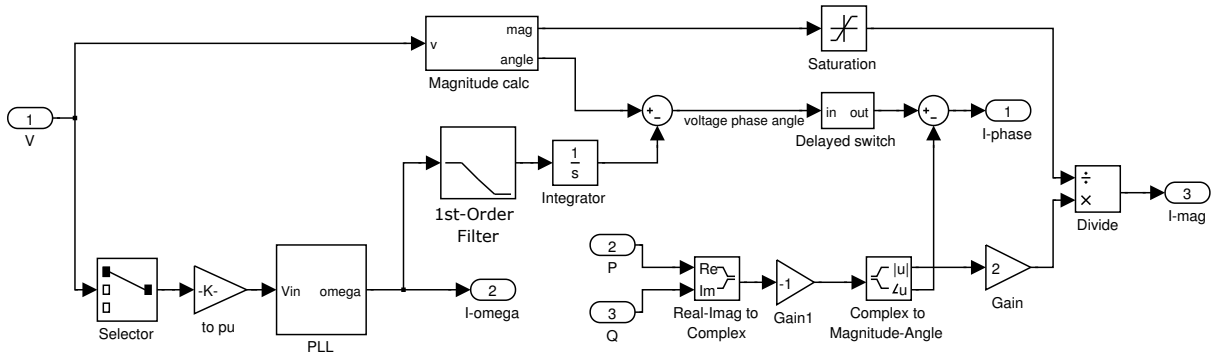

Figure 7.13: P-Q load block diagram, Current-source load case, control blocks

7.2.3 Time-domain simulation results

The current-source based custom load model was connected to a microsource model, and a simulation was performed in Matlab/Simulink. The time-domain simulations in general do not converge with this load model, and only certain operating points appear to work well. For example, a stable case is presented in Figure 7.14, where the P-Q load is perturbed at time $t = 1.0\,\mathrm{s}$ by increasing its demanded power by 10%.

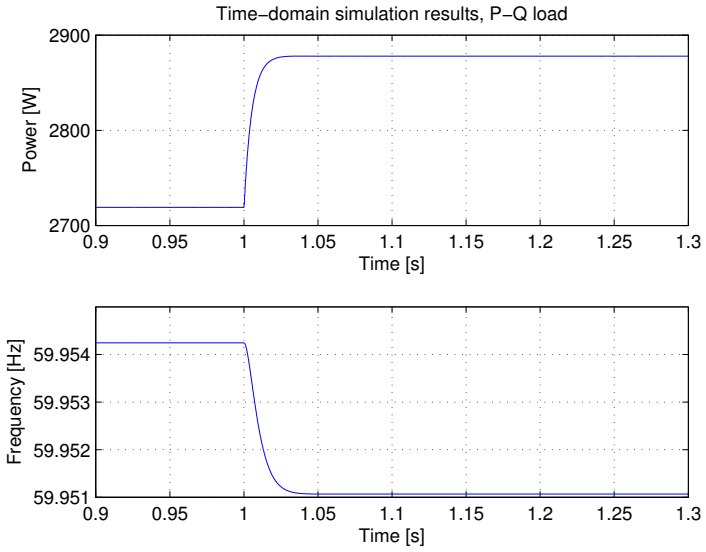

Figure 7.14: Time-domain simulation results for one microsource, P-Q load system. At time $t = 1.0\,\mathrm{s}$ the P-Q load is perturbed.

7.3 Summary

In this chapter, the dynamic phasor model of two kinds of complex loads are developed: the induction machine and the constant power P-Q load. Both kinds of loads are common in a broad range of applications, including microgrids.

The induction machine model was derived by the synchronous reference frame d-q model, by an algorithmic approach. This model was further simplified for the constant speed case, which served as a point of comparison with constant speed models found in the literature. The full induction machine model was coupled to a basic mechanical load, and an eigenvalue analysis was carried out while modifying the machine's inertia. The induction machine was stable at all times. A full featured model of the induction machine was used along with a microsource for time-domain simulations. Even though an stability analysis was not performed on a model considering both the machine and the microsource, the simulations gave stable results even after modest droop gain steps.

The P-Q load model is developed from the active and reactive power equations of an ideal P-Q load. Even though this model is perfectly analyzable from the theoretical point of view, it is, at this stage, of no interesting use, as the results for any operating condition of a P-Q load along with a microsource are unstable. However, two practical P-Q load model approximations were presented. One of the models was used in time-domain simulation, giving stable results.

While developing the model for the induction machine, a set of steps were stated, by which one could obtain a dynamic phasor model derived from a d-q model. This general approach, which is equivalent to transforming the equations into polar coordinates (rather than rectangular as the d-q model case), could be applied to other d-q models expressed as complex variable differential equation sets. However, it is worth mentioning that the complex variable model (or d-q model) must be expressed (or translated otherwise) into the synchronous reference frame, whose rotating frequency is the desired dynamic phasor rotating frequency ω_o.

8 CONCLUSIONS AND FUTURE WORK

In this thesis, the impedance matching stability criteria for AC microgrids is presented. The stability criteria is compatible with *plug and play* features expected from a microgrid: it is applied at the point of connection between the existing microgrid and a new unit that is being incorporated into the system.

Chapter 2 presented a detailed literature review. It was identified that existing tools for stability studies are not particularly scalable for a microgrid with plug and play capabilities. Furthermore, an approach using the concept of impedance matching is applicable in the microgrid case was identified for the purpose.

The ideas behind the impedance matching stability criteria were presented in Chapter 3, along with the proposed dynamic phasor analytical model of a microgrid. These nonlinear models are linearized around an operating point, producing the *incremental phasor dynamic models*, from which the *incremental phasor impedances* are obtained. These impedances are ultimately used with the impedance matching stability criteria.

In Chapter 4, single source microgrids were studied from the analytical, numerical and simulation point of view. Two single source cases were studied: the *single microsource coupled to an infinite bus* was used to validate the dynamic phasor and incremental phasor models against the results published in literature; and the *single microsource coupled to a load* was used to validate the models against time-domain simulations. An interesting results is that a single microsource connected to a resistive or R-L load is always stable.

In Chapter 5, the stability of two source microgrids was studied. The stability properties were established using the impedance matching stability criteria. The incremental phasor models are also validated against time-domain simulations. In addition, a measurement of the incremental phasor impedance was carried out: the incremental phasor impedances and admittances were successfully obtained, and closely match the results obtained with the analytical model.

Chapter 6 presented experimental results that validate the incremental phasor

impedance approach and demonstrated the utility of the impedance based stability criterion with actual laboratory examples.

In Chapter 7, additional model for two kinds of complex loads were introduced. The induction machine and the constant power (P-Q) load were introduced, numerically studied and simulated. These models, although not contrasted with experimental counterparts, serve as an starting point for studying more complex, real-world loads.

An outline and description of the contributions from this work are presented in the following section.

8.1 Contributions

- *Identification of the problem, the opportunity and the solution*: The review of the state of the art in the microgrid topics covered several areas that are the current subject of research, as well as others that are more mature. It was recognized that there are existing tools suitable for stability studies in a microgrid system. However, the *plug and play* concept introduces new challenges that require a novel approach. A new way of looking at the microgrid was presented, and the methodology of impedance matching stability criteria to microgrids for the stability assessment of a microgrid has been identified for developing this work.

- *Dynamic phasor model formulation*: Even though there are several approaches to the determination of the small signal models and impedances, they fail when applied to systems with the characteristics of a microgrid. For example, the most popular technique, using d-q reference frame, may not be readily suitable for a system with variable frequency that is regulated by the droop controller. The dynamic phasor modeling technique in polar coordinates is, in contrast, a powerful tool suitable for systems with such characteristics.

- *Incremental phasor models and impedances*: While dynamic phasor models for microgrid components may be readily created, they express nonlinear de-

pendence. A linearized model around an operating point, called *incremental phasor model*, was then developed for the stability studies. From these models the *incremental phasor impedance* is extracted as a single component of the incremental phasor model's transfer function. From the incremental model, impedance is useful for the determination of the stability properties of a microgrid, because it can be determined at the point of connection, making this approach compatible with the *plug and play* concept.

- *Verification of incremental impedance transfer functions using simulation*: The analytically predicted incremental phasor impedance transfer functions have been successfully validated by simulation. A frequency domain sweep was conducted on the complete system, followed by Fourier analysis to determine the incremental phasor impedances, and compared against the analytical solutions.

- *Use of incremental phasor models to establish stability properties*: The incremental phasor dynamic transfer function model has been validated in a particular case by studying systems comprising a single microsource connected to the infinite bus, and have validated and strengthened previously developed stability criteria in a more rigorous and general manner.

- *Impedance matching stability criteria*: The incremental phasor impedances forming a loop gain transfer function to study the stability of a microgrid has been proposed. Such an approach using incremental phasor impedances is suitable for a system where we only have access the point of connection, such as a microsource that is being connected to an existing microgrid (with possibly unknown properties).

- *Verification of proposed stability criteria by simulation*: The criterion has been successfully validated by simulation: the models predicted instabilities for frequency droop gains above certain critical values, which were verified by time-domain simulations. Systems comprising a single microsource con-

nected to the infinite bus, a single microsource connected to a load, and a two-microsource microgrid were modeled and validated.

- *Validation of incremental impedance transfer functions by experimentation*: The incremental phasor impedances of several components were measured by experiments on a laboratory microgrid installation. Passive loads and microsources were successfully measured, and closely match their analytical models.

- *Validation of the impedance matching stability criteria by experimentation*: Stability margins for the microgrid were identified by using the incremental phasor models. By driving the microgrid into instability, these margins were confirmed. Corrective actions based on the model estimations can be applied to a microgrid in order to avoid unstable operation.

- *Incremental phasor model for complex loads*: In addition to the models covered in Chapter 3, two complex loads were modeled using dynamic phasors.

  The induction machine's dynamic phasor model was derived from the traditional d-q model. Then, the incremental phasor model was obtained and an eigenvalue analysis was performed in two cases: an induction machine coupled to a finite-inertia mechanical load, and a constant-speed (infinite inertia) induction machine. The results obtained from the eigenvalue analysis match those found in the literature.

  The constant-power (P-Q) load was modeled as an ideal negative-resistance load. Even though this model has not encountered practical use, two simulation models are proposed. One of the models is successfully used in time-domain simulations.

- *Derivation of dynamic phasor model from d-q model*: By expressing a model in complex variables in the synchronous reference frame, the derivation of the dynamic phasor model is direct. An algorithm was presented in Section 7.1. This algorithm was used to obtain the dynamic phasor model for the

induction machine, and could be used to obtain models for other systems as well.

8.2 Future work

- *Improvement of the dynamic phasor analytical models*: Even though the models presented in this thesis proved useful in determining stability properties of a microgrid, there are some assumptions and simplifications that should be relaxed. In particular, the dynamic phasor models developed in Chapter 3 do not include the reactive power droop control, counterpart to the power-frequency droop control. The reactive power-voltage (Q-V) droop control is a key component of microgrid controls, that provides controlled reactive power sharing among the microsources.

  Other improvements could be achieved by not neglecting the magnetizing inductance of the transformers; by incorporating saturation on magnetic circuits present in the microgrid; and by modeling voltage and current unbalances through the incorporation of a zero sequence component.

  One of the features that characterizes the UW Microgrid controllers is the maximum and minimum power limit (Pmax and Pmin) control. These controllers are incorporated along with the frequency droop gain; there is a potential of incorporating them in the dynamic phasor models as well, by little modification to the analytical models developed in this document.

- *Improvement of the measurement techniques*: One of the weaknesses of the experimental hardware setup was the inability to reproduce clean incremental phasor impedance spectra. This is due to several factors, including: (a) the capacity of the small signal injection unit to create the perturbations into the system; (b) the tendency of the system (specially of an islanded microgrid) to change its operating point while injecting a small signal perturbation; and (c) the dynamic range of the injected and measured signals, which can be several tens of dB.

Even though an independent small signal injection unit could be further improved by considering the factors above, it is desirable to incorporate these impedance measurement algorithms into the microgrid components themselves. For example, a true *plug and play* unit should be able to inspect its PoC and obtain the impedance of the system being connected to. At the same time, it should be able to adjust its own incremental phasor impedance to ensure a stable operation after the interconnection is done.

One of the key units that might be suitable for doing the impedance measurement task is the static switch. Being this unit usually located at the point of connection with the utility grid, the static switch could *sense* the state of the rest of the grid before synchronizing the two grids, and monitor the state of the parallel system while they are interconnected.

- *Extension of the impedance matching based stability criteria to other environments*: The stability criteria presented in this document was inspired by the *plug and play* capabilities that one would expect from a microgrid. However, the microgrid, as well as any other EPS, could be analyzed using the impedance matching based stability criteria presented in this document. Developed with scalability in mind, the impedance matching offers the possibility of studying the stability of a system from several interconnection points. Problems such as the incorporation of new units, inter-area oscillations, loss of synchronism, among other, may be approached by selecting the right PoC. If needed, the models could be extended to include input, state, and output variables more familiar with EPS stability literature, such as voltage magnitudes, angles, active power and frequency deviations.

- *Connection between dynamic phasor models and secondary and tertiary control*: EPS area controllers and system operators work together to provide the best power quality possible in an electricity grid. One of the most common tasks is to provide primary, secondary and tertiary control, which are applied in different time domains, from the milliseconds to several minutes or hours. The system's frequency present natural deviations, resulting from changes into

the operating conditions of the grid, some times programmed, other times incidental. Therefore it is a task of the controller to maintain the system's frequency near its nominal value.

Even though primary controllers, such as the droop control covered in this thesis, already provide means of balancing the power demand and system's frequency, they encounter long-term frequency deviation, steady state error that has to be minimized. The existence of secondary and tertiary controls are due to this frequency deviations.

The dynamic phasor modeling presents an interesting framework, which defines a constant, known frequency, and takes into account all deviations from such frequency. Minimizing long-term frequency deviations could be seen as the problem of minimizing phase angle error in a dynamic phasor reference frame.

It might be interesting to study the relationship between the actions taken in droop controllers (droop gain dispatch) and the steady state frequency error. Microgrid centralized controllers usually have the task of balancing the power flow such that the steady state error is minimized. By using dynamic phasor models, the power-frequency controllers could be consolidated in a model that would predict system's frequency deviations, and could be of practical use not only for microgrids but also other EPS.

- *Communication interfaces:* In order for a microgrid centralized controller to dispatch setpoints and collect measurement data, a communication channel must exist among the units. The UW Microgrid, for example, has an IEEE 802.11b wireless communication system for monitoring and control purposes. When developing the dynamic phasor models, no communication channel was modeled into the system, and delivery of setpoints was assumed instantaneous and ideal. Communication channel models exist for wired and wireless cases, which take into account loss of information, latency, jitter, among other issues.

There exists a recognized challenge in integrating dynamics of the electromagnetic domain (usually in the order of milliseconds to seconds) with power electronics domain (usually in the order of microseconds). The challenge is extended when including communication dynamics that, depending on the channel model, could add dynamic on a third domain, at a much larger timescale. Nevertheless, the dynamic phasor models were successfully used for analytical and simulation studies when different dynamics timescales are present. An attractive addition to the dynamic phasor models would be the interactions between the primary controllers (e.g. power-frequency droop gains) and their dispatchable setpoints through a communication channel.

8.3 Summary

The impedance matching stability criteria presented in this thesis is an suitable tool for a microgrid environment where the *plug and play* capabilities are of major importance. The stability criteria were exemplified with several microgrid scenarios that were used to validate the dynamic phasor and incremental phasor modeling approach. The impedance matching stability criteria successfully predicted instabilities on microgrids with one- and two-microsources. As the impedance matching is done at the point of connection, the criteria is easily extended for the multi-microsource case. The experimental work included hardware validation, establishment of stability margins in a microgrid context, and the extension to more complex loads. At the conclusion of this work, a novel and definitive framework for studying the stability of microgrids is presented, for expanding their role in the emerging future.

BIBLIOGRAPHY

[1] L. Che, M. Khodayar, and M. Shahidehpour, "Only connect: Microgrids for distribution system restoration," *Power and Energy Magazine, IEEE*, vol. 12, no. 1, pp. 70–81, 2014.

[2] S. Liu, Y. Hou, C. Liu, and R. Podmore, "The healing touch: Tools and challenges for smart grid restoration," *Power and Energy Magazine, IEEE*, vol. 12, no. 1, pp. 54–63, 2014.

[3] N. Abi-Samra and W. Henry, "Actions before... and after a flood," *Power and Energy Magazine, IEEE*, vol. 9, no. 2, pp. 52–58, 2011.

[4] P. Kundur, N. Balu, and M. Lauby, *Power system stability and control*, ser. EPRI power system engineering series. McGraw-Hill, 1994.

[5] M. Vidyasagar, *Nonlinear Systems Analysis*, ser. Classics in applied mathematics. Society for Industrial and Applied Mathematics, 2002.

[6] C.-T. Chen, *Linear System Theory and Design*, 3rd ed. New York, NY, USA: Oxford University Press, Inc., 1998.

[7] M. Gardner and J. Barnes, *Transients in linear systems studied by the Laplace transformation*, ser. Transients in Linear Systems Studied by the Laplace Transformation. J. Wiley & Sons, inc., 1956, no. v. 1.

[8] R. Middlebrook, "The general feedback theorem: a final solution for feedback systems," *Microwave Magazine, IEEE*, vol. 7, no. 2, pp. 50–63, 2006.

[9] M. Tian, V. Visvanathan, J. Hantgan, and K. Kundert, "Striving for small-signal stability," *Circuits and Devices Magazine, IEEE*, vol. 17, no. 1, pp. 31–41, 2001.

[10] H. Bode, "Obituary statement: Harry nyquist," *Automatic Control, IEEE Transactions on*, vol. 22, no. 6, pp. 897–898, 1977.

[11] M. Van Valkenburg, "In memoriam: Hendrik w. bode (1905-1982)," *Automatic Control, IEEE Transactions on*, vol. 29, no. 3, pp. 193–194, 1984.

[12] A. G. J. MacFarlane and I. Postlethwaite, "The generalized nyquist stability criterion and multivariable root loci," *International Journal of Control*, vol. 25, no. 1, pp. 81–127, 1977. [Online]. Available: http://www.tandfonline.com/doi/abs/10.1080/00207177708922217

[13] G. AlLee and W. Tschudi, "Edison redux: 380 vdc brings reliability and efficiency to sustainable data centers," *Power and Energy Magazine, IEEE*, vol. 10, no. 6, pp. 50–59, 2012.

[14] B. Patterson, "Dc, come home: Dc microgrids and the birth of the "enernet"," *Power and Energy Magazine, IEEE*, vol. 10, no. 6, pp. 60–69, 2012.

[15] A. Riccobono and E. Santi, "Comprehensive review of stability criteria for dc distribution systems," in *Energy Conversion Congress and Exposition (ECCE), 2012 IEEE*, 2012, pp. 3917–3925.

[16] M. Belkhayat, R. Cooley, and E. Abed, "Stability and dynamics of power systems with regulated converters," in *Circuits and Systems, 1995. ISCAS '95., 1995 IEEE International Symposium on*, vol. 1, 1995, pp. 143–145 vol.1.

[17] M. Belkhayat, R. Cooley, and A. Witulski, "Large signal stability criteria for distributed systems with constant power loads," in *Power Electronics Specialists Conference, 1995. PESC '95 Record., 26th Annual IEEE*, vol. 2, 1995, pp. 1333–1338 vol.2.

[18] S. Sudhoff, K. Corzine, S. Glover, H. Hegner, and J. Robey, H. N., "Dc link stabilized field oriented control of electric propulsion systems," *Energy Conversion, IEEE Transactions on*, vol. 13, no. 1, pp. 27–33, 1998.

[19] S. Sudhoff, S. Glover, P. Lamm, D. H. Schmucker, and D. Delisle, "Admittance space stability analysis of power electronic systems," *Aerospace and Electronic Systems, IEEE Transactions on*, vol. 36, no. 3, pp. 965–973, 2000.

[20] S. Sudhoff and J. Crider, "Advancements in generalized immittance based stability analysis of dc power electronics based distribution systems," in *Electric Ship Technologies Symposium (ESTS), 2011 IEEE*, 2011, pp. 207–212.

[21] G. S. Thandi, R. Zhang, K. Xing, F. Lee, and D. Boroyevich, "Modeling, control and stability analysis of a pebb based dc dps," *Power Delivery, IEEE Transactions on*, vol. 14, no. 2, pp. 497–505, 1999.

[22] F. Lee, M. Xu, S. Wang, and B. Lu, "Design challenges for distributed power systems," in *Power Electronics and Motion Control Conference, 2006. IPEMC 2006. CES/IEEE 5th International*, vol. 1, 2006, pp. 1–15.

[23] X. Wang, J. M. Guerrero, F. Blaabjerg, and Z. Chen, "A review of power electronics based microgrids," *Journal of Power Electronics*, vol. 12, no. 1, pp. 181–192, 2012.

[24] J. Guerrero, M. Chandorkar, T. Lee, and P. Loh, "Advanced control architectures for intelligent microgrids – part i: Decentralized and hierarchical control," *Industrial Electronics, IEEE Transactions on*, vol. 60, no. 4, pp. 1254–1262, 2013.

[25] J. Guerrero, P. C. Loh, T.-L. Lee, and M. Chandorkar, "Advanced control architectures for intelligent microgrids – part ii: Power quality, energy storage, and ac/dc microgrids," *Industrial Electronics, IEEE Transactions on*, vol. 60, no. 4, pp. 1263–1270, 2013.

[26] A. Dobakhshari, S. Azizi, and A. Ranjbar, "Control of microgrids: Aspects and prospects," in *Networking, Sensing and Control (ICNSC), 2011 IEEE International Conference on*, 2011, pp. 38–43.

[27] F. Saccomanno, *Electric power systems: analysis and control*, ser. IEEE Press series on power engineering. IEEE Press, 2003.

[28] M. Chandorkar, D. Divan, and R. Adapa, "Control of parallel connected inverters in standalone ac supply systems," *Industry Applications, IEEE Transactions on*, vol. 29, no. 1, pp. 136–143, 1993.

[29] S. Iyer, M. Belur, and M. Chandorkar, "Decentralized control of a line interactive uninterruptible power supply (ups)," in *American Control Conference (ACC), 2010*, 2010, pp. 3293–3298.

[30] R. Lasseter, "Microgrids," in *Power Engineering Society Winter Meeting, 2002. IEEE*, vol. 1, 2002, pp. 305–308 vol.1.

[31] P. Piagi and R. Lasseter, "Autonomous control of microgrids," in *Power Engineering Society General Meeting, 2006. IEEE*, 2006, pp. 8 pp.–.

[32] M. S. Illindala, "Vector control of pwm vsi based distributed resources in a microgrid," Ph.D. dissertation, University of Wisconsin-Madison, 2005.

[33] P. Piagi, "Microgrid control," Ph.D. dissertation, University of Wisconsin-Madison, 2005.

[34] J. A. P. Lopes, A. G. Madureira, and C. C. L. M. Moreira, "A view of microgrids," *Wiley Interdisciplinary Reviews: Energy and Environment*, vol. 2, no. 1, pp. 86–103, 2013. [Online]. Available: http://dx.doi.org/10.1002/wene.34

[35] K. De Brabandere, B. Bolsens, J. Van Den Keybus, J. Driesen, M. Prodanovic, and R. Belmans, "Small-signal stability of grids with distributed low-inertia generators taking into account line phasor dynamics," in *Electricity Distribution, 2005. CIRED 2005. 18th International Conference and Exhibition on*, 2005, pp. 1–5.

[36] X. Wang, F. Zhuo, H. Guo, L. Meng, M. Yang, and J. Liu, "Stability analysis of droop control for inverter using dynamic phasors method," in *Energy Conversion Congress and Exposition (ECCE), 2011 IEEE*, 2011, pp. 739–742.

[37] E. Coelho, P. Cortizo, and P. Garcia, "Small-signal stability for parallel-connected inverters in stand-alone ac supply systems," *Industry Applications, IEEE Transactions on*, vol. 38, no. 2, pp. 533–542, 2002.

[38] N. Pogaku, M. Prodanovic, and T. Green, "Modeling, analysis and testing of autonomous operation of an inverter-based microgrid," *Power Electronics, IEEE Transactions on*, vol. 22, no. 2, pp. 613–625, 2007.

[39] R. Majumder, A. Ghosh, G. Ledwich, and F. Zare, "Stability analysis and control of multiple converter based autonomous microgrid," in *Control and Automation, 2009. ICCA 2009. IEEE International Conference on*, 2009, pp. 1663–1668.

[40] S. Iyer, M. Belur, and M. Chandorkar, "A generalized computational method to determine stability of a multi-inverter microgrid," *Power Electronics, IEEE Transactions on*, vol. 25, no. 9, pp. 2420–2432, 2010.

[41] G. Venkataramanan and M. Illindala, "Small signal dynamics of inverter interfaced distributed generation in a chain-microgrid," in *Power Engineering Society General Meeting, 2007. IEEE*, 2007, pp. 1–6.

[42] T. Green and M. ProdanoviÄĞ, "Control of inverter-based micro-grids," *Electric Power Systems Research*, vol. 77, no. 9, pp. 1204 – 1213, 2007, ¡ce:title¿Distributed Generation¡/ce:title¿. [Online]. Available: http://www.sciencedirect.com/science/article/pii/S037877960600191X

[43] R. Majumder, A. Ghosh, G. Ledwich, and F. Zare, "Operation and control of hybrid microgrid with angle droop controller," in *TENCON 2010 - 2010 IEEE Region 10 Conference*, 2010, pp. 509–515.

[44] R. Majumder, B. Chaudhuri, A. Ghosh, R. Majumder, G. Ledwich, and F. Zare, "Improvement of stability and load sharing in an autonomous microgrid using supplementary droop control loop," *Power Systems, IEEE Transactions on*, vol. 25, no. 2, pp. 796–808, 2010.

[45] R. Majumder, A. Ghosh, G. Ledwich, and F. Zare, "Power sharing and stability enhancement of an autonomous microgrid with inertial and non-inertial dgs with dstatcom," in *Power Systems, 2009. ICPS '09. International Conference on*, 2009, pp. 1–6.

[46] J. Guerrero, J. Matas, L. G. de Vicuna, M. Castilla, and J. Miret, "Decentralized control for parallel operation of distributed generation inverters using resistive output impedance," *Industrial Electronics, IEEE Transactions on*, vol. 54, no. 2, pp. 994–1004, 2007.

[47] J. Guerrero, N. Berbel, J. Matas, J. Sosa, J. Cruz, and A. Alentorn, "Decentralized control for parallel operation of distributed generation inverters using resistive output impedance," in *Power Electronics and Applications, 2005 European Conference on*, 2005, pp. 10 pp.–P.10.

[48] S. Bala and G. Venkataramanan, "Autonomous power electronic interfaces between microgrids," in *Energy Conversion Congress and Exposition, 2009. ECCE 2009. IEEE*, 2009, pp. 3006–3013.

[49] ——, "On the choice of voltage regulators for droop-controlled voltage source converters in microgrids to ensure stability," in *Energy Conversion Congress and Exposition (ECCE), 2010 IEEE*, 2010, pp. 3448–3455.

[50] S. Bala, "Integration of single-phase microgrids," Ph.D. dissertation, University of Wisconsin-Madison, 2008.

[51] M. Erickson, T. Jahns, and R. Lasseter, "Improved power control bandwidth of grid-forming sources in a certs microgrid," in *Energy Conversion Congress and Exposition (ECCE), 2012 IEEE*, 2012, pp. 2366–2373.

[52] ——, "Impact of active resistance on dynamic power responses in a certs microgrid," in *Power and Energy Conference at Illinois (PECI), 2012 IEEE*, 2012, pp. 1–5.

[53] M. J. Erickson, "Improved power control of inverter sources in mixed-source microgrids," Ph.D. dissertation, University of Wisconsin-Madison, 2013.

[54] K. De Brabandere, B. Bolsens, J. Van den Keybus, A. Woyte, J. Driesen, and R. Belmans, "A voltage and frequency droop control method for parallel in-

verters," *Power Electronics, IEEE Transactions on*, vol. 22, no. 4, pp. 1107–1115, 2007.

[55] E. Barklund, N. Pogaku, M. Prodanovic, C. Hernandez-Aramburo, and T. Green, "Energy management in autonomous microgrid using stability-constrained droop control of inverters," *Power Electronics, IEEE Transactions on*, vol. 23, no. 5, pp. 2346–2352, 2008.

[56] G. Diaz, C. Gonzalez-Moran, J. Gomez-Aleixandre, and A. Diez, "Scheduling of droop coefficients for frequency and voltage regulation in isolated microgrids," *Power Systems, IEEE Transactions on*, vol. 25, no. 1, pp. 489–496, 2010.

[57] N. Jayawarna, X. Wu, Y. Zhang, N. Jenkins, and M. Barnes, "Stability of a microgrid," in *Power Electronics, Machines and Drives, 2006. The 3rd IET International Conference on*, 2006, pp. 316–320.

[58] C. Marinescu and I. Serban, "Analysis of frequency stability in a residential autonomous microgrid based on a wind turbine and a microhydro power plant," in *Power Electronics and Machines in Wind Applications, 2009. PEMWA 2009. IEEE*, 2009, pp. 1–5.

[59] X. Xu, T. Lin, and X. Zha, "Probabilistic analysis of small signal stability of microgrid using point estimate method," in *Sustainable Power Generation and Supply, 2009. SUPERGEN '09. International Conference on*, 2009, pp. 1–6.

[60] R. Middlebrook, "Input filter considerations in design and application of switching regulators," in *IEEE IAS Annual meeting*, 1976, pp. 366–382.

[61] ——, "Small-signal modeling of pulse-width modulated switched-mode power converters," *Proceedings of the IEEE*, vol. 76, no. 4, pp. 343–354, 1988.

[62] I. Cvetkovic, M. Jaksic, D. Boroyevich, P. Mattavelli, F. Lee, Z. Shen, S. Ahmed, and D. Dong, "Un-terminated, low-frequency terminal-behavioral d-q model of three-phase converters," in *Energy Conversion Congress and Exposition (ECCE), 2011 IEEE*, 2011, pp. 791–798.

[63] R. Burgos, D. Boroyevich, F. Wang, K. Karimi, and G. Francis, "Ac stability of high power factor multi-pulse rectifiers," in *Energy Conversion Congress and Exposition (ECCE), 2011 IEEE*, 2011, pp. 3758–3765.

[64] ——, "On the ac stability of high power factor three-phase rectifiers," in *Energy Conversion Congress and Exposition (ECCE), 2010 IEEE*, 2010, pp. 2047–2054.

[65] M. Belkhayat, "Stability criteria for ac power systems with regulated loads," Ph.D. dissertation, Purdue University, 1997.

[66] B. Wen, D. Boroyevich, P. Mattavelli, Z. Shen, and R. Burgos, "Experimental verification of the generalized nyquist stability criterion for balanced three-phase ac systems in the presence of constant power loads," in *Energy Conversion Congress and Exposition (ECCE), 2012 IEEE*, 2012, pp. 3926–3933.

[67] M. Cespedes and J. Sun, "Online grid impedance identification for adaptive control of grid-connected inverters," in *Energy Conversion Congress and Exposition (ECCE), 2012 IEEE*, 2012, pp. 914–921.

[68] Z. Staroszczyk, "A method for real-time, wide-band identification of the source impedance in power systems," *Instrumentation and Measurement, IEEE Transactions on*, vol. 54, no. 1, pp. 377–385, 2005.

[69] Y. Familiant, K. Corzine, J. Huang, and M. Belkhayat, "Ac impedance measurement techniques," in *Electric Machines and Drives, 2005 IEEE International Conference on*, 2005, pp. 1850–1857.

[70] Y. Familiant, J. Huang, K. Corzine, and M. Belkhayat, "New techniques for measuring impedance characteristics of three-phase ac power systems," *Power Electronics, IEEE Transactions on*, vol. 24, no. 7, pp. 1802–1810, 2009.

[71] J. Huang, K. Corzine, and M. Belkhayat, "Single-phase ac impedance modeling for stability of integrated power systems," in *Electric Ship Technologies Symposium, 2007. ESTS '07. IEEE*, 2007, pp. 483–489.

[72] ——, "Small-signal impedance measurement of power-electronics-based ac power systems using line-to-line current injection," *Power Electronics, IEEE Transactions on*, vol. 24, no. 2, pp. 445–455, 2009.

[73] G. Francis, R. Burgos, D. Boroyevich, F. Wang, and K. Karimi, "An algorithm and implementation system for measuring impedance in the d-q domain," in *Energy Conversion Congress and Exposition (ECCE), 2011 IEEE*, 2011, pp. 3221–3228.

[74] D. Martin, E. Santi, and A. Barkley, "Wide bandwidth system identification of ac system impedances by applying pertubations to an existing converter," in *Energy Conversion Congress and Exposition (ECCE), 2011 IEEE*, 2011, pp. 2549–2556.

[75] G. Venkataramanan and B. Wang, "Dynamic modeling and control of three phase pulse width modulated power converters using phasors," in *Power Electronics Specialists Conference, 2004. PESC 04. 2004 IEEE 35th Annual*, vol. 4, 2004, pp. 2822–2828 Vol.4.

[76] A. Halanay, *Differential Equations: Stability, Oscillations, Time Lags*, ser. Mathematics in science and engineering, v. 23. Academic Press, 1966.

[77] S. Sanders, J. Noworolski, X. Liu, and G. C. Verghese, "Generalized averaging method for power conversion circuits," in *Power Electronics Specialists Conference, 1990. PESC '90 Record., 21st Annual IEEE*, 1990, pp. 333–340.

[78] P. Mattavelli, G. Verghese, and A. Stankovic, "Phasor dynamics of thyristor-controlled series capacitor systems," *Power Systems, IEEE Transactions on*, vol. 12, no. 3, pp. 1259–1267, 1997.

[79] M. Hannan and K. Chan, "Modern power systems transients studies using dynamic phasor models," in *Power System Technology, 2004. PowerCon 2004. 2004 International Conference on*, vol. 2, 2004, pp. 1469–1473 Vol.2.

[80] N. Bogoliïÿăuïÿąbov and I. Mitropolskii, *Asymptotic Methods in the Theory of Non-Linear Oscillations*, ser. International monographs on advanced mathematics and physics. Gordon & Breach, 1961.

[81] C. DeMarco and G. Verghese, "Bringing phasor dynamics into the power system load flow," in *25th North American Power Symposium, Howard University*, 1993, pp. 463–471.

[82] H. Roder, "Amplitude, phase, and frequency modulation," *Radio Engineers, Proceedings of the Institute of*, vol. 19, no. 12, pp. 2145–2176, 1931.

[83] B. Van Der Pol, "Frequency modulation," *Radio Engineers, Proceedings of the Institute of*, vol. 18, no. 7, pp. 1194–1205, 1930.

[84] W. Everitt, "Frequency modulation," *American Institute of Electrical Engineers, Transactions of the*, vol. 59, no. 11, pp. 613–625, 1940.

[85] K. Sturley, "Frequency modulation," *Electrical Engineers - Part III: Radio and Communication Engineering, Journal of the Institution of*, vol. 92, no. 19, pp. 197–213, 1945.

[86] J. R. Carson and T. C. Fry, "Variable frequency electric circuit theory with application to the theory of frequency-modulation," *Bell System Technical Journal*, vol. 16, no. 4, pp. 513–540, 1937. [Online]. Available: http://dx.doi.org/10.1002/j.1538-7305.1937.tb00766.x

[87] J. R. Carson, "Notes on the theory of modulation," *Radio Engineers, Proceedings of the Institute of*, vol. 10, no. 1, pp. 57–64, 1922.

[88] H. Black, *Modulation theory*, ser. Bell Telephone Laboratories series. Van Nostrand, 1953.

[89] A. Hund, *Frequency Modulation*, ser. Raio communication series. McGraw-Hill, 1942.

[90] J. Roberts, *Angle Modulation: The Theory of System Assessment*, ser. IEE Publication Series. Books on Demand, 1977.

[91] L. Giacoletto, "Generalized theory of multitone amplitude and frequency modulation," *Proceedings of the IRE*, vol. 35, no. 7, pp. 680–693, 1947.

[92] M. Ilić and J. Zaborszky, *Dynamics and Control of Large Electric Power Systems*, ser. A Wiley-Interscience publication. Wiley, 2000.

[93] M. J. Erickson, "Integration of battery-based energy storage element in the certs microgrid," Master's thesis, University of Wisconsin-Madison, 2009.

[94] P. Mendoza-Araya, P. Kollmeyer, and D. Ludois, "V2g integration and experimental demonstration on a lab-scale microgrid," in *Energy Conversion Congress and Exposition (ECCE), 2013 IEEE*, 2013, pp. 5165–5172.

[95] G. Venkataramanan and B. Johnson, "A pulse width modulated power line conditioner for sensitive load centers," *Power Delivery, IEEE Transactions on*, vol. 12, no. 2, pp. 844–849, 1997.

[96] M. John, "Small signal impedance spectroscopy for three phase ac systems for studying stability of ac microgrids," Diploma thesis, Leibniz Universität Hannover, Germany, 2014.

[97] (2013) Discovery kit for STM32F401 line. STMicroelectronics. [Online]. Available: http://www.st.com/st-web-ui/static/active/en/resource/technical/document/data_brief/DM00094495.pdf

[98] (2008) DL750 ScopeCorder (Bulletin 7012-00E). Yokogawa Electric Corporation. [Online]. Available: http://cdn6.us.yokogawa.com/uploaded/bu7012_00E_030.pdf

[99] D. W. Novotny and T. Lipo, *Vector Control and Dynamics of AC Drives*, ser. Monographs in electrical and electronic engineering. Oxford University Press, 1996.